Three Dimensional Velocity Tomography in the Core of Messier 71

by

Raminder Singh Samra

B.Sc., The University of British Columbia, 2009

A THESIS SUBMITTED IN PARTIAL FULFILLMENT OF
THE REQUIREMENTS FOR THE DEGREE OF

MASTER OF SCIENCE

in

The Faculty of Graduate Studies

(Astronomy)

THE UNIVERSITY OF BRITISH COLUMBIA

(Vancouver)

March 2013

© Raminder Singh Samra 2013

Abstract

Using the Gemini North Telescope at Mauna Kea we have obtained astrometric and spectroscopic data for stars in the core of the galactic globular cluster Messier 71 (NGC 6838). This data has allowed us to for the first time ever to obtain three dimensional velocity profiles for stars in the vicinity of centre of a globular cluster. Using the Near Infrared Imager with Adaptive Optics and a 3.8 year baseline for our astrometric study we have resolved the internal proper motion dispersion. The proper motion dispersion is found to be $179\pm17\mu$arcsec year^{-1}, we have put a strict limit to the size of any central Intermediate Mass Black Hole at $\sim150M_{\odot}$ at 90% confidence, additionally we find no evidence of core anisotropy. Using our GMOS Integrated Field Unit spectroscopic data we have obtained a radial velocity dispersion of 3.54 ± 0.64 km s^{-1}. Combining our proper motion and radial velocity dispersions we find the geometric distance to the cluster to be 4.1 ± 1.2 kpc. We then compare our geometric distance to a distance found from fitting stellar evolution models. We have developed a new technique for fitting models, using this technique we find the stellar evolution model distance to be 3.9 ± 0.2 kpc. We then discuss how this technique can easily be applied to other clusters in any future work.

Preface

A substantial portion of this work was published in the May 2012 edition of the Astrophysical Journal Letters. All image processing, reduction and analysis was done entirely by myself with the guidance of my supervisor and co-authors of our article. The manuscript preparation and submission was done entirely by myself with the guidance of my supervisor and co-authors. The work published in the journal is included in the second and third chapter of this thesis. Works in chapters four and five are new techniques and are subjected to potential future publications.

- Samra, Raminder S et al. Proper Motions and Internal Dyanmics in the Core of the Globular Cluster M71, The Astrophysical Journal Letters, Volume 751, Issue 1, article id. L12, 5 pp. (2012).

Table of Contents

Abstract ii

Preface iii

Table of Contents iv

List of Tables vi

List of Figures vii

List of Acronyms xiii

Acknowledgements xiv

Dedication xv

1 Introduction 1
- 1.1 Globular Clusters 1
- 1.2 Colour Magnitude Diagrams 2
- 1.3 Distances to Globular Clusters 4
- 1.4 Proper Motions 6
- 1.5 Intermediate Mass Black Holes 7
- 1.6 Messier 71 9
  - 1.6.1 History 9
  - 1.6.2 Recent Work 10

2 Data Reduction and Processing of Astrometric Data . . . 12
- 2.1 Adaptive Optics 12
- 2.2 Data 13
- 2.3 Data Reduction 14
- 2.4 Data Processing 17
  - 2.4.1 Making the Medianed Image and Finding List 18
  - 2.4.2 Making the Point Spread Functions 20

2.4.3 Running ALLFRAME 23

3 Analysis of Proper Motion Data 27
3.1 Sample Selection 27
3.1.1 Improving the Photometry 27
3.1.2 Colour Cuts 30
3.2 Proper Motion Distribution 32
3.2.1 High Proper Motion Stars 34
3.2.2 Proper Motion Isotropy 36
3.3 An Upper Limit to the Mass of any Central IMBH 39
3.4 Summary of Proper Motion Analysis 43

4 Reduction of Integrated Field Unit Data 44
4.1 Introduction to Spectroscopy 44
4.1.1 Different Types of Astronomical Spectroscopy 45
4.2 Gemini Multi Object Spectrograph Integrated Field Unit . . 47
4.3 Messier 71 IFU Data 49
4.4 Reduction of M71 IFU Data 51
4.5 Radial Velocities 61
4.6 Radial Velocity Dispersion 68

5 The Distance to Messier 71 71
5.1 Geometric Distance 71
5.2 Stellar Model Distance 71

6 Conclusions 75

Bibliography 77

Appendices

A NIRI Proper Motion Data 81

B IFU Radial Velocity Data 88

C Bulk Motion of Messier 71 91

D Installation of DAOPHOT 94

E Extra Photometric Work 98

List of Tables

2.1 Exposure times for observations 14

A.1 NIRI Proper Motion Data, the photometry is from the Advanced Camera for Surveys 87

B.1 Radial velocity data from the GMOS IFU, the photometry is from the Advanced Camera for Surveys. 90

List of Figures

1.1 A Colour Magnitude Diagram (CMD) of 47 Tuc. This CMD of 47 Tuc has the Hubble Space Telescope's F606 filter plotted against the difference between the F606W and the F814W magnitudes. This CMD has not been cleaned for proper motions and as a result is not exclusive for cluster members, therefore it shows the main sequence of the Small Magallenic Cloud stream which is located near the vicinity of the cluster. 2

1.2 A CMD of 47 Tuc with three different isochrones over plotted. The isochrones are for stars with similar abundances as 47 Tuc and only differ in age between themselves. No robust fitting technique was employed to make this plot. 4

1.3 To calculate a geometric distance to a cluster, one has to assume circular orbits and the proper motion dispersion is equal to the radial velocity dispersion. 5

1.4 Relationship between various velocity components of a star. The object is located at a distance d from the Sun and has proper motion of μ radians s^{-1}, $v_t = d \times \mu$, where v_t is the transverse velocity. 6

1.5 Various black hole models are plotted against the velocity dispersion of NGC 6388. The best fit model is for an IMBH of mass $\sim 18{*}10^3 M_\odot$. Data for figure is from Lutzgendorf (2011) [14] 8

1.6 The colour magnitude diagram of M71, data for figure is from Cuffey (1943) [7] 9

2.1 An image of the core of M71 using the 8m Gemini Telescope without the use of adaptive optics. The same field with adaptive optics can be seen in figure 2.4. 13

2.2 Image from the Hubble Space Telescope of M71 image is 3.35' x 3.35' the rough location of the NIRI/ALTAIR AO image is the red square 15

2.3 Raw NIRI image of the core of M71 in inverted color to demonstrate the artifacts that were removed during the reduction steps. The green circles are ghosting artifacts that appeared on some of the images. They are caused by internal reflections in the optical system. The ghosting artifacts were removed by employing a 12 step dither pattern. 16
2.4 A median combined image using the NIRI/Altair adaptive optics image in the K band. The green circle represents the cluster centre and the size of the circle represents the approximate uncertainty. Note this image has been rotated compared to figure 2.3. 19
2.5 A contour plot of a star's intensity near the edge of the field . 21
2.6 A contour plot of a star's intensity near the centre of the field 22
2.7 The relative location of one cluster member across the field in each of the three imaging epochs. The colored dots represent the derived locations from each ALLFRAME run. The error in the final position is determined from the spread in the points for each epoch. 24
2.8 The X and Y positions of the same star as a function of time. The proper motion was found from fitting a straight line through those points, the slope of the line multiplied by the NIRI f/32 plate scale gives the proper motion. The dashed lines represent one-sigma errors. 25
2.9 Proper Motion plot for 220 stars in our NIRI field. The motions have been corrected for right ascension and declination. 26

3.1 Colour Magnitude Diagram of the NIRI field 27
3.2 Colour Magnitude Diagram of Messier 71 obtained from the ACS Survey of Globular Clusters. The field here is the same from figure 2.2. 28
3.3 Colour Magnitude Diagram of Messier 71 obtained from the ACS Survey of Globular Clusters with the stars from our NIRI field (black circles) and the ones from Cudworth (black squares). The line at V = 17 is the limit for both datasets. For the NIRI data all stars brighter than 17 were saturated, whereas for Cudworth's data V = 17 was the limit for detecting stars 30
3.4 Colour criteria for our proper motion sample. The black points represent our NIRI field stars whereas the green stars are Cudworth's. 31

3.5 *Left:* Proper motions diagrams for both the NIRI field and Cudworth's stars for which we have ACS photometry. *Right:* The proper motions of stars which survived the colour cut and the subsequent error cut from figure 3.4. The circle represents the cluster's escape proper motion. As with figure 3.4 the black points are our proper motion data whereas the green are Cudworth's. 32
3.6 A simulation of the galactic field for the same galactic coordinates of M71. For stars with V $\leq$ 17, a field 100x the ACS field was simulated. For stars V $\leq$ 17 a field 100x our NIRI field was simulated. The red stars are the ones that meet the colour cuts from figure 3.4. 35
3.7 The proper motion vectors for the escaping stars that survived the color and proper motion error cuts. The vectors are plotted to show the trajectory of the stars over the next 5000 years. The X marks the centre of the cluster. 36
3.8 Histogram of the proper motion angle with respect to the center of the cluster. Blue histograms are for stars in the NIRI field, and the dashed red line histogram is for stars from [6]. 37
3.9 Histograms for the values Q_{n_r}/Q_{n_t} resulting from the bootstrap resample of the data. The radial and tangential values of Q_n are consistent with unity within 1σ for all stars. . . . 38
3.10 The observed proper motion dispersion and three different IMBH models. 39
3.11 The results from bootstrapping the proper motion data 25,000 times. The IMBH mass from each fit is binned here. The leftmost bin from $0 \leq M_{\odot} \leq 5$ peaks at 20,500 counts, implying that a very small central IMBH is the preferred fit. The red line represents the 90th percentile at $150\text{M}_{\odot}$. 40
3.12 A dispersion map of the field, obtained by running a circle with a $4''$ diameter across the field and calculating the dispersion in each area. Observationally, there are no signs of radial dependence or an increase in dispersion towards the center which is represented by the X. 42

4.1 An example of how an integrated field unit (IFU) works. The hexagons represent lenslets which have the ability of capturing a spectrum individually. 46

4.2 GMOS IFU example data of a dwarf galaxy. At the top is the reconstructed IFU image with the left panel showing the sky field. Bottom shows the raw CCD image. The sky and object fields are arranged into alternating blocks on the CCD. Also prominent in the image are the chip gaps between the three GMOS CCDs. 48
4.3 The transmission curve for the Calcium Triplet Filter at Gemini North 50
4.4 Examples of calibration images from the IFU. Top: The raw bias image supplied by Gemini. Bottom: A Raw GCAL flat from one of the nights of observations. 51
4.5 Top: Calibration Copper-Argon arcs. Bottom: The raw twilight image. There is a discontinuity in all IFU images in the centre chip. This is the location where the red slit's dispersion ends and the blue slit's starts. 52
4.6 Flowchart detailing the steps for IFU data reduction. The arrows have the Gemini IRAF task required for the steps. The red boxes denote final reduced files required extracting science data. 53
4.7 Top: The Gemini Calibration flat after the results of step 1 is seen above. The chip gaps have been accounted for and the two slits have been stitched together. Bottom: The reduced twilight flat prior to wavelength calibration. 54
4.8 The response image. This is the final flat field. 55
4.9 Copper-Argon arc spectrum 55
4.10 Wavelength calibration of the arc spectrum by fitting various functions. Having too many fitting parameters can cause erroneous fits. 56
4.11 The effect of applying the wavelength transform onto the twilight flats. The top figure shows the twilight flat prior to wavelength calibration. The bottom figure is the final calibrated flat. The Calcium Triplet lines are easily observed here as the three bright vertical lines in the image. Wavelength increases from left to right. The vertical axis represents the spectra from individual IFU fibers. The horizontal split in the bottom figure is due to the two slits used in the IFU. . . 57
4.12 Raw science image. Stellar spectra are the bright bands that run from left to right. 58

4.13 Science image after all data reduction. Wavelength increases from left to right. Each of the 1500 IFU fibers are shown here increasing from bottom upwards. 59
4.14 Top: Map of the six IFU fields stitched together. There is no overlap between the fields. Each of the six fields appears to be split in half. This is due to the scaling of the image and the differences in throughput of the two IFU slits. Bottom: IFU map of the sky field located 1 arcminute away from the larger field. 60
4.15 Image of the cluster obtained by one of the three GMOS CCDs used for target acquisition. Red represents the two IFU fields, yellow represents the NIRI field also found in figure 2.4. The blue is the field of the ACS from figure 2.2. . . 61
4.16 Cross correlation of two signals. Where the signals overlap there is a maximum in the correlation function. If these were two spectra, the radial velocity would be the offset of the peak of the correlation function. This is analogous to a sliding dot product of two signals. 62
4.17 Twilight Spectra. The figure on the right shows a close up of the three regions of cross correlation when the lines are used individually. 62
4.18 The spectra of one IFU fiber and the corresponding star from which the fiber was from. Brighter stars have many more illuminated fibers. 63
4.19 Spectra of a single IFU fiber for four different stars. Stars fainter than V = 20 did not have strong enough Calcium Triplet lines for velocity measurements. 64
4.20 The correlation function of two spectra. The fitting function here is a gaussian represented by the dashed curve. 65
4.21 The response from CCD flexure. The left panel shows the arc spectrum with individual emission lines coloured. In the two figures on the right hand side, we see the result of cross correlating the coloured region against a median combined arc of that same region. The bottom panel is a zoom of the top panel to show how CCD flexure varies across the chip. . 67
4.22 The CMD of the IFU stars for which we have radial velocities is overlaid on the CMD of the ACS field. The cluster members are the stars which satisfy the colour criteria from figure 3.4 and the proper motion cut from figure 3.5. 69
4.23 Radial velocities of the same stars from figure 4.22. 70

5.1 The CMD from figure 3.2 with a median line running down the centre. Here V is now in Vega magnitudes. 72
5.2 Top: The fiducial cmd and the derivative of the cmd. Bottom: An 11 Gyr isochrone of stars with similar abundances as M71 and the corresponding derivative. 73
5.3 By shifting the isochrone so that the spike of the derivative matches that of the observed data, we get the distance modulus. The left panel is over the entire CMD. The right panel is a close up of the turn off. 74

C.1 An example of a NIRI image prior to star subtraction. 91
C.2 Four objects were found to survive both cuts in residual flux and sharpness. Three of them were found to be on the cluster CMD, the fourth was not. 92

D.1 Daophot Makefile. 95
D.2 The Makefile is now edited so Allstar is the next suite to be packaged. Run Makefile again and Allstar will be installed. . 97

E.1 Canada-France-Hawaii Telescope image of M71 from The CFHT Adaptive Optics Bonnette from 1991. With a field of view is $90'$ on each side of the image, two images one in B and the other in R with a integration time of 120s for each filter. . . . 99
E.2 A CMD from the data in Figure E.1. The CMD is in uncalibrated magnitudes. 100
E.3 Image of Messier 71 obtained using the Wide Field Infrared camera from CFHT. The image is $20'$ x $20'$. This is a H band image of the cluster which is found in the top left hand of the image. The red circle depicts a $\sim 7'$ circle centred on the cluster centre 101
E.4 A CMD from the data in Figure E.3. The stars within the circle are represented with red points, they are likely cluster members, likely galatic field stars are represented by black markers, those are also the stars which were not in the circle from Figure E.3. 102

List of Acronyms

ACS = Advanced Camera for Surveys
CCD = Charged Coupled Device
CMD = Colour Magnitude Diagram
FWHM = Full Width Half Maximum
HST = Hubble Space Telescope
GMOS = Gemini Multi-Object Spectrograph
IFU = Integrated Field Unit
IRAF = Image Reduction and Analysis Facility
NIRI = Near Infrared Imager
PSF = Point Spread Function

Acknowledgements

This work was supported and supervised by my supervisor Dr Harvey Richer. Dr Richer's insights and guidance in all aspects of this project allowed me to proceed down paths of discovery which ultimately made me a better scientist. I am also thankful for the numerous conversations I had with other members of the group including Dr Jeremy Heyl, Dr Kristin Woodley, Dr Gordon Walker, Dr Karun Thanjavur and fellow graduate student Ryan Goldsbury. Without everyone's help this project would not have arrived at its current stage. I thank all those mentioned for their exceptional help and support.

Dedication

The One who pervades the Universe also dwells in the body; whoever seeks Him, finds Him there.

- Guru Granth Sahib Ji, Raag Dhanaasree, Ang 695

This thesis is dedicated to my father Gurmit Singh Samra. My dad was responsible for me choosing to pursue my lifelong passion for astronomy, it was ultimately his decision that I enroll at the University of British Columbia and study astronomy. Dad your teachings and guidance are responsible for the person I've become. I hope I've made you proud. Even in these tough times your still the brightest star in my heart; I wish nothing but the best and clear skies.

Additionally I would like to thank my loving wife Ravneet for her continued support over the tenure of my graduate studies. Ravneet you've been instrumental in helping me get through the past few years and thanks for making life so fun and enjoyable. Astronomers look around for other planets and life in the universe, but to me the only one that matters is the one with you in it.

Chapter 1

Introduction

1.1 Globular Clusters

Star clusters come in two basic varieties; loosely packed open clusters and densely packed globular clusters. The two cluster types not only differ in their stellar densities but also in their ages and locations in the galaxy. Open clusters are almost always found in the disk of the Galaxy and tend to contain young stars. These clusters contain several thousand stars with a size of a few parsecs across. By contrast, globular clusters are found in a large halo surrounding the galaxy and contain some of the oldest stars in the universe. Globular clusters can have up to a million stars concentrated in a large spheroid many dozens of parsecs in size. The central regions of a globular cluster are very crowded with typical separations between stars being much less than a parsec.

Our Milky Way galaxy contains ∼160 catalogued globular clusters. Larger galaxies such as the nearby Andromeda Galaxy (Messier 31) have about 500, and galaxies such as Messier 81 are thought to contain over 10,000 globular clusters [28]. The primary constituents of globular clusters are stars. There is little gas in the space between the individual stars, and there is no evidence for the existence of dark matter in globulars as well. As these stars were formed from the same gas cloud near the same time, they have very similar composition. Additionally, stars in the cluster can also be approximated to be the same distance from the Earth. It is these properties of globular clusters that make them ideal candidates for studying stellar evolution, stellar dynamics, galactic evolution and assist in putting an age on the universe as a whole.

Generations of star formation ultimately leave a mark on the composition of interstellar material, thus astronomers group stars according to their metallicity. Metallicity is expressed as

$$[Fe/H] = log_{10}(N_{Fe}/N_H)_{star} - log_{10}(N_{Fe}/N_H)_{\odot} \tag{1.1}$$

Where [Fe/H], is the logarithm of the ratio of a star's iron abundance

compared to the Sun's. Metallicity can then be used to distinguish disk populations from halo populations. Disk clusters generally have [Fe/H] $\geq$ -0.8 and halo clusters [Fe/H] $\leq$ -0.8. [31]. Clusters which are metal rich have [Fe/H] $\sim$ +0.25, whereas metal poor clusters have [Fe/H] $\sim$ -2.5. Although iron is used as a measure of metallicity, it is far from being the most abundant heavy element present. Iron's strong spectrum in the visible band allows it to be the ideal spectral feature for identifying abundances.

1.2 Colour Magnitude Diagrams

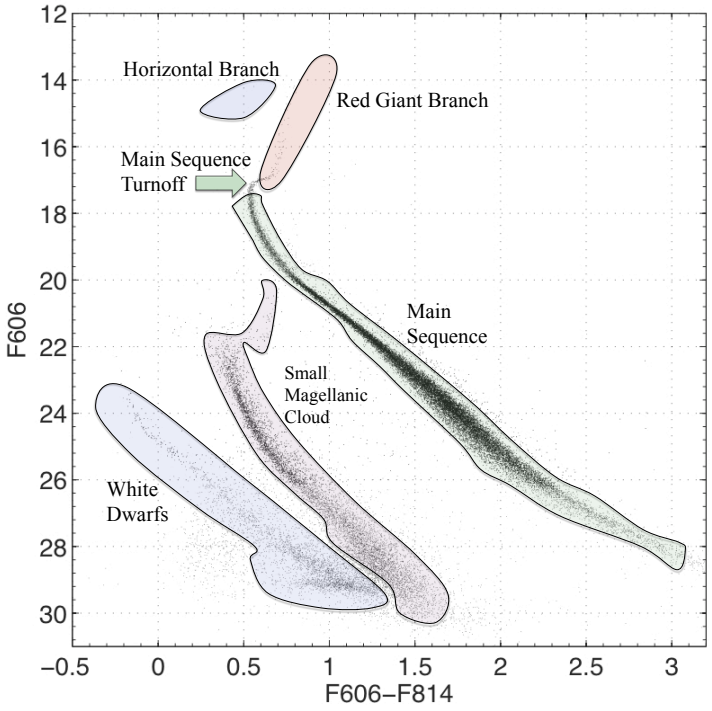

Figure 1.1: A Colour Magnitude Diagram (CMD) of 47 Tuc. This CMD of 47 Tuc has the Hubble Space Telescope's F606 filter plotted against the difference between the F606W and the F814W magnitudes. This CMD has not been cleaned for proper motions and as a result is not exclusive for cluster members, therefore it shows the main sequence of the Small Magallenic Cloud stream which is located near the vicinity of the cluster.

To determine the effective temperature for a large sample of stars would require a detailed spectral line analysis for each star. However, it is much faster and efficient to determine the colour index of an individual star. Once an apparent magnitude of a star in a particular filter is measured, a colour-magnitude diagram (CMD) can be constructed. All stars will end up somewhere on a CMD depending on their stage in stellar evolution. A random sample of stars will form a pattern on the diagram but will have scatter, as the stars were born at different times, have different metallicities or their distances are different. If the stars are all from the same cluster, thus formed nearly at the same time, a CMD will have a well defined narrow sequence. From this sequence, information about the stars and the particular cluster can be obtained. Globular clusters have such a sequence and it can be seen in figure 1.2.

All stars will spend most of their lives on the main sequence where they undergo Hydrogen core burning. More massive stars are located higher up on the main sequence and less massive stars are found at the lower end. Once a star completes Hydrogen to Helium fusion in its core, it will reach the main sequence turn off point and migrate to the red giant branch. It is worth noting that a star will not move up or down the main sequence during its Hydrogen core burning phase, rather the main sequence turn off point will migrate downward with time. As stars leave the main sequence, they swell up and increase their size, become redder and exhibit a large increase in brightness. During this phase, hydrogen is burning in a shell around the Helium rich core. With the onset of Helium burning in the core, the star will enter the horizontal branch. Evolutionary processes are now much faster than they were when the star was on the main sequence. Once on the horizontal branch, a star will enter the asymptotic giant branch and exhibit large pulsations which cause the outer layers of the star to be shed into a planetary nebula. The core of the star remains as a hot white dwarf star. White dwarf stars are the last remains of a sun-like star and it will slowly cool with time. White dwarfs can be found on the lower left side of a CMD. The exact location of a white dwarf cooling sequence can be used with models to determine the age of a particular cluster.

1.3 Distances to Globular Clusters

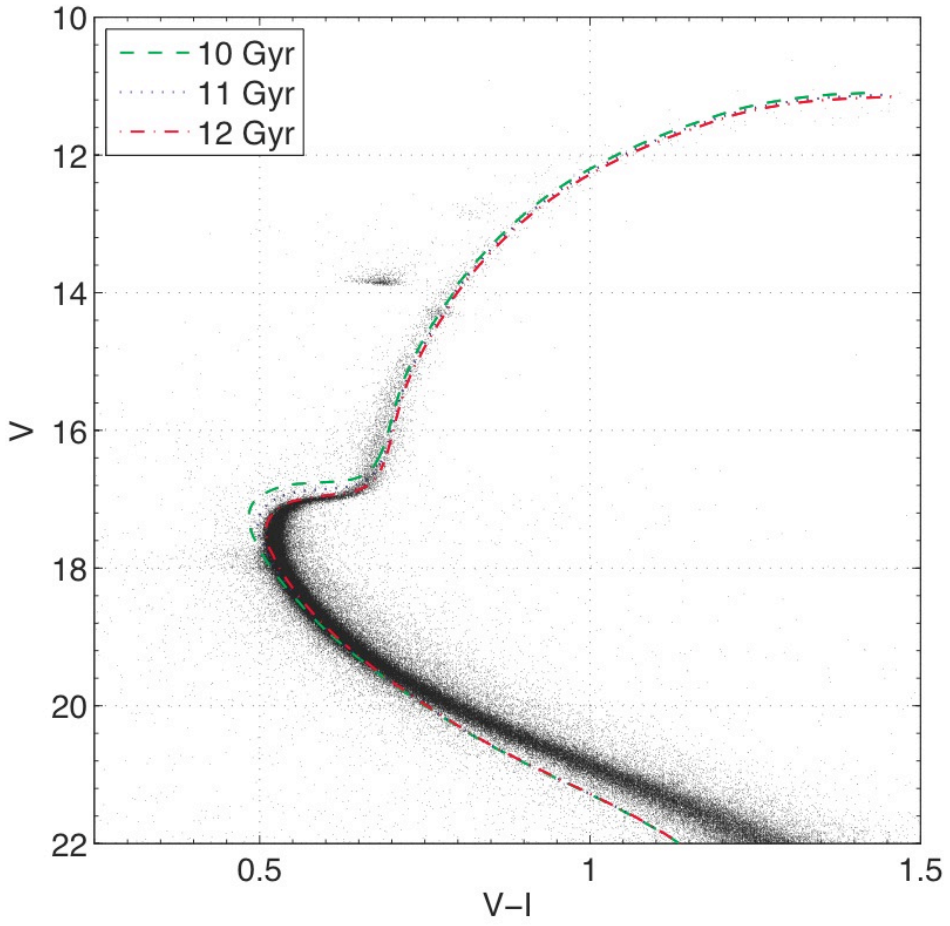

Figure 1.2: A CMD of 47 Tuc with three different isochrones over plotted. The isochrones are for stars with similar abundances as 47 Tuc and only differ in age between themselves. No robust fitting technique was employed to make this plot.

One of the challenges in astronomy and astrophysics is calculating distances to celestial objects. Several methods are used to determine distance. This is dependent upon the type of object (ie: galaxy, star, star cluster or planet) and the quality of the available data. For nearby objects in the solar system,

radar ranging is an accurate way to determine distances. This technique cannot work for anything beyond the solar system. Nearby stars can have their distance determined using parallax, which requires multiple measurements of the star's parallax angle. For stars which are further, their distance is determined via a process known as main-sequence fitting. Once an accurate distance for a nearby star is known via parallax and its spectra is also established, its absolute magnitude can be determined. The same spectral type star can then be found elsewhere and after determining the apparent magnitude, its distance can then be computed. This technique can then yield stellar evolution models which can be used to construct isochrones.

Isochrones are theoretical curves that simulate the life of stars, all of which have the same chemical abundances but only differ in mass; such is the case in a globular cluster. As isochrones are theoretical models, they yield absolute magnitudes versus colour curves. To determine distance, an isochrone simply has to be shifted vertically to get the distance modulus. Horizontal shifts will determine the amount of reddening between the cluster and observer. This technique can also determine a cluster's age, however recent evidence shows that globular clusters may have multiple stellar populations. As a result this may make fitting isochrones difficult.

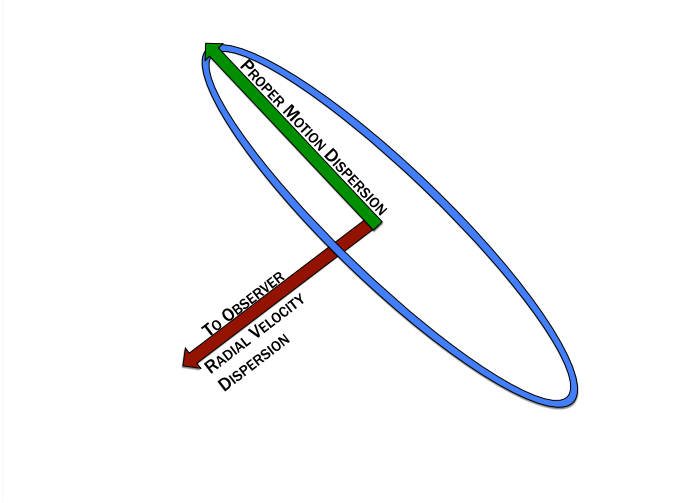

Figure 1.3: To calculate a geometric distance to a cluster, one has to assume circular orbits and the proper motion dispersion is equal to the radial velocity dispersion.

Another method which is independent of stellar evolution models is to calculate a geometric distance to a cluster. This simply assumes that stars have isotropic orbits and the proper motion dispersion in each direction is equal to the radial velocity dispersion. Figure 1.3 shows the geometry for this method. The accuracy of the geometric distance can be increased if there are stars for which both the proper motions and radial velocities are known. Additionally, having more stars in the samples can reduce uncertainty.

1.4 Proper Motions

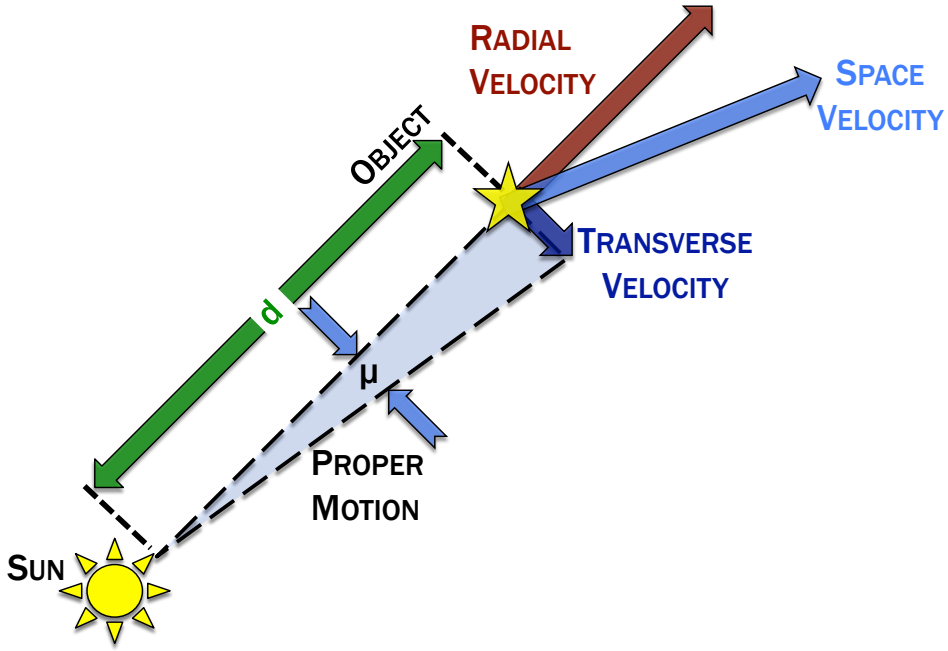

Figure 1.4: Relationship between various velocity components of a star. The object is located at a distance d from the Sun and has proper motion of μ radians s^{-1}, $v_t = d \times \mu$, where v_t is the transverse velocity.

As stars travel through space, their true space velocity can be measured by the observer in two orthogonal components; radial velocity and proper motion (see figure 1.4). The radial velocity of a star is the line of sight velocity measured directly via the doppler effect using a spectroscope. Proper

motions is the angular change of a star's position with time. It can be measured with respect to background stars or objects of known proper motion. Proper motions are measured in seconds of arc per year and require multiple epochs of imaging. Traditionally, proper motions were measured using images with baselines decades apart. However, with the onset of modern CCD cameras and telescopes, baselines of just a few years can be used to determine proper motions of stars.

Proper motions are instrumental for studying the dynamics of star clusters. As a star cluster has its own bulk proper motion, the proper motions of its stars are distinct from galactic field stars. Therefore, cluster members can be isolated for a sample of cluster only stars. From studying the motions of stars near the core of a globular cluster or galaxy, it is possible to obtain the mass of any central dark mass. Proper motion studies of stars in the vicinity of the galactic centre have been used to determine the existence of a super massive black hole SGR A* [11]. Similarly, proper motions can be used to determine the existence of a central massive black hole at the centre of a globular cluster.

1.5 Intermediate Mass Black Holes

It is well established that there are two known mass ranges of black holes. Stellar mass black holes are the remnants of massive stars and can be observed in accreting binary systems. There is also evidence for the existence of large super massive black holes (SMBHs) at the centers of galaxies. These typically have masses that range from $\sim 10^6 M_\odot$ to $\sim 10^9 M_\odot$. SMBHs have a tight correlation between their mass and the velocity dispersion of the galaxy which they reside. Extrapolating this relation down to velocity dispersions typically found for globular clusters, black holes with masses of $\sim 10^{3-4} M_\odot$ could exist.

As there is little gas to accrete in a globular cluster, detection via radio and X-ray emission is challenging. A more efficient method is to explore the kinematics of the central regions of a cluster. Wyller (1970) [30] proposed this method more than forty years ago, however it was limited by the quality of the observations. To detect a central black hole, spatial resolution on the order of the sphere of influence of the black hole must be achieved; typically 1-2″for globular clusters. Instruments such as the Hubble Space Telescope and ground based observatories with adaptive optics can resolve the internal motions of stars, whereas multi object spectroscopes and integrated field units can also provide the necessary resolution.

Evidence for the existence of IMBHs is still debatable. Noyola et al. (2008) [15] found evidence of an IMBH in ω Centauri, the largest globular cluster in the Milky Way galaxy. However, ω Cen. may not be a typical globular cluster rather the core of a dwarf spheroidal galaxy. Additionally, this claim is met with skeptism as Anderson and van der Marel (2009) [2] show evidence that counters this claim. They claimed that Noyola et al (2007) were not at the correct centre of ω Cen and calculated a different cluster centre which is $12''$ away, therefore they found no evidence for a central IMBH in ω Cen.

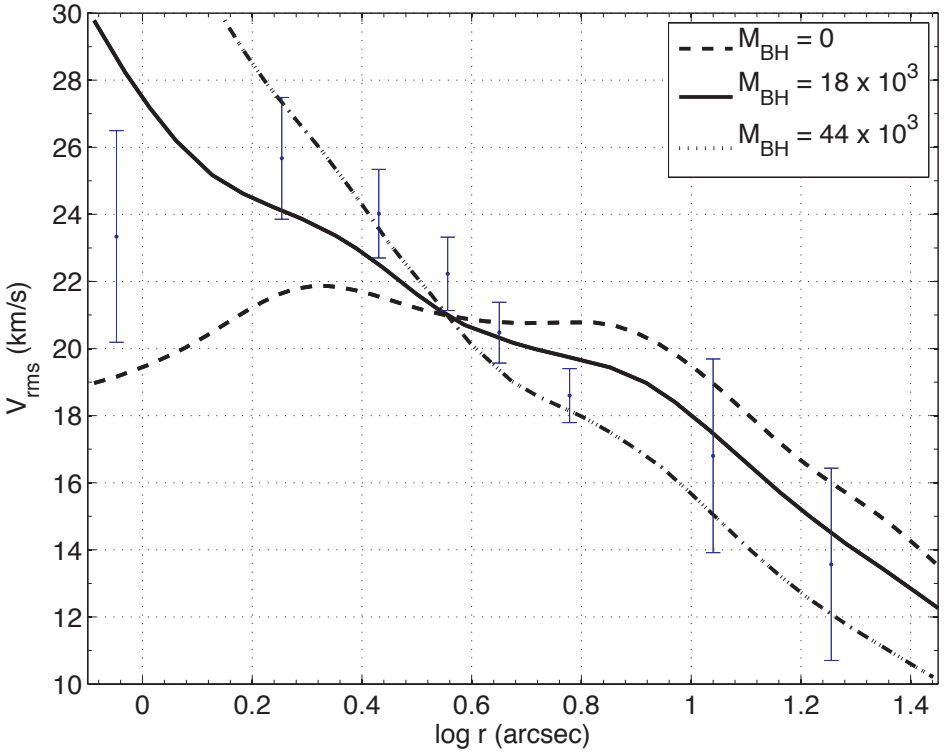

Figure 1.5: Various black hole models are plotted against the velocity dispersion of NGC 6388. The best fit model is for an IMBH of mass $\sim 18{*}10^3 M_\odot$. Data for figure is from Lutzgendorf (2011) [14]

Another globular cluster NGC 6388 has evidence for a central black hole. Using the kinematic signature of the central velocity dispersion in the core of this cluster, Lutzgendorf et al (2011) [14] show evidence for the existence

of a $\sim 18*10^3 M_\odot$ IMBH.

1.6 Messier 71

1.6.1 History

Messier 71 (NGC 6838) was discovered by in 1746 by Swiss astronomer Philippe Loys de Chseaux as the thirteenth object in his catalogue. M71 was subsequently rediscovered by Gottfried Koehler in 1772 and by Pierre Mechain on June 28th 1780. Charles Messier would classify it as his 71st object in his catalogue of faint celestial objects. Messier did not see any stars in the cluster, as his first claims were "its light is very faint and it contains no star; the least light makes it disappear".

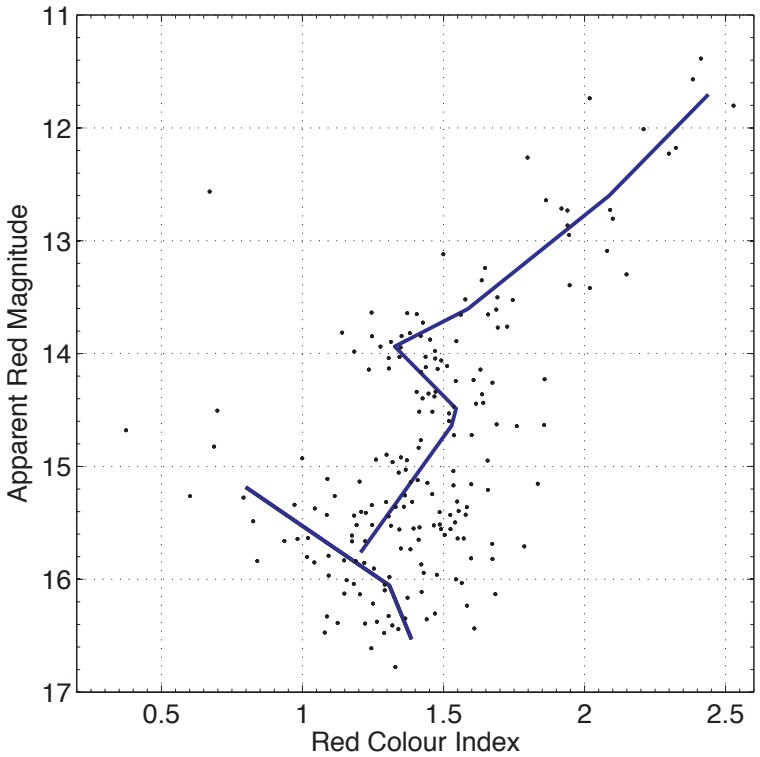

Figure 1.6: The colour magnitude diagram of M71, data for figure is from Cuffey (1943) [7]

Messier 71 was classified as a condensed open star cluster until the 20th century. Harlow Shapley had classifed it as the densest of all types in his classification scheme for open clusters. Cuffey (1943) [7] performed photometry and made a colour-magnitude diagram of red giant branch members. He recognized that M71's CMD (see figure 1.6.1) resembled that of a globular cluster. He also calculated the distance to be about 4000 parsecs.

1.6.2 Recent Work

In 1971 Arp and Hartwick [3] published the first modern photographic and photoelectric observations. They used the UBV system to yield a CMD that was typical of a metal rich cluster that exhibited a short red horizontal branch and a gently sloping giant branch. Additionally, they calculated the distance modulus $(m-M)_o = 13.07 \pm 0.21$, [Fe/H] = -0.30±0.2 and an age of 7.6(+3.1,-2.3) x 10^9 years. The age derived was younger than most halo globular clusters.

In 1984, Cudworth [6] performed photometry and studied proper motions of 350 stars with V $\leq$ 16 in the cluster [6]. Proper motions were used to clean the cluster CMD and he noted that the horizontal branch and lower giant branch resembled that of 47 Tuc. However, the upper part of the branch was bluer and brighter in M71. Proper motions were used to detect an internal velocity dispersion. He also studied the cluster's space velocity and determined it to be a very low, ∼50 km/s, characteristic of a disk-population object.

The first modern CCD observations were conducted by Richer and Fahlman in 1988 [18] as they carried out U and V band CCD imaging in the centre of the cluster to 205″ away. They found over 10,000 stars and investigated radial effects in the mass to luminosity relationship. They found that the global luminosity function was found to be flatter than 47 Tuc, a cluster with similar chemical abundances. The luminosity function favours the idea that the cluster is dynamically relaxed as the function shows an increase in the number of low luminosity stars at larger distances. By comparing the cluster's mass to light ratio, they found that a significant fraction of the cluster's mass is contained in stars outside the range of luminosities covered. Models placed the dark mass as either neutron stars, white dwarf stars or low mass sub-dwarf stars.

Current modern values for M71 can be found in Harris' 1996 catalogue [13]. The cluster's centre was found by Goldsbury et al (2010) [12], it is at right ascension, RA = $19^h53^m46^s.25$ and declination DEC = +18°46'46″.7 at J2000 coordinates. Harris places the distance to be 4.0 kpc from the Sun,

[Fe/H] = -0.73, half light radius $r_h = 1.65'$, tidal radius, r_t to be at $8.96'$ from the core. The core radius is $r_c = 0.63'$, larger than 70% of all galactic globulars. This large core radius was one motivation for our study as it could be "fluffy" due to a central black hole.

Chapter 2

Data Reduction and Processing of Astrometric Data

2.1 Adaptive Optics

Prior to the development of adaptive optics, ground based observatories had their resolution limited to that of the sky conditions at the observation site. To unlock the full potential of a telescope and operate near the diffraction limit telescopes had to be placed above the atmosphere in orbit. However, there are technical and financial limitations to the size of telescopes that can be placed in space. With the onset of modern adaptive optics, large optical telescopes now have the capability to operate at the diffraction limit.

Adaptive optics work by reducing the effect of wavefront distortions by measuring the distortions using a wavefront sensor and compensating for the distortions via a deformable mirror. As starlight enters the Earth's atmosphere it experiences turbulence from various temperature layers and wind speeds. As a result, the angular resolution suffers to that of the seeing conditions. Adaptive optics can correct for this using natural and laser guide stars. Often the science target is too faint to be used as a reference star for the measurement of wavefront. As a result, a nearby bright star must be used. Light from a reference star passes through approximately the same atmospheric turbulence as the science target so the same correction can be used. However, by having a nearby bright star (typically 12-15 V magnitude) in addition to the limitations of adaptive optics to small fields, only a small area of the sky can be used for natural guide stars.

Laser guide stars offer an alternative to natural guide stars. They work by employing a 589 nm sodium laser to excite sodium atoms 90 km high in the mesosphere. The sodium atoms glow as a result and are perceived as a star by the ground-based telescope which can use the wavefront distortions of the laser guide star for correcting the distortions in the science data. Figure

4.1 shows the core of Messier 71 as imaged by the 8m Gemini Telescope without the use of adaptive optics.

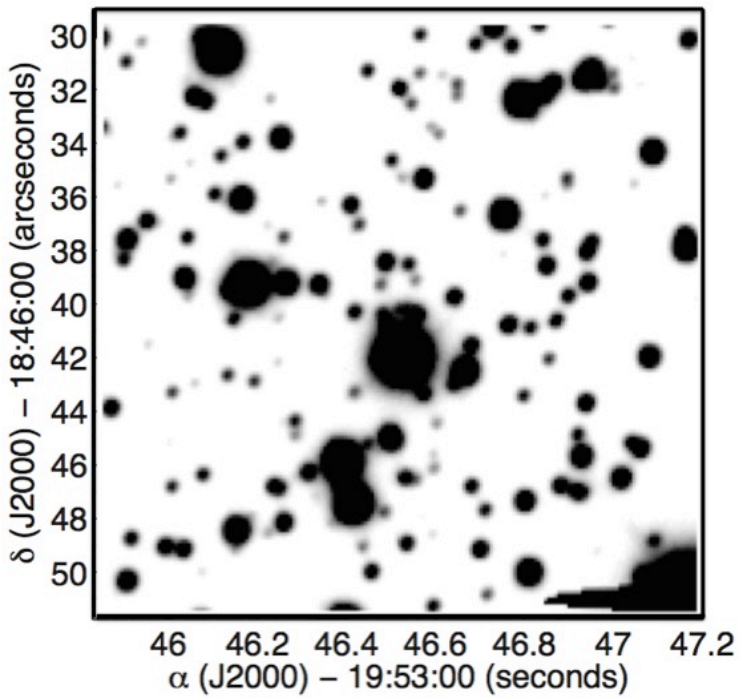

Figure 2.1: An image of the core of M71 using the 8m Gemini Telescope without the use of adaptive optics. The same field with adaptive optics can be seen in figure 2.4.

2.2 Data

In three separate imaging epochs we obtained H (centered at 1.65 microns) and K band (centered at 2.2 microns) imaging of the inner 22 x 22 arcseconds of M71 (see figure 2.2). The images were obtained by using the NIRI/ALTAIR Adaptive Optics system on the 8m Gemini North Telescope. For best imaging results, imaging was only conducted during the best seeing conditions at the summit of Mauna Kea. For all three imaging epochs, the set up was identical. The Near Infrared Imager (NIRI) was set to f/32 with a CCD size of 1024 by 1024 pixels corresponding to a plate scale of $0.0219''$ pixel^{-1}. This yielded a field of view of $22''$ x $22''$ centred on star

AH-81 ([3]), a twelfth magnitude star close to the cluster centre. A twelve step dither pattern was also employed to aid in the removal of artifacts during image processing.

Date	Filter	Exposure (ksec)	FWHM ($''$)
August 2005	H	15	0.085
August 2005	K	16	0.081
June 2007	H	14	0.083
June 2009	K	23	0.077

Table 2.1: Exposure times for observations

2.3 Data Reduction

The data for M71 was downloaded from the Canadian Astrophysical Data Centre. The processes outlined below were the same for each of the three imaging epochs and filters involved. However each epoch and filter was processed separately to account for any potential changes in the imaging system over the baseline of imaging.

Data reduction of Gemini data was performed using the Gemini IRAF package which was supplied by the Gemini Observatory. Gemini gives users a generic cookbook for reduction of NIRI data. Here we go into detail on reduction of data. Figure 2.3 shows a raw science image.

The first step in reduction is to use the task NPREPARE. This task updates the raw data headers and creates extensions in the multi exposure fits (MEF) images. This task requires updated settings of the detector arrays used in the imaging. It adds new header keywords which give an estimate of the gain, read noise, saturation level, array bias voltage and the threshold for data when it deviates from linearity. NPREPARE is run on all science and calibration data, and can be run simultaneously on all data.

The next task is to create a master flat field image. This flat field image can correct for illumination variances across the detector and some of the streaking artifacts from the CCD construction. NIFLAT require two types of flat field images; those taken with a lamp on and off. Lamp on and off images are obtained by shining a bright lamp onto the detector array and then removing it. This allows for the separation of the thermal signature of the detector for the sensitivity response. The exposure times for the flats was 4 seconds each. Multiple exposures are used to construct a median flat field image. This is done separately for each imaging epoch and filter.

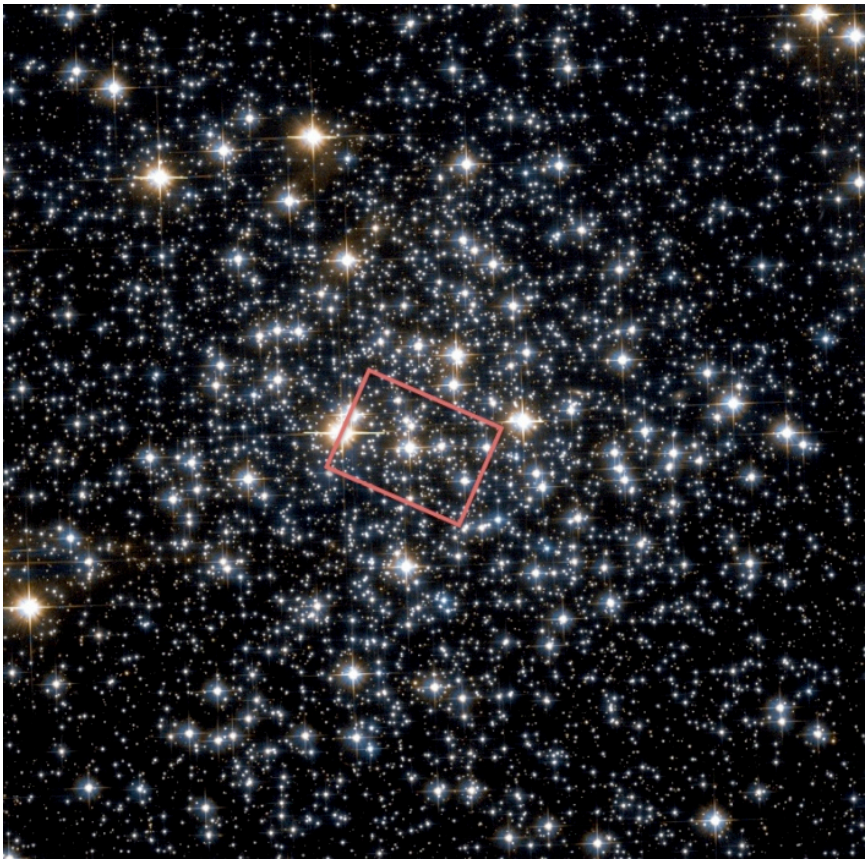

Figure 2.2: Image from the Hubble Space Telescope of M71 image is 3.35' x 3.35' the rough location of the NIRI/ALTAIR AO image is the red square

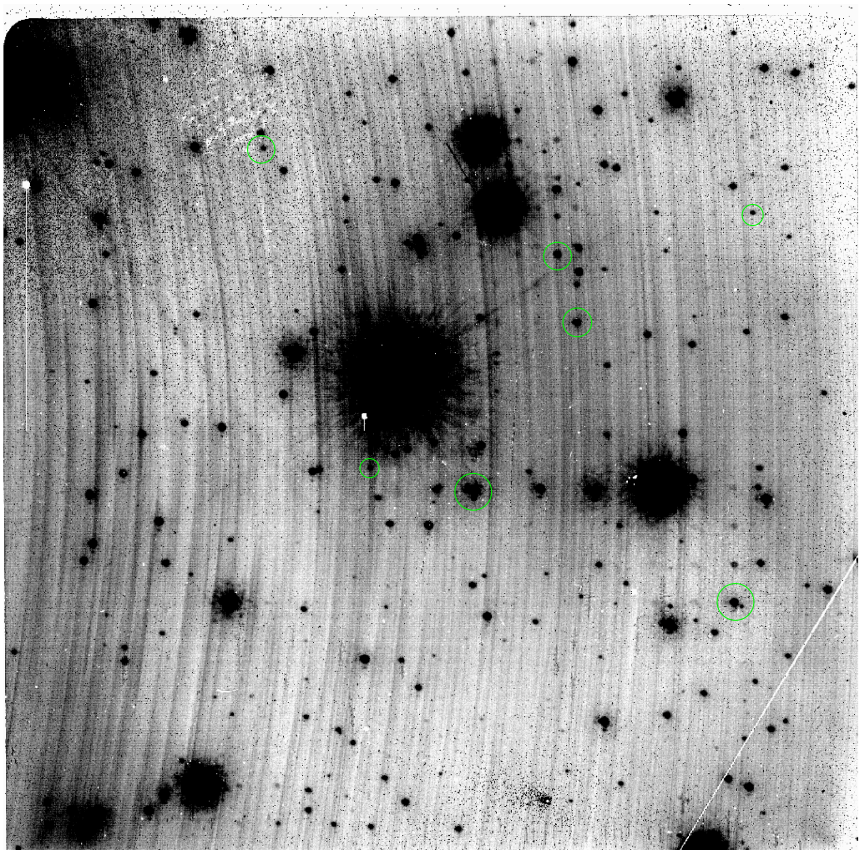

Figure 2.3: Raw NIRI image of the core of M71 in inverted color to demonstrate the artifacts that were removed during the reduction steps. The green circles are ghosting artifacts that appeared on some of the images. They are caused by internal reflections in the optical system. The ghosting artifacts were removed by employing a 12 step dither pattern.

Likewise, this task is used to create a master dark frame. Darks are captured with the camera shutter still closed, essentially capturing the noise in the imaging sensor. Dark frames of 140 second exposures were used to create a median combined master dark frame.

The final task is to run the IRAF task NIREDUCE. NIREDUCE takes in the raw science data, subtracts the bias and divides by the master flat and darks. After running NIREDUCE, most of the array artifacts are removed. Those which are not removed are easily distinguishable from stellar objects during the data processing. This task is done on all images from every epoch and filter individually. This results in about ∼700 images from the three imaging epochs.

2.4 Data Processing

Majority of the data was processed and analyzed using DAOPHOT [26], a standalone version of the software which allows for more freedom than the IRAF version. IRAF is still used to help with the identification of stars. A detailed data processing cookbook is available in [26]. The processing steps are outlined in § 2.4.1, § 2.4.2 and § 2.4.3. These sections explain how the median image, point spread functions and ALLFRAME were run.

Finding the Stars

The first task was to make a medianed image. This image would be used to create a finding list for all of the objects in the field. Ideally the medianed image would also not have any artifacts from the reduction, as they would have been filtered out. Before a medianed image could be made, the stars had to be identified. DAOPHOT was used to identify the stars. IRAF's IMEXAMINE routine was run to find the full-width-half-maximum of the stars in the field. The average FWHM was $\sim$ 3.5 pixels. It had little variance between the different nights of observations. Once the FWHM was known, the standalone version of DAOPHOT could be employed to find the locations of the stars on the chip. The FWHM was computed for each of the H and K filters used and IMEXAMINE was used to find the FWHM on each of the nights of observations for all three epochs.

Registration

As the data had been dithered to a 12 step pattern, it was important to put the data on the same coordinate system. This was done by using the DAO-

MATCH and DAOMASTER routines. The data were fed into DAOMATCH and it did a basic four term match which allows for the translation, rotation and scaling of the data. This task works automatically and produces the input file for the more versatile task, DAOMASTER. DAOMASTER first asks for the minimum number of frames an object has to be on for it to consider translating it; this was set to 70%. Then the software asks for the amount of terms we wish to incorporate into a transfer function to transform the data. As there was only simple translations between the dither pattern, a simple six term transformation equation was used for registeration. The software then transforms the coordinates of each object x_1, y_1 into x_2, y_2 via equations 2.1 and 2.2. The software then asks the user to pick a matching radius, a radius of 10 pixels was originally used. This radius is the distance of which the program searches for a matching star between frames. The program will then ask the user to reduce the matching radius and outputs how many stars remain for the given criteria. The user then slowly decreases the matching radius until the program converges onto a final number of detected stars. Finally, before DAOMASTER exits, it asks for the type of output file the user wants. First a transformation file was created which contains the values of the six constants for equations 2.1 to 2.2. Additionally new .coo files were outputted. The .coo files contain the transformed coordinate lists, allowing the user to find the same star across various frames with new x and y coordinates.

$$x_2 = A + Cx_1 + Ey_1 \tag{2.1}$$

$$y_2 = B + Dx_1 + Fy_1 \tag{2.2}$$

2.4.1 Making the Medianed Image and Finding List

Once all the stars were on the same coordinate, list aperture photometry was performed in DAOPHOT using the PHOT command. After performing aperture photometry, we had files with magnitudes of stars and their positions on each of the frames. It was now possible to construct a median image of the dataset. To make a medianed image MONTAGE2 was used. The input for this task was the transformation file outputted by DAOMASTER. MONTAGE2 then asks the user minimum number of frames an object must appear in before it is included. For all datasets a minimum threshold of 20% of the total number of frames was chosen, thus eliminating any remaining artifacts such as ghosts and hot pixels. Due to the dither pattern, the output median image was larger at 1100 x 1100 pixels, therefore more stars could be found on this image. The median image was then run through DAOPHOT's FIND command to find the positions of every star in

the median image. Originally, DAOPHOT returned ∼400 objects for which it had detected to be star-like. Most of these were found around the bright saturated stars. These false detections were then easily manually removed and a final list containing 220 stars was generated. The median image was made using the 2009 K band data set. This epoch was used as an anchor for finding the differential proper motions of stars.

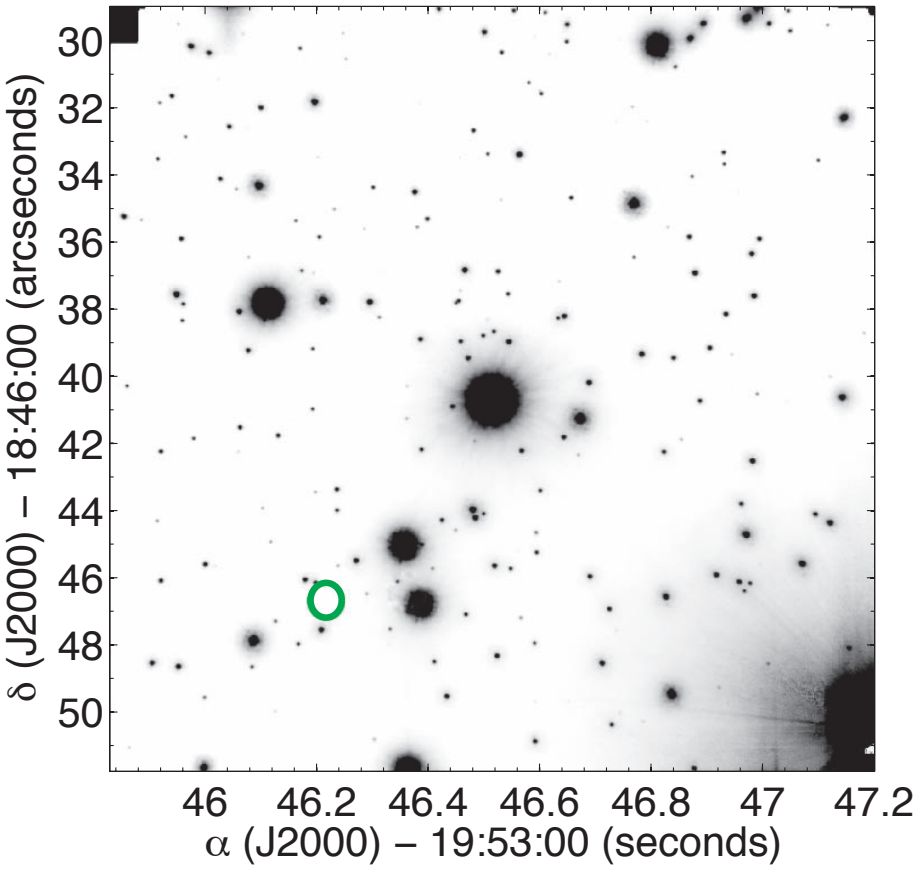

Figure 2.4: A median combined image using the NIRI/Altair adaptive optics image in the K band. The green circle represents the cluster centre and the size of the circle represents the approximate uncertainty. Note this image has been rotated compared to figure 2.3.

2.4.2 Making the Point Spread Functions

While running the IMEXAMINE routine to check the FWHM of the objects as mentioned in section 2.4 it was noted that stars close to the edge of the frame had distorted shapes while stars closer to the centre had well define concentric ring shapes as seen in Figures 2.5 & 2.6. This is a result of anisoplanatism, that is stars near the edge of the field appear distorted compared to those in the centre. Anisoplanatism is a result of the limitations of adaptive optics. The corrections made for the stars at the centre of the field are not necessarily the same as the edge of the field. As the shapes of the stars varies across the frame the point spread function (PSF) was modeled in a way so it would also vary across the frame.

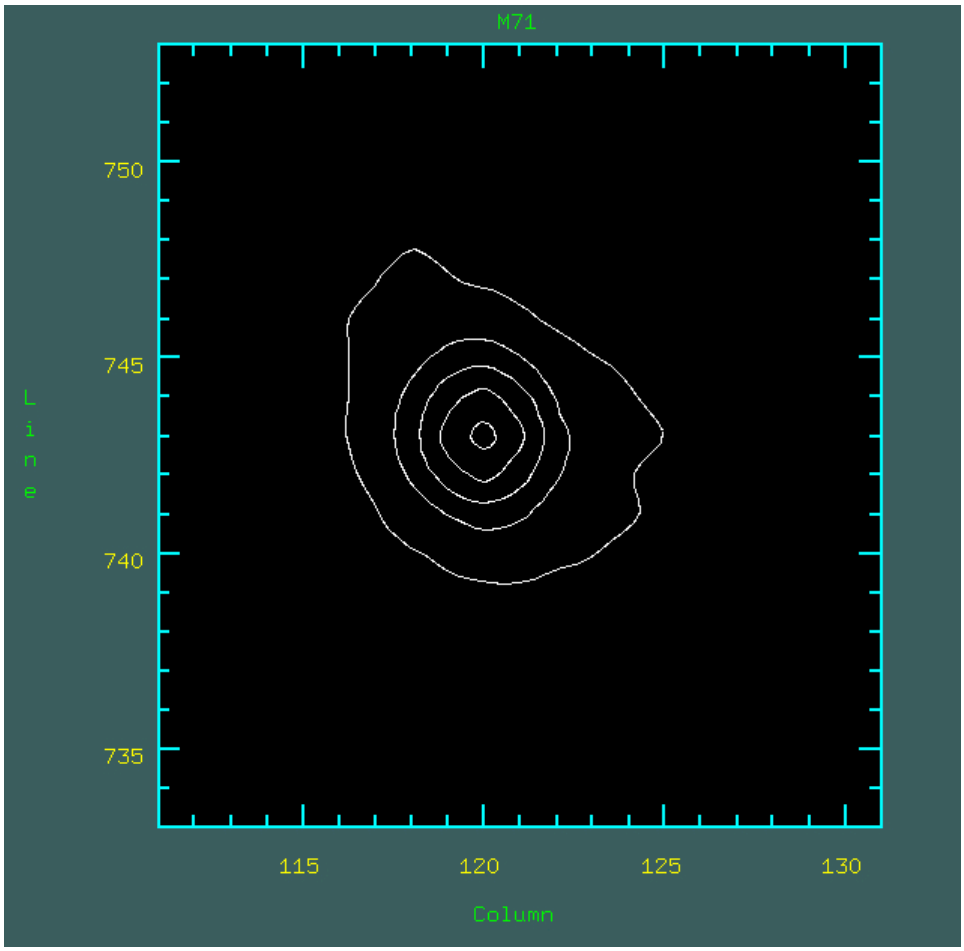

Figure 2.5: A contour plot of a star's intensity near the edge of the field

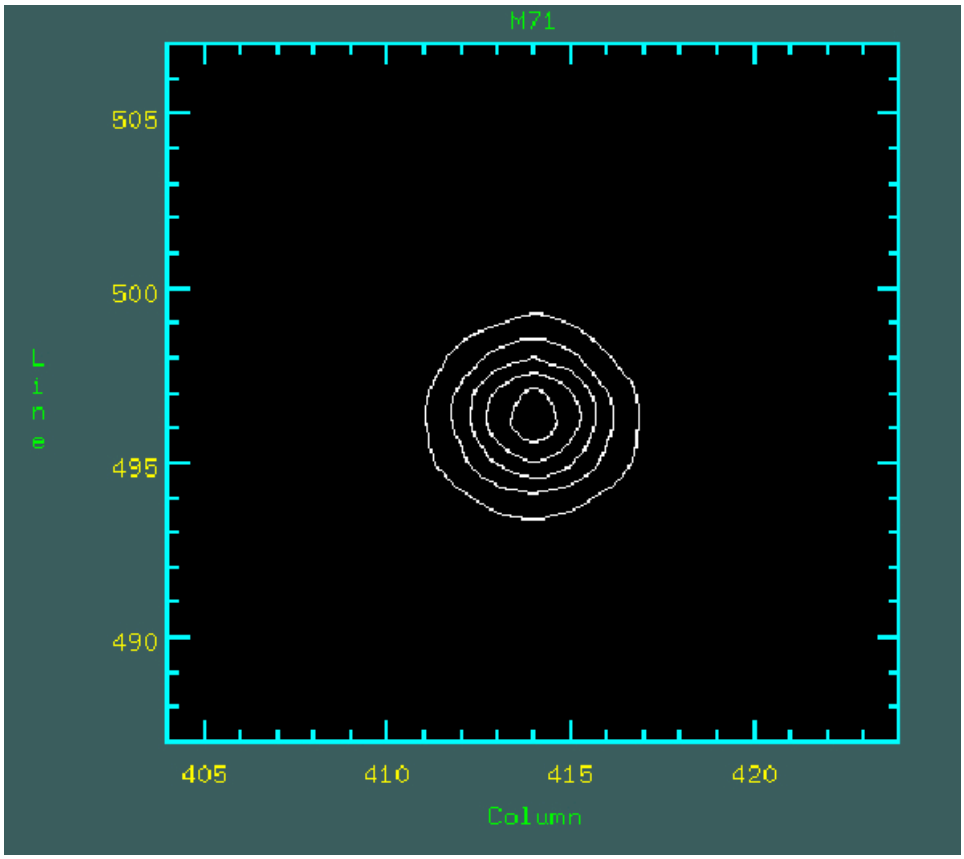

Figure 2.6: A contour plot of a star's intensity near the centre of the field

As the stars from the coordinate and the aperture photometry lists were already registered on the same coordinate system, the task of making the PSFs was dramatically easier. Candidate stars were selected automatically via DAOPHOT's PICK routine which outputs a list of possible good PSF stars. The PSF candidate stars were then examined to see if they were suitable candidates, with the unsuitable stars being removed. Unsuitable stars were either saturated, near the frame's edge or were in close proximity to a neighbouring star. Once a good list of PSF stars were generated, PICK was run on all of the frames from all available datasets. To construct the PSF, it was determined that using a three free parameter Moffat function would produce the best results. This was set by changing DAOPHOT's ANALYTICAL MODEL PSF parameter to 2.00. For a full discussion on

the PSF steps, see the DAOPHOT II user's manual [27]. To test the quality of the PSF, science images had their stars subtracted. A good subtraction would render sky background in place of every subtracted star.

2.4.3 Running ALLFRAME

ALLFRAME was the final step in the data processing procedure. The program requires four types of files to run: the file containing the transformation constants (§ 2.4), the master finding list (§ 2.4), individual PSFs for each frame (§ 2.4.2) and ALLSTAR headers for each file. To generate the ALLSTAR headers, run the ALLSTAR task and input the image, corresponding PSF and the aperture photometry file. ALLSTAR outputs a file that contains values of the read noise, gain, high and low good data values and the fitting radius for the frame. Once all of these files are ready, ALLFRAME is ready to run.

To get the astrometric positions of the stars, ALLFRAME is run in groups of ∼20 files separately for each epoch with the same master finding list. This results in ∼8 positions of each object for each imaging epoch. ALLFRAME performs PSF photometry on all of the frames and calculates the positions and magnitudes of the objects identified in the master finding list. The output is a file that contains the averaged positions and magnitudes. To find the position of a star in each of the three imaging epochs, the average of the ∼8 positions was taken and the error was the 1 standard deviation of the positions. See figure 2.7 for the position of one star across the three imaging epochs.

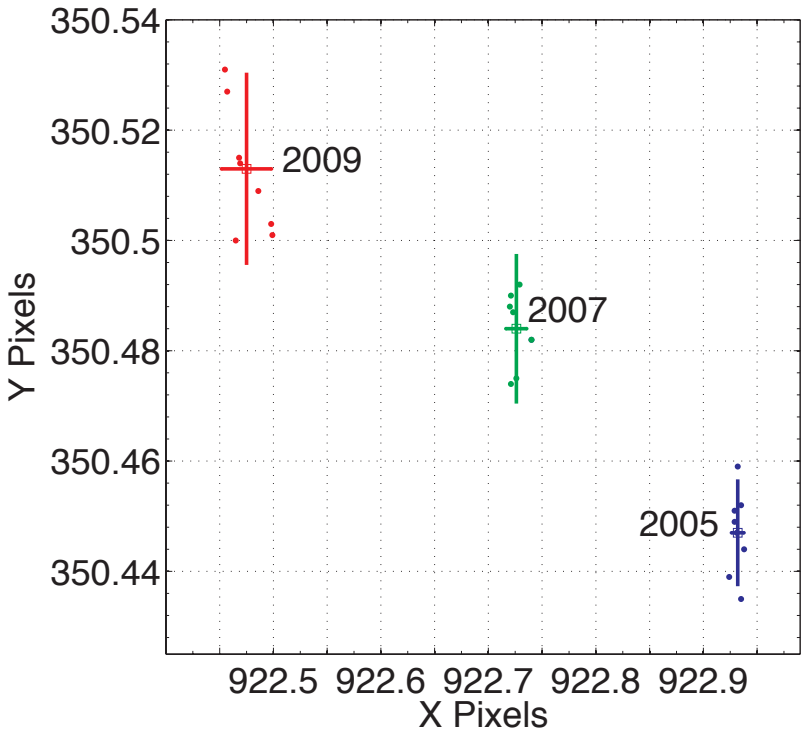

Figure 2.7: The relative location of one cluster member across the field in each of the three imaging epochs. The colored dots represent the derived locations from each ALLFRAME run. The error in the final position is determined from the spread in the points for each epoch.

Once the astrometric positions and errors in position were found for each of the 220 stars in the NIRI field, we determined the proper motions. To calculate proper motions, linear time dependent curves were fit for each star's position across the field. The best fitting slope gave the proper motion in x and y. To get the error in the proper motion, the position of the star in x and y for each epoch was chosen randomly weighted via the error in position. In other words, if a star has position x and error δx the new position was x' but it had a 68% chance to remain 1σ from its calculated position x and a 95.4% chance to be within 2σ of x.

After the determination of the differential proper motions of the 220

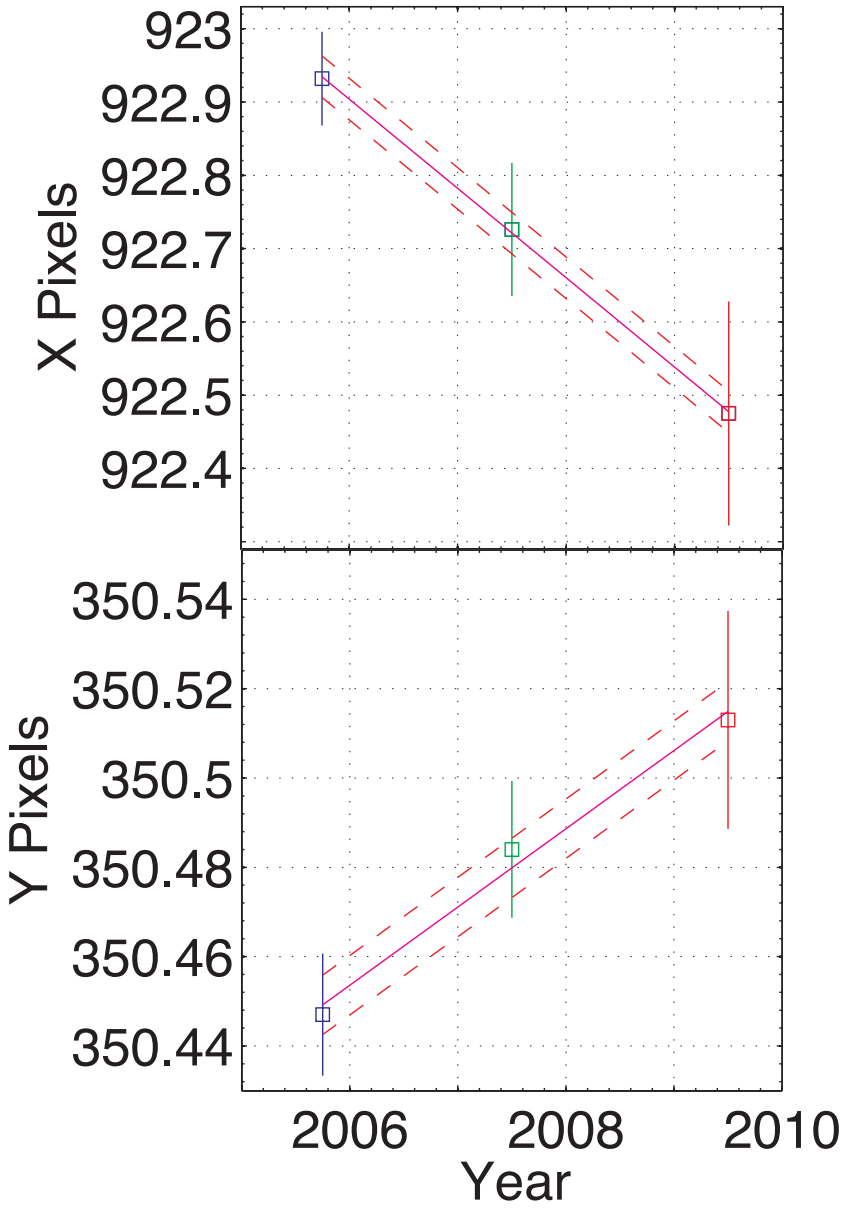

Figure 2.8: The X and Y positions of the same star as a function of time. The proper motion was found from fitting a straight line through those points, the slope of the line multiplied by the NIRI f/32 plate scale gives the proper motion. The dashed lines represent one-sigma errors.

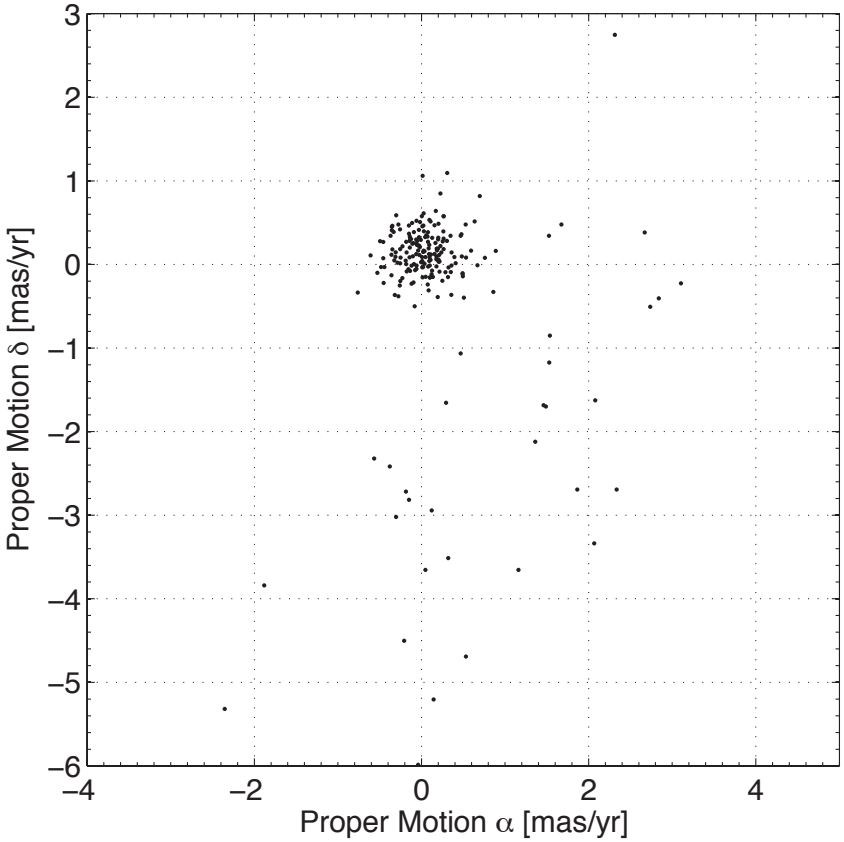

Figure 2.9: Proper Motion plot for 220 stars in our NIRI field. The motions have been corrected for right ascension and declination.

stars in our field, it was now possible to construct a proper motion diagram. Figure 2.9 shows the proper motions in right ascension and declination for our stars. The swath of stars running diagonally from the bottom left to upper right are likely galactic field stars.

Chapter 3

Analysis of Proper Motion Data

In this chapter we show the steps for the analysis of our proper motion data. Majority of this chapter was published in Samra et al (2012) [22].

3.1 Sample Selection

3.1.1 Improving the Photometry

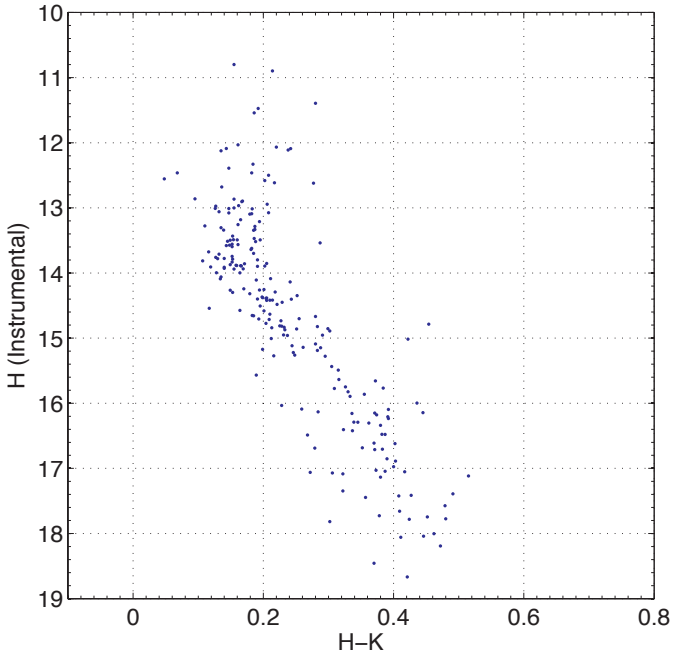

Figure 3.1: Colour Magnitude Diagram of the NIRI field

One of the caveats of studying stars in the core of a globular cluster is the possibility of finding stars ejected by interactions with a possible central black hole. Therefore, for selection of stars for our analysis we could not simply select stars from the proper motion sample alone. Instead we decided selection would be based upon a star's position on a cluster's colour magnitude diagram.

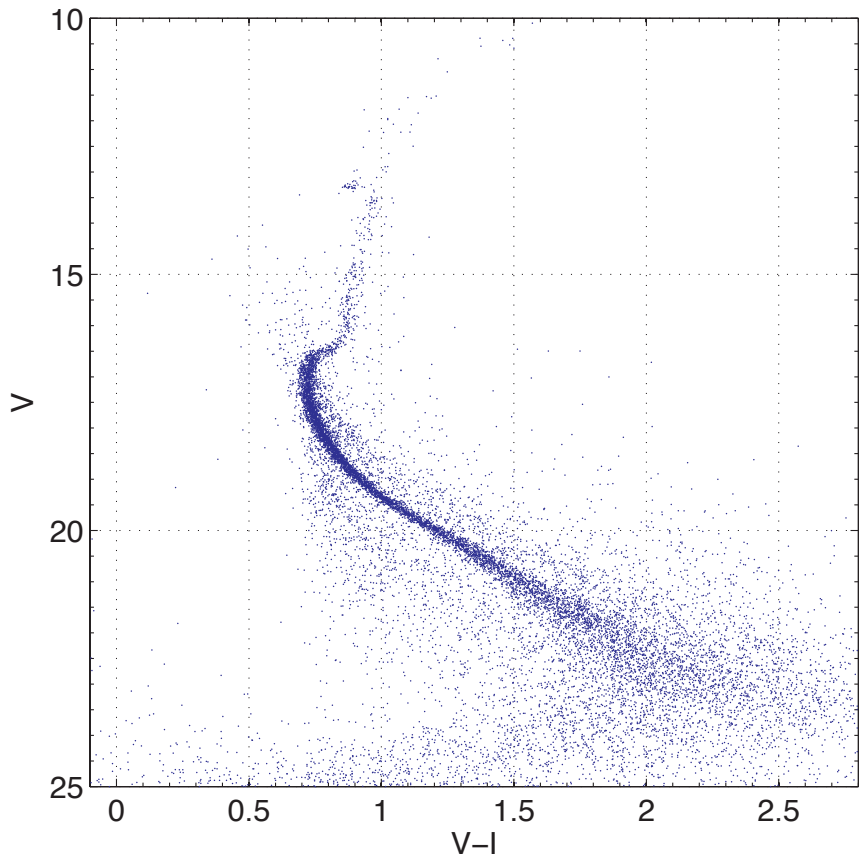

Figure 3.2: Colour Magnitude Diagram of Messier 71 obtained from the ACS Survey of Globular Clusters. The field here is the same from figure 2.2.

From our NIRI data we had photometry in the infrared filters H and K. As there is very little separation between the two filters in wavelength space, our colour magnitude diagram was very narrow in colour space. Figure 3.1.1

shows the infrared CMD for our data. From this, it is difficult to determine which stars are field or cluster members. Fortunately, the Hubble Space Telescope had conducted observations of M71 during the ACS Survey of Galactic Globular Clusters ([1, 23]). We matched our NIRI stars with stars from the ACS using the Daophot routine DAOMASTER and obtained V and I photometry for 215 stars in our NIRI field. Figure 3.2 shows the CMD of the entire cluster.

A previous proper motion study of M71 was performed by Cudworth (1985) [6]. We used the 358 stars listed in that paper's table to verify our proper motions. We first matched Cudworth's stars to the ACS photometry to obtain colors for 208 stars. The resulting CMD can be found in figure 3.3.

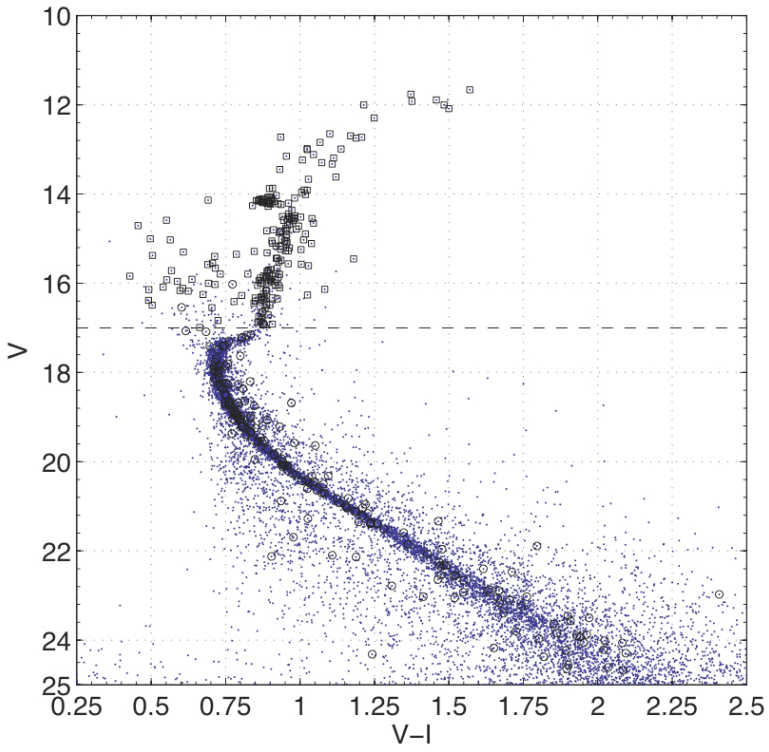

Figure 3.3: Colour Magnitude Diagram of Messier 71 obtained from the ACS Survey of Globular Clusters with the stars from our NIRI field (black circles) and the ones from Cudworth (black squares). The line at V = 17 is the limit for both datasets. For the NIRI data all stars brighter than 17 were saturated, whereas for Cudworth's data V = 17 was the limit for detecting stars

3.1.2 Colour Cuts

As discussed previously, we did not wish to make a selection of stars based upon proper motion. It is possible that a star may have a proper motion which is capable of escaping from the cluster. Therefore, if we perform a strict colour cut, stars which are likely galactic field stars will be removed.

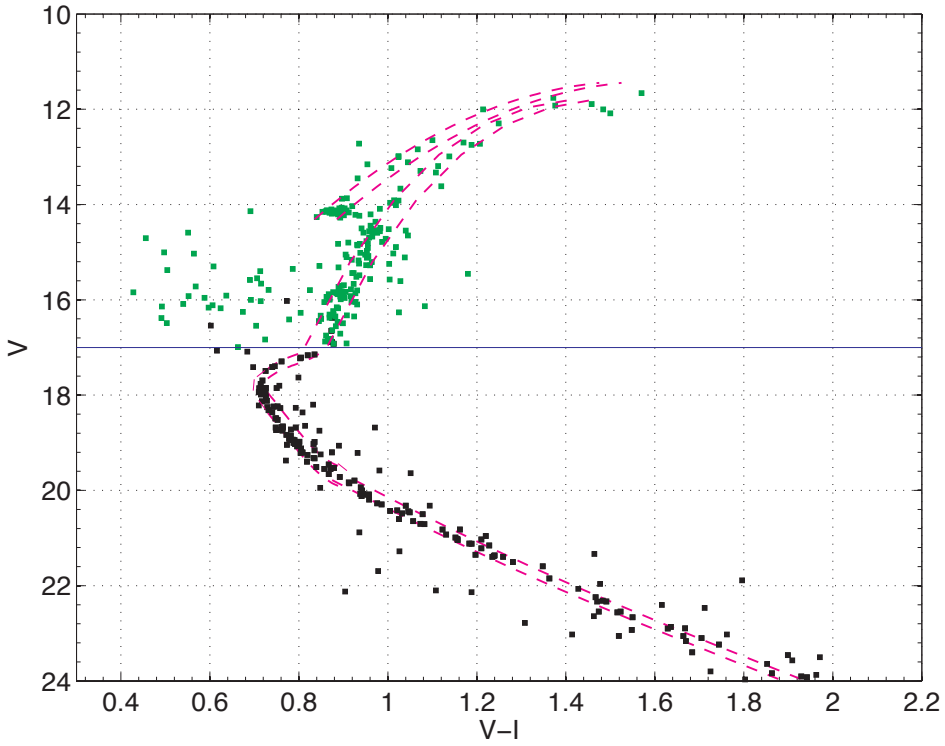

Figure 3.4: Colour criteria for our proper motion sample. The black points represent our NIRI field stars whereas the green stars are Cudworth's.

We used stars which had total proper motions less than 0.8 mas/yr (half the proper motion dispersion of all stars) to define a fiducial main sequence. Our cluster sample consists of all stars within 0.05 magnitudes in color of the main sequence fiducial. We then performed the same steps for Cudworth's stars (see figure 3.4). Stars were then removed based upon their errors from both the NIRI and Cudworth's winnowed samples. Stars which had proper motion errors greater than 2σ were rejected. This resulted in 150 cluster members for our NIRI field and 94 stars from Cudworth's sample. These 94 stars ranged in radial distance between $6''$-$150''$ from the cluster center, 2 of which were in our NIRI field for which we did not have proper motions due to them being saturated on our frames. Figure 3.5 has both our NIRI field proper motions and Cudworth's proper motions included. The final proper motion sample we used for this study are the stars in the right hand side figure.

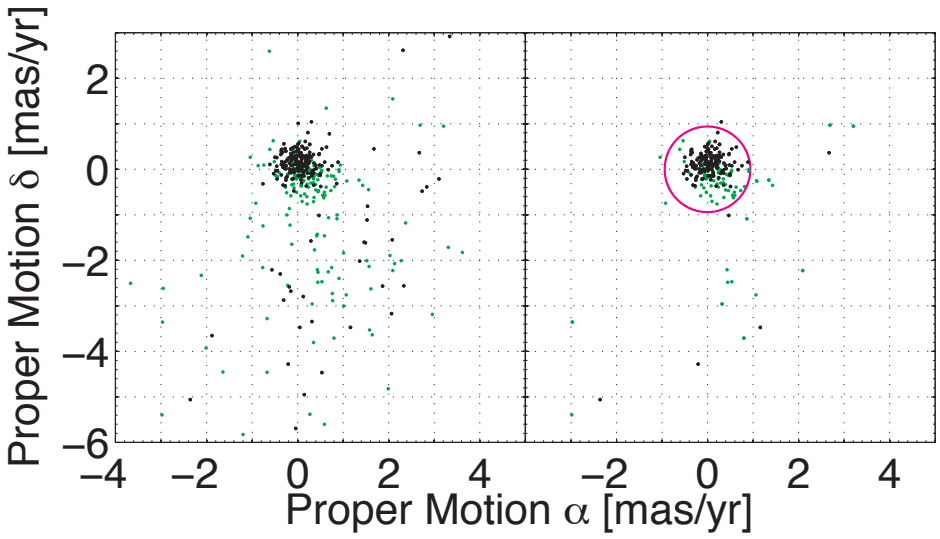

Figure 3.5: *Left:* Proper motions diagrams for both the NIRI field and Cudworth's stars for which we have ACS photometry. *Right:* The proper motions of stars which survived the colour cut and the subsequent error cut from figure 3.4. The circle represents the cluster's escape proper motion. As with figure 3.4 the black points are our proper motion data whereas the green are Cudworth's.

3.2 Proper Motion Distribution

To quantify the velocity dispersion of the cluster, one is tempted to use the standard deviation. However, a single high-velocity interloping star in the sample can skew the standard deviation to arbitrarily large values. Therefore we seek an estimator of the dispersion that is robust to outliers. Some familiar robust measurements of scale are the inter-quartile range (IQR) and the median absolute deviation (MAD). The IQR is the difference between the 75th and 25th percentile of the data whereas MAD is the median of the absolute values of the difference between the data values and the overall median of the data set. Rousseeuw & Croux (1991) [20] propose Q_n, motivated by two of its strengths — its ability to deal with skewness and its efficiency with gaussian distributions. It is defined over all the pairs of stars in the sample,

$$Q_n = a \times \text{first quartile of } (|\mu_i - \mu_j|) : i < j) \tag{3.1}$$

where a is a constant dependent upon the size of the sample (for large samples $a \to 2.2219$) and μ_i and μ_j are observed proper motions in a particular direction of pairs of stars in our sample. One further advantage of the Q_n estimator is that it approximates the standard deviation for distributions which are significantly different from normally distributed distributions such as those close to a uniform distribution. We treat Q_n as a proxy for the standard deviation for the remaining analysis. For example, we correct for the errors in the observed proper motions from the estimated errors to arrive at the proper motion dispersion:

$$Q_n^2 = Q_{n_o}^2 - \frac{1}{N}\sum \epsilon_{\mu_i}^2 \tag{3.2}$$

where Q_n is the error corrected dispersion, Q_{n_o} is the observed non-error-corrected proper motion dispersion and ϵ_{μ_i} is the error associated with the proper motion of each star. The error in the dispersion was calculated by bootstrapping the proper motions and their errors 100,000 times and taking the standard deviation of the bootstrapped dispersions. This results in a one-component core dispersion of $Q_n = 179 \pm 17$ μas/yr. Using the familiar standard deviation method to calculate the dispersion, we obtain a value of $\sigma = 185 \pm 18$ μas/yr, that is after removing stars with proper motions greater than the cluster's escape proper motion.

We used Cudworth's stars (see the right panel of figure 3.5) to determine the proper motion dispersion for stars which had radial distances greater than our NIRI field and were likely cluster members. We found for stars in the inner $70''$, the dispersion was 184 ± 37 μas/yr. For stars with distances greater than $70''$ and up to $150''$ the dispersion was 281 ± 33 μas/yr. These results are similar to the published values from Cudworth's paper [6].

At the distance of 4 kpc, our proper motion corresponds to a velocity dispersion of 3.3 ± 0.4 km/s, a value greater than the radial velocity dispersion of 2.0 km/s obtained by Rastorguev & Samus (1991) [17] and 2.8 ± 0.6 km/s from Peterson & Latham (1986) [16]. However, those velocity dispersions were calculated for giant stars which were far away from the center of the cluster; a constant dispersion is still within the uncertainties.

Equating our measured proper motion dispersion to the velocity dispersion from [16] we arrive at a geometric distance to the cluster at 3.47 ± 0.84 kpc. Although it is consistent with previous distances it is risky to equate dispersions from radially different locations in the cluster, and it is expected that the dispersion may change over a large radial distance. To get a much more accurate distance one would have to use the same stars for radial velocities as well as proper motions. However, we will explore this further in

chapter 5.2.

Relaxation Time

We can then use the observed velocity dispersion and stellar density to estimate the relaxation time in the NIRI field. Spitzer (1987) [25] gives the general form for the relaxation time to be

$$t_r = \frac{v^3}{1.22n(4\pi G^2 m_*^2)\ln(0.4M/m_*)} \tag{3.3}$$

where v is the projected root mean square velocity, n is the number density of stars in the field, and m_* is the typical mass of a star, taken to be ~ 0.5 $M_\odot$. This results in a relaxation time of $\sim 39 d_4^6$ Myr (where d_4 is the distance to the cluster divided by 4 kpc). This value is close Harris' estimated core relaxation time of ~ 34 Myr. However, if we factor in the $\sim 20\%$ discrepancy in the distance estimations, the relaxation time can be as little as 21 Myr or high as 70 Myr.

3.2.1 High Proper Motion Stars

From the CMD in figure 3.4, we find 6 stars in the NIRI field which have high proper motions and survived the winnowing and error cuts. If any of these stars are escaping the cluster, we could determine the cluster's evaporation timescale purely from observations. However our observed field lies at low Galactic latitude ($b = -4.56$ degrees), therefore the field may be subject to heavy contamination from the Galactic field as noted by [6]. To check for possible interlopers, we used the Besançon models of stellar population synthesis of the Galaxy from Robin et al (2003) [19]. The models depend on the Galactic coordinates, field size, photometric colors, and the extinction. The value for extinction in the direction of M71 was found to be 0.19 mag/kpc which was calculated using the reddening constant of 3.14 ± 0.10 from Schultz (1975) [24], the distance, and the reddening from Harris (1996) [13]. For a field 100 times the area of our NIRI field, the model yields about 5800 stars, 625 of which lie on our cluster's main sequence. Therefore we can expect $6-7$ of the stars in our NIRI field to be interloping field stars (see figure 3.6). It is therefore difficult to conclude if we have found any escaping stars.

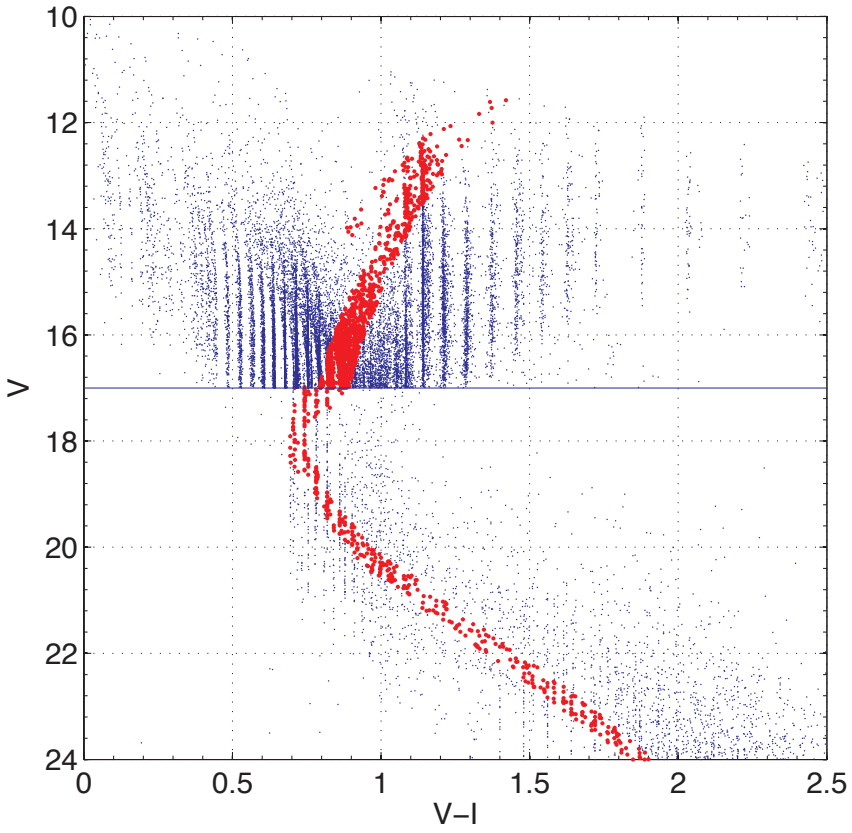

Figure 3.6: A simulation of the galactic field for the same galactic coordinates of M71. For stars with V $\leq$ 17, a field 100x the ACS field was simulated. For stars V $\leq$ 17 a field 100x our NIRI field was simulated. The red stars are the ones that meet the colour cuts from figure 3.4.

We also ran a simulation for a field 150x the size of the ACS field; we found $\sim$1900 stars in this simulation which lie on the winnowed CMD for Cudworth's stars. Scaling this down to the ACS field we expected to find $\sim$13 interloping stars. From the proper motion distribution we found 16 potential escapers. It is once again difficult to conclude we had observed any escaping stars.

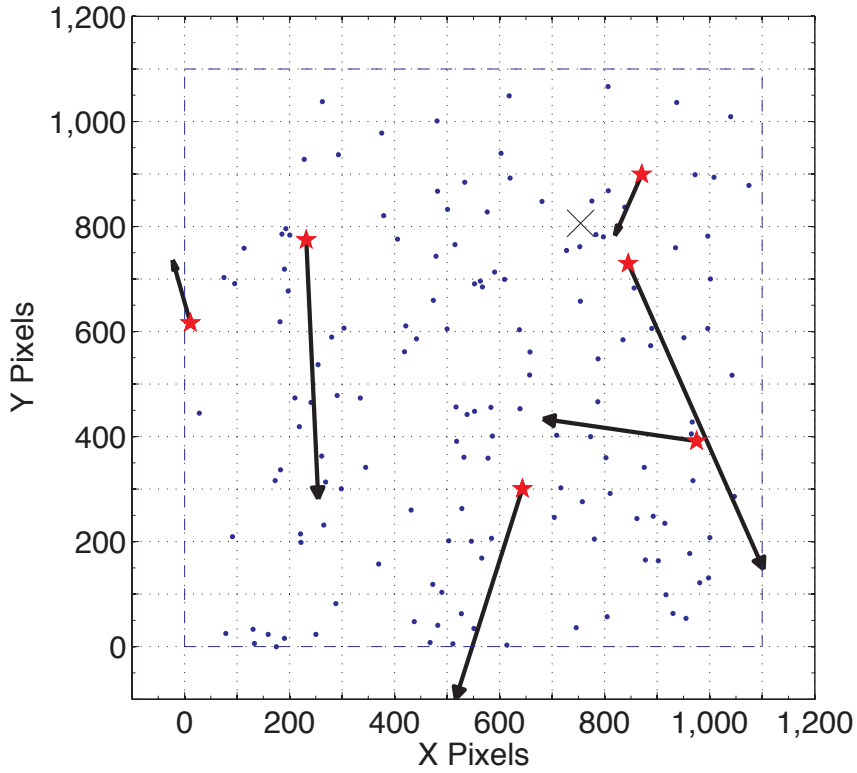

Figure 3.7: The proper motion vectors for the escaping stars that survived the color and proper motion error cuts. The vectors are plotted to show the trajectory of the stars over the next 5000 years. The X marks the centre of the cluster.

3.2.2 Proper Motion Isotropy

Using the proper motion data, we determine the proper motion vector of the individual stars in the cluster. We calculated the proper motion angle with respect to the cluster center for three groups of stars. Half of the NIRI field contained stars within 11″. The other half were from 11-22″. We also calculated the angles for stars from Cudworth[6], which we determined to be cluster members. We found that stars in the three different radial distances had proper motion angles which were consistent with isotropy.

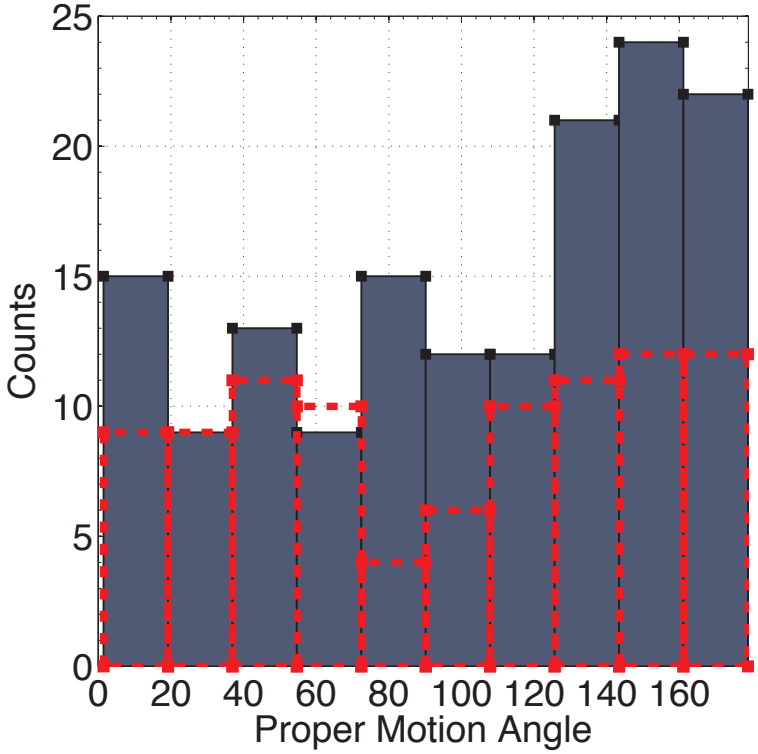

Figure 3.8: Histogram of the proper motion angle with respect to the center of the cluster. Blue histograms are for stars in the NIRI field, and the dashed red line histogram is for stars from [6].

We performed a Kuiper test on the data from figure 3.8, which is a test similar to the Kolmogorov-Smirnov test but more sensitive to differences in the wings of the distributions. This test is better suited for distributions which are cyclic in nature as in our case. The $p-$value, comparing a flat distribution, is 0.17, for stars in the inner $11''$ and p=0.21 for stars in the outer $11''$, finding no significant difference when compared to a flat isotropic distribution. We have a similar result when we extend our field from the inner $22''$ up to $150''$. We then have a p-value of 0.14. Figure 3.8 shows the distributions of proper motion angles for the NIRI field and from Cudworth.

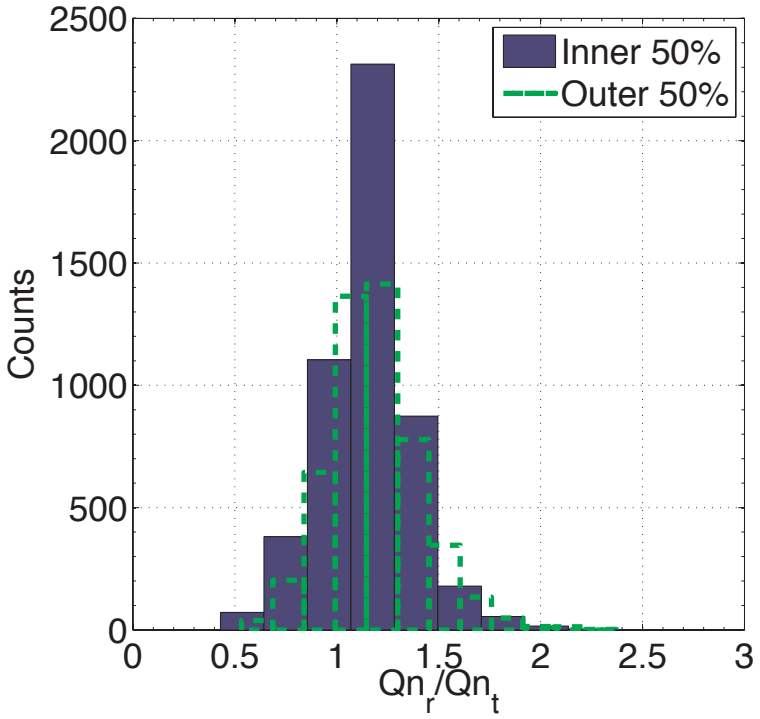

Figure 3.9: Histograms for the values Q_{n_r}/Q_{n_t} resulting from the bootstrap resample of the data. The radial and tangential values of Q_n are consistent with unity within 1σ for all stars.

As we transform coordinates between the multiple epochs, we use cluster stars as the reference points. Therefore, any mean motion of the cluster is lost. To characterize the anisotropy of the proper motions, we measure the width of the proper motion distribution in the radial and tangential directions using Q_n. The measured ratio of the radial to tangential widths Q_{n_r}/Q_{n_t} is unity for an isotropic distribution. We find the ratio of the two components Q_{n_r}/Q_{n_t} for three radial distances. For the inner 50% we have $Q_{n_r}/Q_{n_t} = 1.15\pm0.22$ and $Q_{n_r}/Q_{n_t} = 1.17\pm0.23$ for stars for the outer 50% of the NIRI field. If we extend our field up to $\sim150''$ we have Q_{n_r}/Q_{n_t} $= 1.03\pm0.13$. The errors were obtained by bootstrapping our sample of measured proper motions, and accounting for errors in the cluster's center and proper motions. Although the results for stars in our NIRI field are above unity and may indicate a stronger radial component in the proper motions, both results are still within 1σ of unity. Figure 3.9 shows the

distributions of the ratios of the radial and tangential dispersions from our NIRI field.

3.3 An Upper Limit to the Mass of any Central IMBH

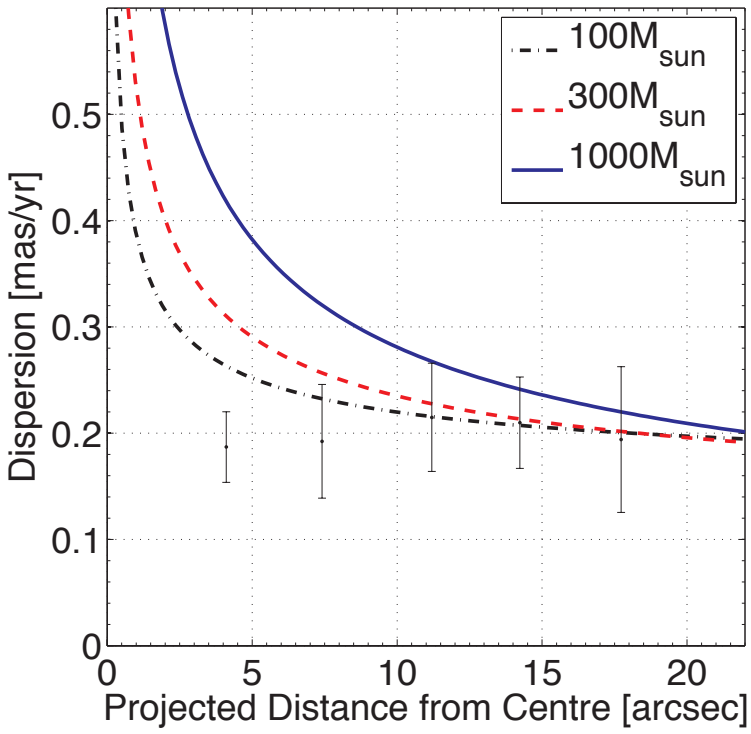

Figure 3.10: The observed proper motion dispersion and three different IMBH models.

IMBHs have been suggested to exist in several globular clusters such as G1 [9, 29], NGC 6388 (Lützgendorf et al) [14], and Omega Cen (Noyola et al)[15]. However, some of the claims are still disputed, notably the claim in Omega Cen (Anderson & van der Marel)[2]. Safonova & Shastri (2010) [21] extrapolate the SMBH correlations down to GC masses, determining a linear relation in the velocity dispersion and central black hole mass. Using their relation and our observed velocity dispersion, we obtain an upper limit

of a central black hole mass of 25 $M_\odot$ for M71. It is risky, however, to extrapolate correlations between SMBHs down to IMBHs as their formation scenarios might be significantly different. To determine if we have observed any evidence for a central IMBH in the core of M71, we divide our proper motion data for stars in the inner 22″ into 5 radial bins. Each bin contains 30 stars. We then calculate the observed proper motion dispersion (Equation 3.2) and estimate the errors by bootstrapping and calculating the spread in the values of Q_n (see Figure 3.8). The observed proper motion dispersion is nearly constant throughout the inner 22″.

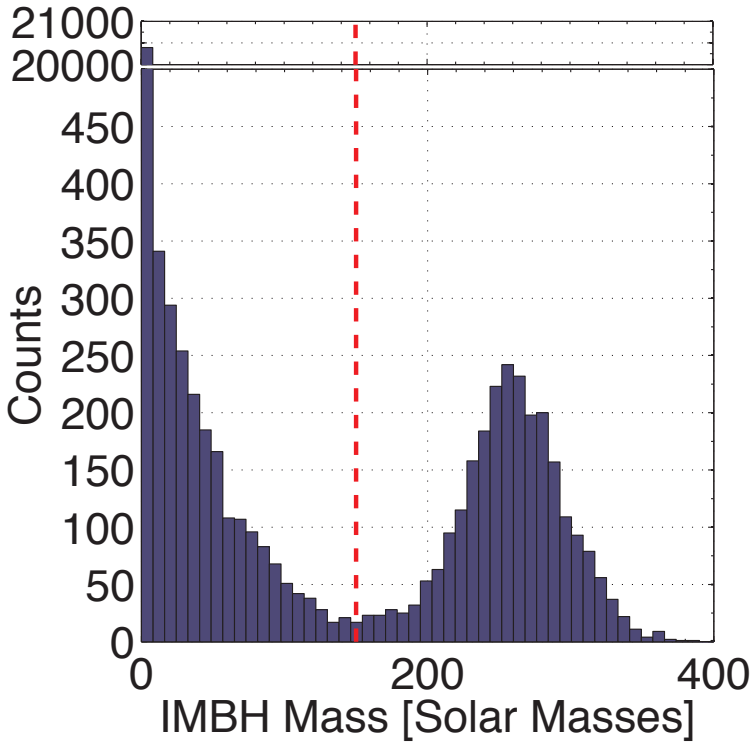

Figure 3.11: The results from bootstrapping the proper motion data 25,000 times. The IMBH mass from each fit is binned here. The leftmost bin from $0 \leq M_\odot \leq 5$ peaks at 20,500 counts, implying that a very small central IMBH is the preferred fit. The red line represents the 90th percentile at $150M_\odot$.

We have found that the velocity dispersion calculated by Baumgardt et

al (2004)[4] in clusters with a black hole at the center can be modeled simply as a function of the cluster half-light radius for stars which are close to the cluster center. The resulting model contains an $r^{-1/2}$ Keplerian contribution from the black hole and a constant dispersion from the stars only. To quantify our results, we bootstrap the observed proper motions and fit them to our model by minimizing the χ^2 values and accounting for our error in the cluster center. Using these bootstrapped data we find with 90% confidence, that any black hole at the center of M71 must be less massive than $150 d_4^3$ $M_\odot$. Where d_4 is the distance to the cluster divided by 4 kpc. From the histogram in figure 3.11, the most common result is the one with a very small black hole, where the proper motion distribution is constant with radius. Near the 90th percentile, the value of σ from our model vanishes and the observed proper motions obey a Keplerian $r^{-1/2}$ distribution.

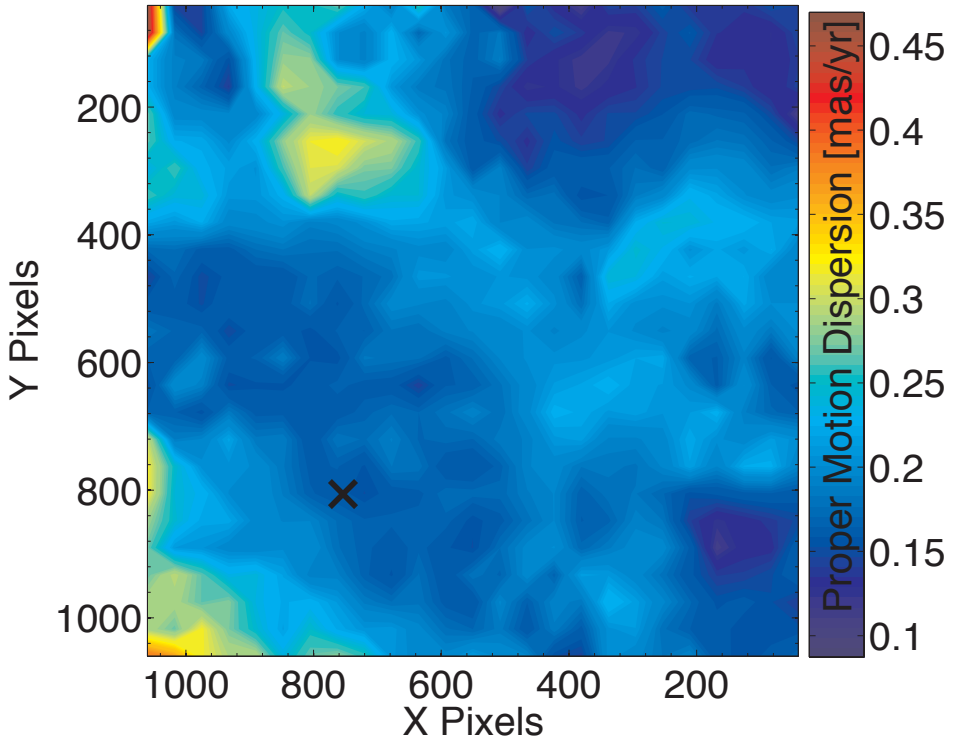

Figure 3.12: A dispersion map of the field, obtained by running a circle with a 4″ diameter across the field and calculating the dispersion in each area. Observationally, there are no signs of radial dependence or an increase in dispersion towards the center which is represented by the X.

One of the risks with binning data is that it is possible to over- or under-bin and mask or amplify any underlying features or noise. We approach this with two methods. First, we run a circular bin across our field and calculate the dispersion in each bin to produce a dispersion map. Figure 3.12 shows this map and it is clear the changes in dispersion are random fluctuations.

Another way to check if the observed dispersion is constant, as in the case for no or a low mass black hole, is to calculate the average distance from the center,

$$\bar{r} = \Sigma r / N \tag{3.4}$$

and compare it to the proper motion weighted distance from the center,

$$\bar{r}_{|\mu|} = \frac{\Sigma r|\mu|}{\Sigma|\mu|}. \tag{3.5}$$

If the proper motions are constant as a function of distance from the center, the two values should be equal. However, if proper motions are decreasing with increasing radial distance, larger radii get less weight so the value is less. We obtain $\bar{r} = 11.81'' \pm 0.47''$ and $\bar{r}_{|\mu|} = 11.50'' \pm 0.83''$. The proper motion weighted distance is lower, indicative of higher proper motions at smaller radii, but a radially constant velocity dispersion is completely consistent within the uncertainties.

3.4 Summary of Proper Motion Analysis

Using the Near Infrared Imager on the Gemini North Telescope we were able to resolve the internal proper motions in the core of Messier 71. With a 3.8 year baseline, we found proper motions for 215 stars, 150 of which are likely cluster members. Several of the stars exhibit high proper motions well beyond the cluster's escape velocity. However, we are unable to say with confidence that we have observed any escaping stars because of likely contamination from field stars. The cluster's proper motion dispersion was found to be 179 ± 17 μas yr^{-1}, a result similar to Cudworth (1985) [6]. By combining data from Cudworth, we are able to look for signs of anisotropy across the cluster's inner $150''$; however we find that the distribution is consistent with the case of isotropic orbits. We then find that the observed proper motion dispersion is constant with radius and we are able to put an upper limit to any central intermediate mass black hole to be less than $150 d_4^3$ M$_\odot$ at 90% confidence.

Chapter 4

Reduction of Integrated Field Unit Data

4.1 Introduction to Spectroscopy

Astronomical spectroscopy is the study of the spectrum of electromagnetic radiation from astronomical objects. This can be used to derive many properties of astronomical objects such as their temperature, chemical composition, density, luminosity, distance, mass and their relative motion via Doppler shift.

To obtain spectra of an astronomical source, a diffraction grating is used to disperse the incoming light. The light is then photographed using a CCD camera. Depending on the source, various gratings in combinations with filters are used to deliver the required science goals. Gratings can come in low, medium or high resolution. The resolution of a particular grating is denoted by R, a dimensionless quantity that is a measurement of spectral purity; $\mathrm{R} = \lambda/\Delta\lambda$. Here, λ is the wavelength of the observation and $\Delta\lambda$ is the smallest wavelength separation an instrument can distinguish. Spectrographs with $\mathrm{R} \leq 1000$ are considered low resolution. Low resolution spectrographs are useful for observing faint objects and will have large spectral coverage. Whereas, spectographs with $\mathrm{R} \geq 50{,}000$ are considered high resolution. High resolution spectrographs have the advantage of delivering precise velocities or very high resolution of an objects spectrum, but at the cost of low spectral coverage and increased telescope time.

The Doppler effect can be used to find the radial velocity of astronomical objects. The spectra of stars is not continuous. There are absorption features at known wavelengths. Absorption lines are created when electrons are excited between energy levels in the various elements found in a star's atmosphere. These features can then be compared to a gas of the same element which also exhibits the same spectral features, however the features are slightly shifted if the star is moving. This shift can be used to calculate the object's radial velocity via:

$$v_{rad} = c\frac{\Delta\lambda}{\lambda} \tag{4.1}$$

where c is the speed of light.

4.1.1 Different Types of Astronomical Spectroscopy

There are several branches of spectroscopy, depending on the instrument used and the science goals. Each has its advantages. Here we discuss three different types.

Long Slit Spectroscopy

Long-slit spectroscopy is used when observing an elongated celestial object through a elongated slit aperture and dispersing the light using a diffraction grating. This is particularly useful when observing extended objects such as galaxies and Herbig-Haro objects. For extended objects their rotation curve can be observed to give spatially resolved velocities. This technique can be used with high resolution gratings to deliver precise radial velocities. The drawback is only one object can be observed at a time.

Multi Object Spectroscopy

Multi-object spectroscopy allows for the possibility of obtaining spectra of up to several hundred objects simultaneously. This is done by precisely fabricating a plate with many small slits which is placed at the spectrographs' entrance aperture or by placing fibers in the telescope's focal plane.

Integrated Field Spectroscopy

Integrated field spectroscopy has recently become an important sub-discipline of astronomical spectroscopy. Traditionally, obtaining spectra of extended objects such as galaxies or many point sources such as stars in a small field, spectroscopy using a long-slit was carried out. This gave spatial resolution in the direction of the slit and the slit was then moved across the field for a second spatial dimension. However this process is slow and requires greater telescope time. Integrated field spectroscopes are used to speed up observations by obtaining spectra of a two dimensional field. Recently this has been sped up with improvements in telescope resolution and with advancements in adaptive optics.

Integrated Field Units (IFUs) work by using one of, or a combination of three methods: lenslet array, fibers or an image slicer. For a lenslet array, an array of small lenses is placed in the image plane essentially with the lenses acting as pixels of a standard camera. The incoming light is then fed to a dispersive element and imaged via a camera. This results in a spectra for each individual lenslet. For a fiber fed spectrograph, the incoming light is captured by an array of fibers before it is dispersed and imaged by a camera. An image slicer works by slicing an image in the image plane and rearranging it so that different parts of the image fall onto a slit and dispersive grating, so that a spectrum is obtained for a larger area of interest.

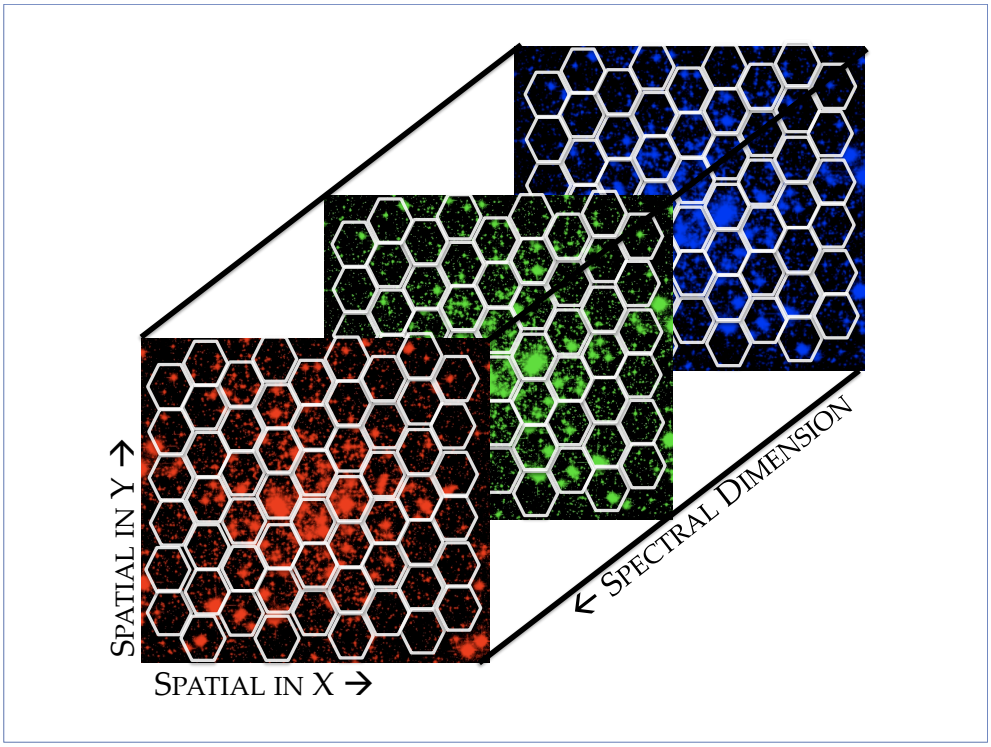

Figure 4.1: An example of how an integrated field unit (IFU) works. The hexagons represent lenslets which have the ability of capturing a spectrum individually.

4.2 Gemini Multi Object Spectrograph Integrated Field Unit

The Gemini Observatory has at its disposal, the Gemini Multi Object Spectrograph (GMOS), which can be configured for long slit, multi object or integrated field spectroscopy. Here we discuss the instrument and its capabilities when running the integrated field unit.

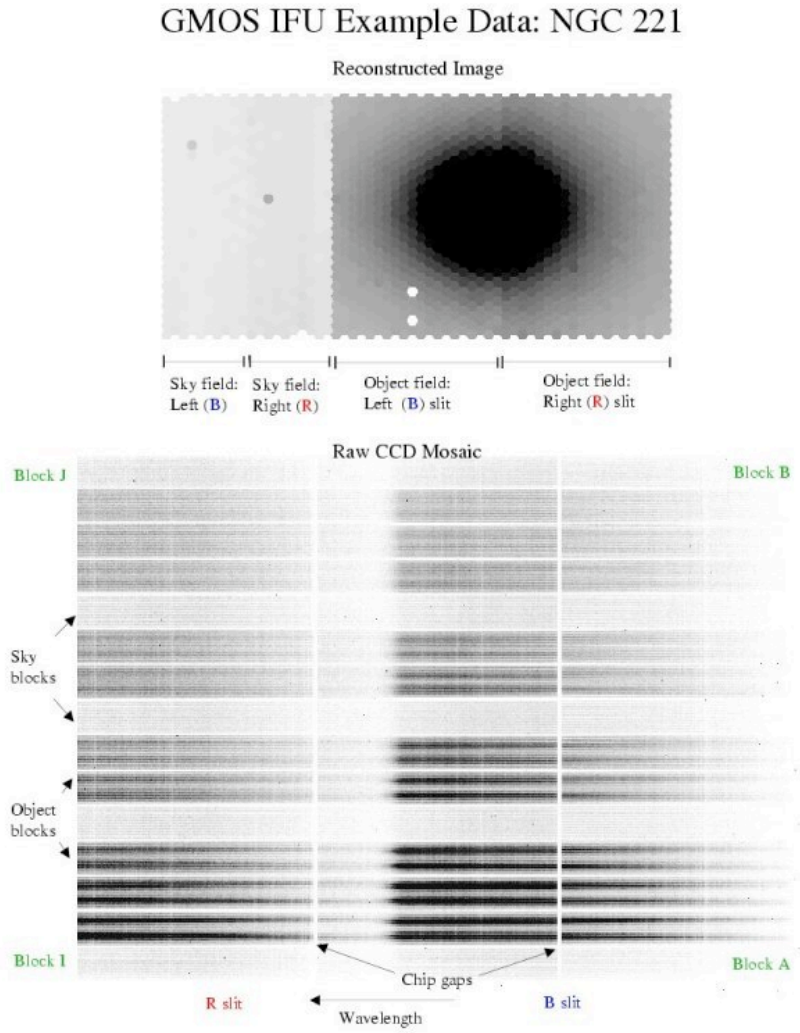

Figure 4.2: GMOS IFU example data of a dwarf galaxy. At the top is the reconstructed IFU image with the left panel showing the sky field. Bottom shows the raw CCD image. The sky and object fields are arranged into alternating blocks on the CCD. Also prominent in the image are the chip gaps between the three GMOS CCDs.

The GMOS IFU is an optical and near infrared spectroscope which covers a wavelength range from 400-1100 nm. The IFU has two imaging fields, one for the object of study and the other for the sky. They have a 1 arcminute

seperation. The IFU contains 1500 lenslets each of which projects 0.2″ onto the sky. The IFU can be run in two different modes, one-slit and two-slit. In one-slit, 500 lenslets are used for the object of study and yields a 5″ x 3.5″ field of view and a 5″ x 1.75″ sky field of view. This provides extended wavelength coverage at the cost of field size. In two-slit mode, all 1500 lenslets are used, 1000 for the object and 500 for the sky. This provides a field of view of 5″ x 7 ″ for the object and 5″ x 3.5″ for the sky. Figure 4.2 shows an example of a reconstructed GMOS IFU image of a dwarf galaxy. Gemini offers various combinations of filters and medium and low resolution gratings. This allows for observing specific spectral features on science data.

4.3 Messier 71 IFU Data

By using the Gemini GMOS IFU on M71, we are able to obtain spatially resolved velocities for stars in the core of the cluster. Previous studies have been conducted using an IFU to obtain radial velocities for stars in the core of globular cluster (e.g Noyola et al (2008) [15] & Lutzengdorf (2011) [14]). However, these studies always had stellar field densities much greater than ours. As a result no published study has been previously done in which individual radial velocities were measured for stars at the core of a globular cluster. M71's extended core permits the use of an IFU to obtain uncontaminated stellar spectra.

By using a medium resolution R = 5500 grating and the Calcium Triplet filter (see figure 4.3), the three Calcium Triplet lines in stellar spectrum can be observed. The triplet lines are found at λ = 850.036nm, 854.444nm and 866.452nm.

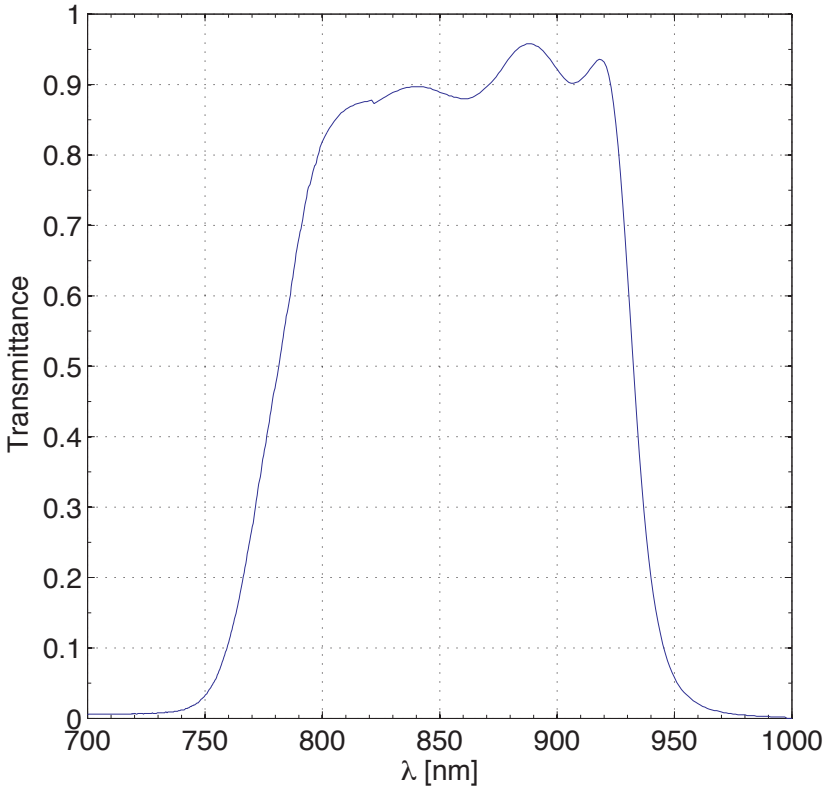

Figure 4.3: The transmission curve for the Calcium Triplet Filter at Gemini North

In 2009 we obtained six hours of observation time on the core of M71 using the GMOS IFU. The dataset was divided into six adjacent 5″x 7″fields with no overlap between the fields. Originally it was requested that each field be observed for one hour, however after we obtained data we found this varied between our six fields with some fields having twice as much observation time compared to others. In addition to IFU science data we were also supplied with daytime twilight flats, gemini calibration flats and Copper-Argon lamp flats for wavelength calibration. The data was were over the course of four nights on June 11 2009 and July 3-5 2009, with the twilight flats obtained only on June 11th. Additionally, the data were obtained at two central wavelengths of 855 nm and 865 nm. This was to minimize the chance that spectral features would be lost between the chip gaps in the CCD detector.

4.4 Reduction of M71 IFU Data

The reduction of IFU data was done using the Gemini IRAF package. This is the same package that was used for reduction of the NIRI data in chapter 2. After acquiring the data there are four types of data files in addition to science data. They are bias, twilight, Gemini calibration flat (GCAL) and Arc. These four calibration files are essential for the reduction of the science data.

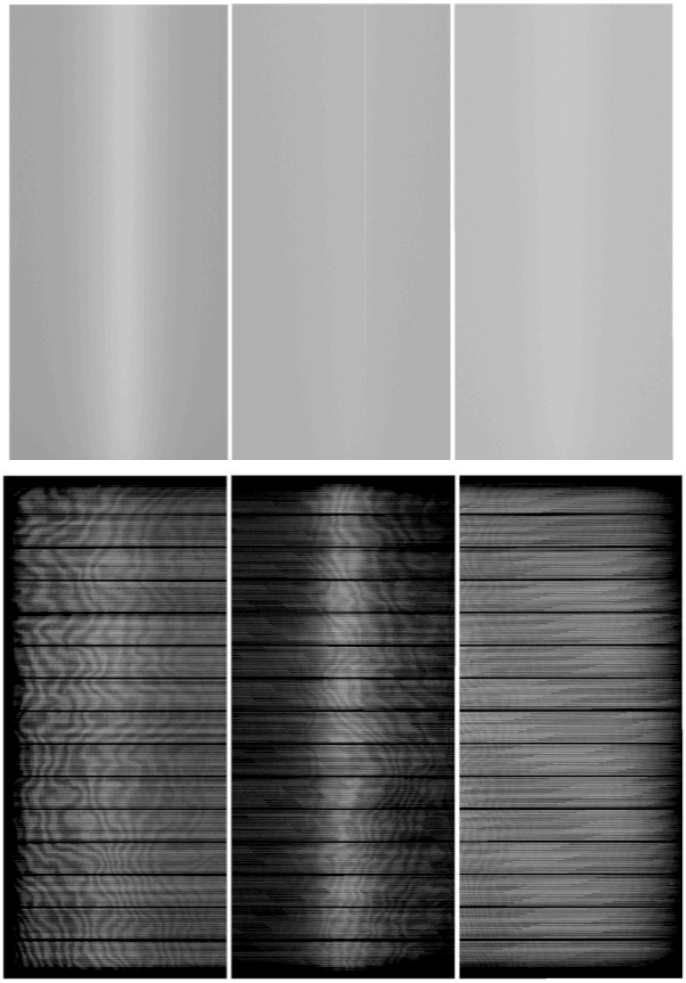

Figure 4.4: Examples of calibration images from the IFU. Top: The raw bias image supplied by Gemini. Bottom: A Raw GCAL flat from one of the nights of observations.

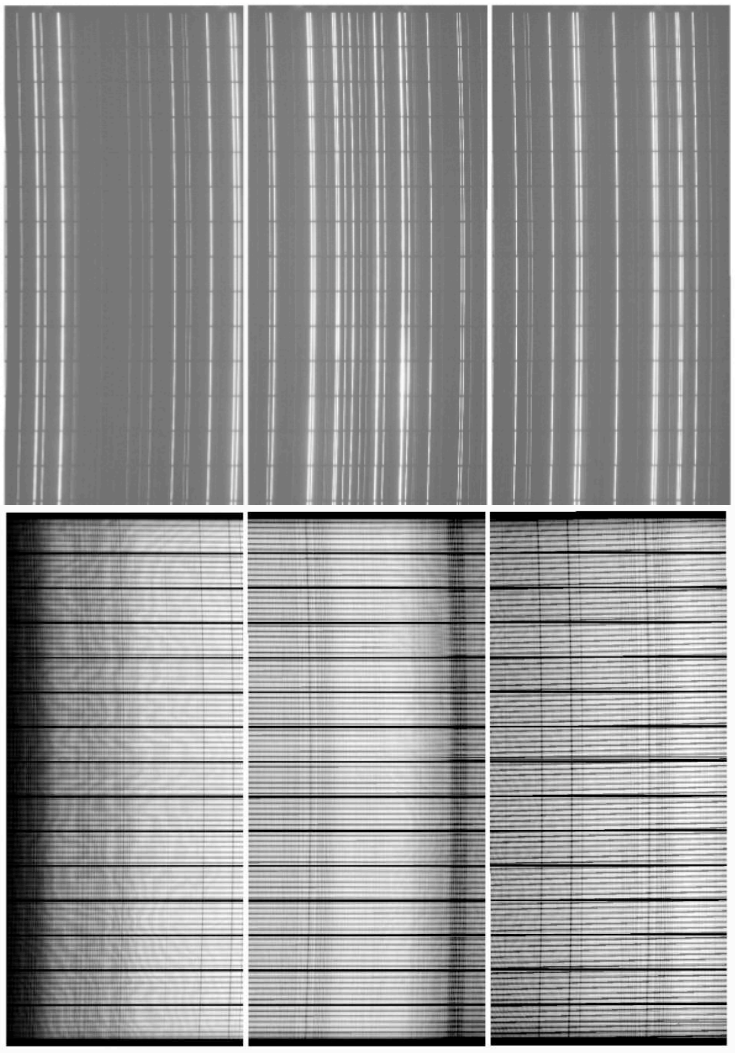

Figure 4.5: Top: Calibration Copper-Argon arcs. Bottom: The raw twilight image. There is a discontinuity in all IFU images in the centre chip. This is the location where the red slit's dispersion ends and the blue slit's starts.

The reduction of data was done individually on each of the images. This means that every night a new set of calibration images were obtained and those images were used for calibrating the science data. One concern with the data was the twilights were only obtained on the first night of observations. As a result, the same twilights had to be used for calibrations despite updated calibration flats and arcs from every other night.

The general IFU reductions are outlined in figure 4.6. This shows the sequence for reducing data. The numbers denote the steps performed during the data reduction. The primary IRAF task is GFREDUCE. This task has the ability for calling other Gemini IRAF tasks which can be controlled accessing the task's parameters.

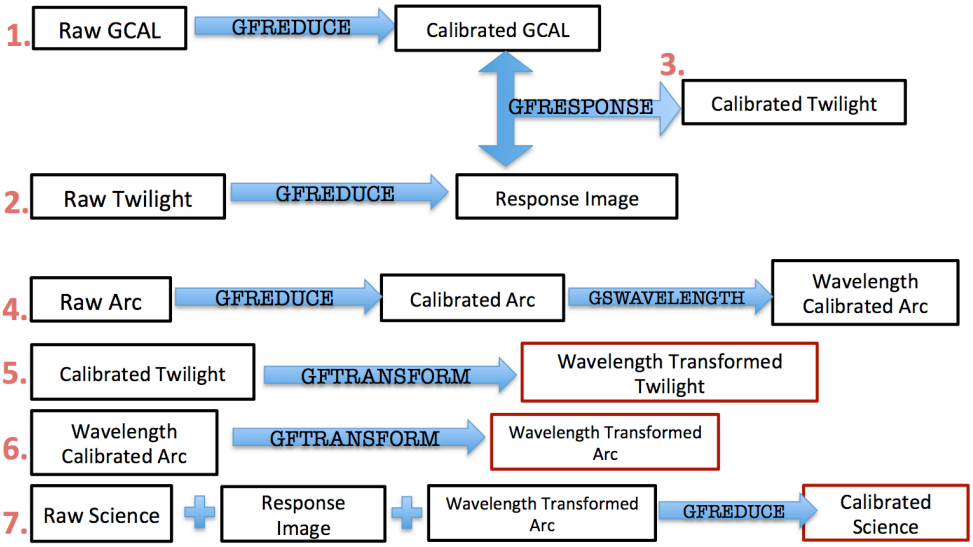

Figure 4.6: Flowchart detailing the steps for IFU data reduction. The arrows have the Gemini IRAF task required for the steps. The red boxes denote final reduced files required extracting science data.

The first task is to bias subtract, clip the images at the discontinuity in wavelength space then stitch the images to account for the chip gaps. There is a discontinuity in the images where the red slit ends and the blue slit starts (see figure 4.5). The top half of figure 4.7 shows the results of the first task. The second task was to perform the same steps as step 1, except this time on the twilight flat.

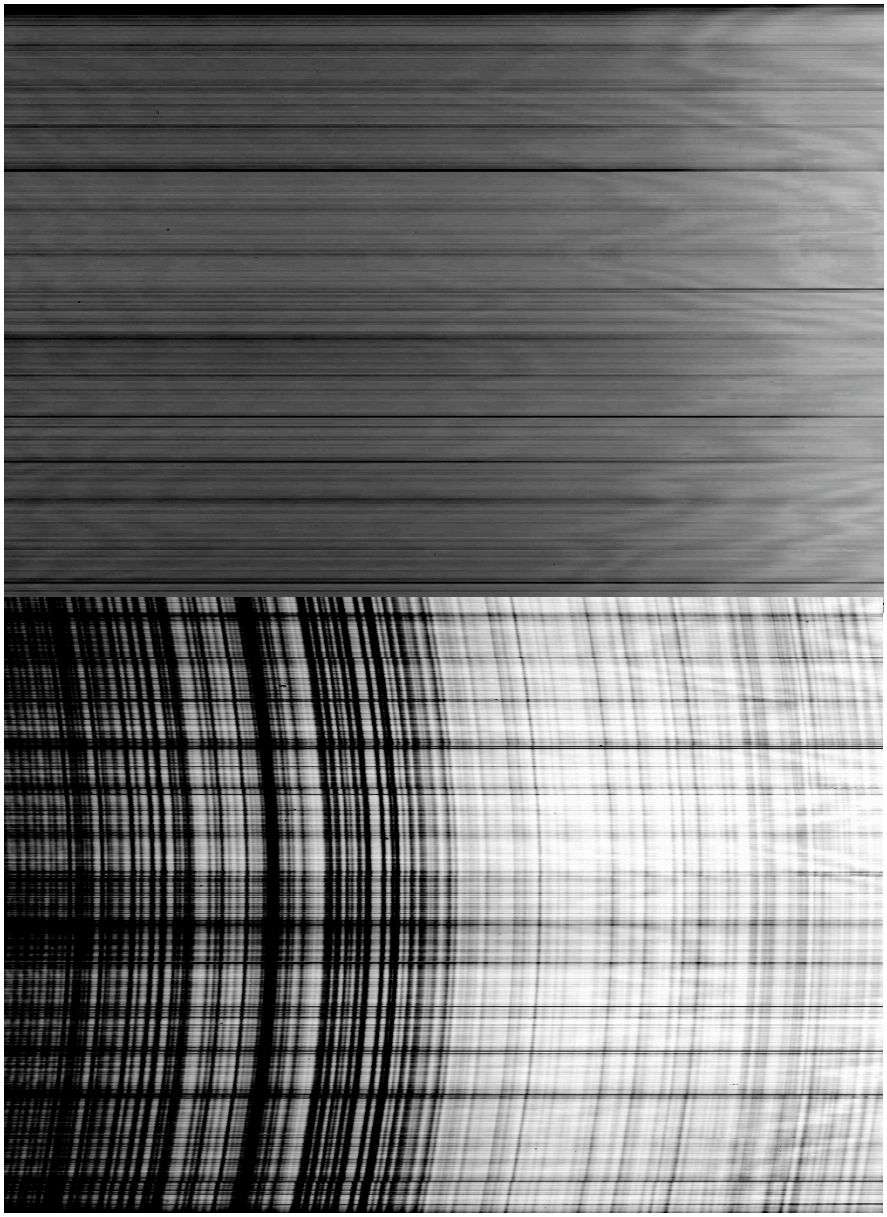

Figure 4.7: Top: The Gemini Calibration flat after the results of step 1 is seen above. The chip gaps have been accounted for and the two slits have been stitched together. Bottom: The reduced twilight flat prior to wavelength calibration.

Step 3 is to use both the reduced calibration and twilight flats to create a final flat field image. This flat field image would be applied to the science data for final reductions. Figure 4.8 shows the final response image.

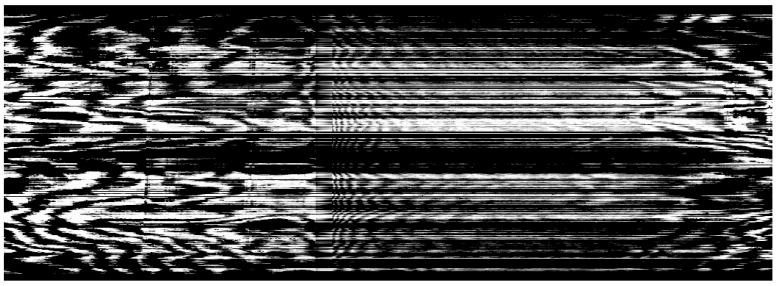

Figure 4.8: The response image. This is the final flat field.

One of the most critical steps in the IFU data reduction is the wavelength calibration of the Copper-Argon arcs. The arc spectrum are recorded during the night of the science observations. They are obtained by shining a lamp onto the IFU with the same filter and gratings as the science data. The spectrum shows emission lines at known wavelengths and this serves as a wavelength scale for the science spectra. Step 4 in figure 4.6 shows the Gemini IRAF task required for wavelength calibration. This task also cuts the raw data at the slits and corrects for the CCD chip gaps.

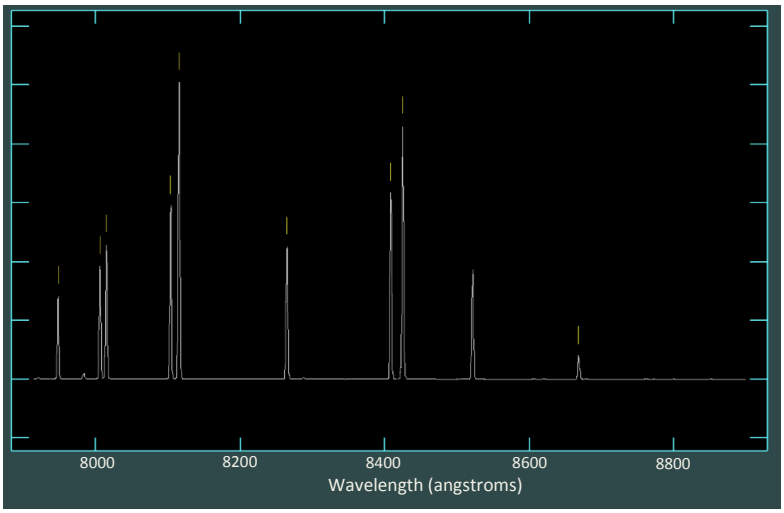

Figure 4.9: Copper-Argon arc spectrum

Figure 4.9 shows the Cu-Ar arc spectrum used for wavelength calibration. Unfortunately there is one emission line at 8510Åwhich is miss-calibrated in the Cu-Ar lamps, therefore it must be excluded in the calibrations.

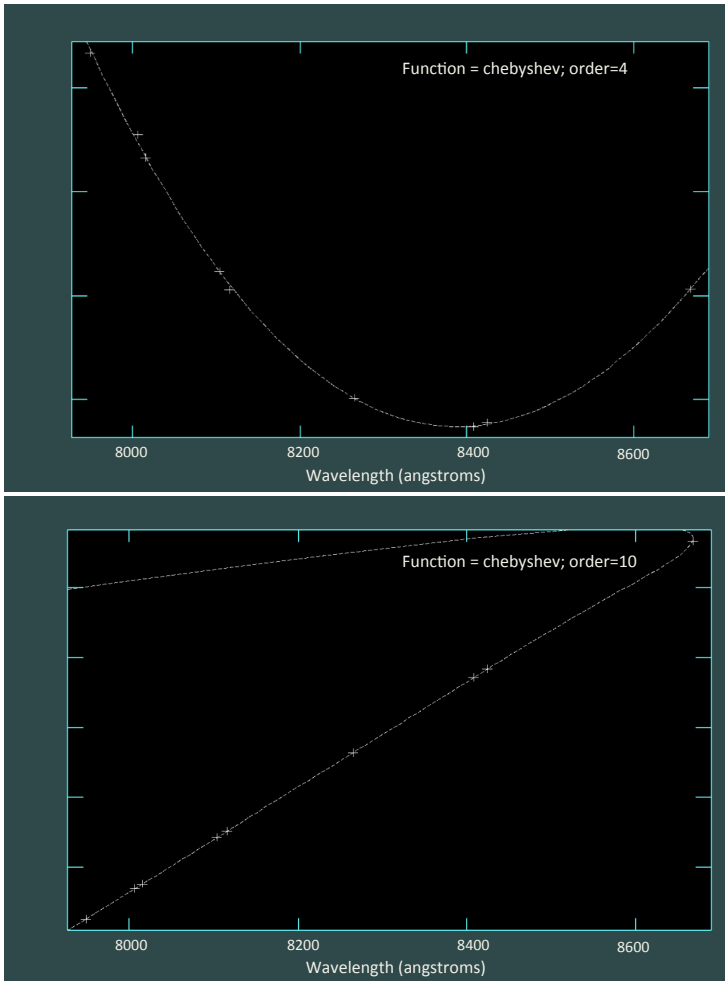

Figure 4.10: Wavelength calibration of the arc spectrum by fitting various functions. Having too many fitting parameters can cause erroneous fits.

Calibration of the Cu-Ar spectra requires fitting of polynomial functions to determine the wavelength solution. Various fitting functions were tried including cubic splines and Chebyshev polynomials. It was ultimately found that a fourth order Chebyshev polynomials provided the most robust wavelength solution. Using higher order fitting functions can cause erroneous fits

as there are not enough calibration arc lines to accurately fit them. Figure 4.10 shows the difference between a good 4th order Chebyshev polynomial and a high 10th order function which did not fit accurately.

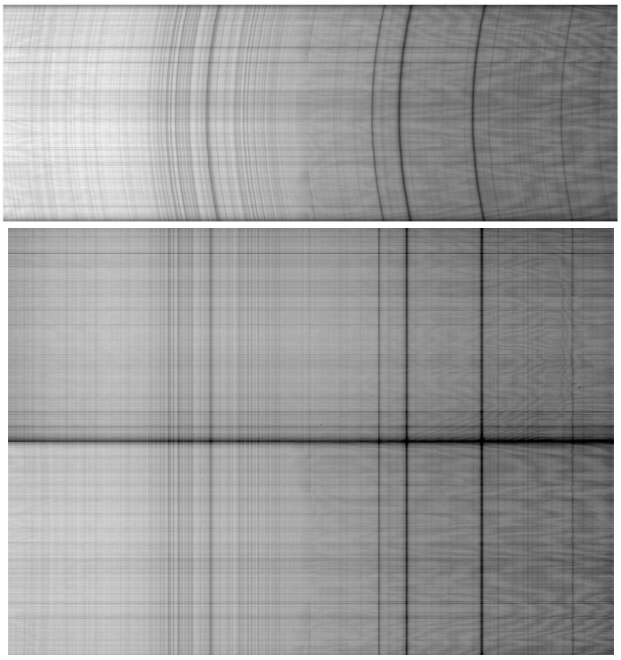

Figure 4.11: The effect of applying the wavelength transform onto the twilight flats. The top figure shows the twilight flat prior to wavelength calibration. The bottom figure is the final calibrated flat. The Calcium Triplet lines are easily observed here as the three bright vertical lines in the image. Wavelength increases from left to right. The vertical axis represents the spectra from individual IFU fibers. The horizontal split in the bottom figure is due to the two slits used in the IFU.

Steps 5 and 6 of the data reduction requires applying the wavelength calibration found in step 4 to the twilight flat and the Cu-Ar arc spectra. This step produces arcs and twilights which are fully wavelength calibrated. These are the same ones that will be used in the IFU science data analysis. Figure 4.11 shows the effect of step 6 from figure 4.6.

Reduction of Science Data

We obtained six hours of telescope time on six different IFU fields, all within the core of M71. To reduce science data, a final flat field must be generated. In addition, the wavelength calibration for each IFU aperture must be completed. Similar to all other IFU calibration data, science data has to be clipped and trimmed so that the chip gaps and the discontinuity between the two slits and be accounted for. Following this, the data is flat fielded using the twilight and GCAL flats from step 3 of figure 4.6. Here we decided to not perform sky subtraction as the sky field of the IFU is still located well within the cluster. Additionally, there are very few night sky telluric lines in the region of the Calcium Triplet lines. Therefore, sky subtraction is not crucial. The stars we found in the sky field were all fainter than V = 20, due to the very low signal to noise ratio in their spectra we did not include them in our analysis.

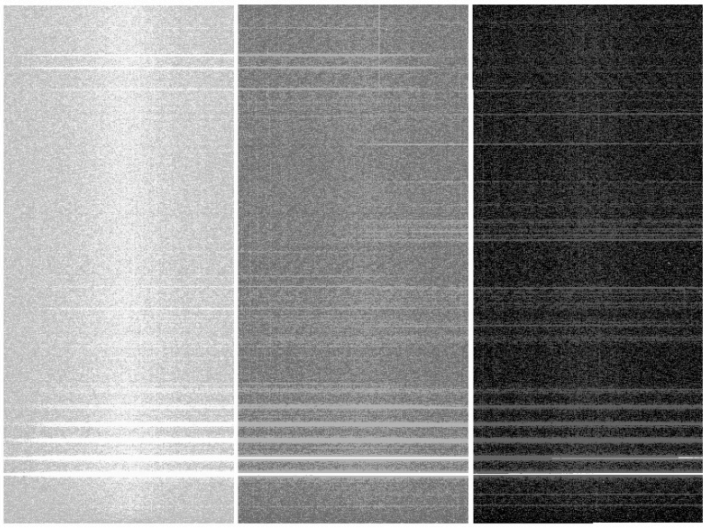

Figure 4.12: Raw science image. Stellar spectra are the bright bands that run from left to right.

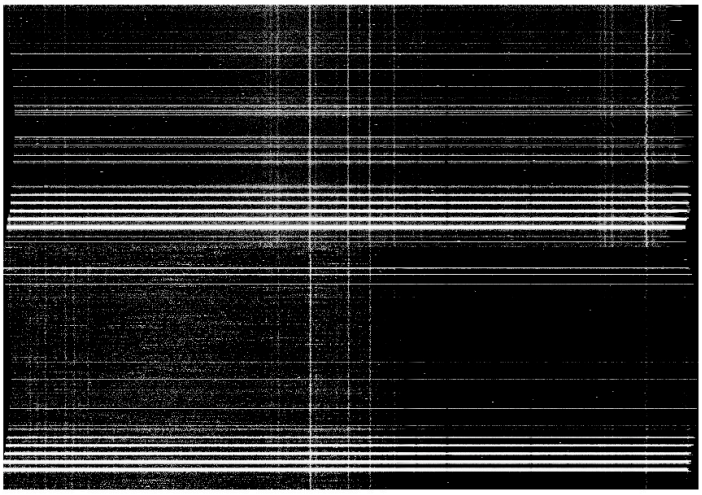

Figure 4.13: Science image after all data reduction. Wavelength increases from left to right. Each of the 1500 IFU fibers are shown here increasing from bottom upwards.

Following this, we preformed cosmic ray rejection and wavelength calibration to the raw science data which resulted in the final science data. Figure 4.13 shows the effects of reduction of IFU science data. All science data were calibrated using GCAL flats and arc spectra from the same night as the science observations. Additionally, the data were processed separately depending on which central wavelength was used for the data. Following data reduction, using the IRAF task GFDISPLAY, the science data can be used to create an IFU image of the field. This task was used for each of the six IFU fields and then manually aligned to create an IFU map of the cluster.

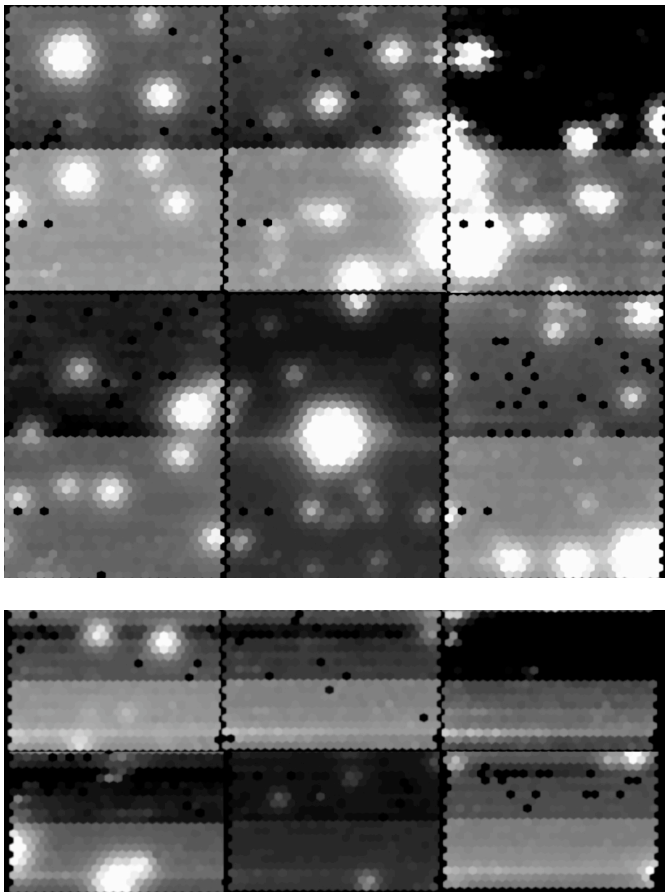

Figure 4.14: Top: Map of the six IFU fields stitched together. There is no overlap between the fields. Each of the six fields appears to be split in half. This is due to the scaling of the image and the differences in throughput of the two IFU slits. Bottom: IFU map of the sky field located 1 arcminute away from the larger field.

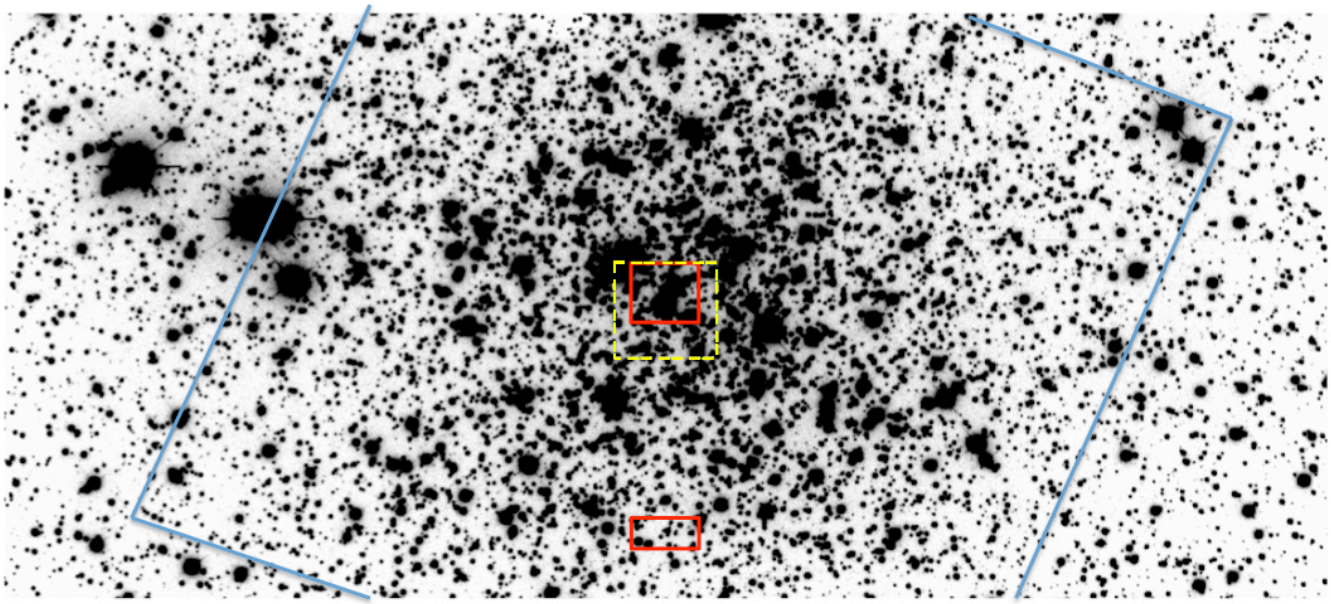

Figure 4.15: Image of the cluster obtained by one of the three GMOS CCDs used for target acquisition. Red represents the two IFU fields, yellow represents the NIRI field also found in figure 2.4. The blue is the field of the ACS from figure 2.2.

4.5 Radial Velocities

To obtain radial velocities of stellar spectra one needs to calculate the difference between wavelength of a given spectral feature to that a similar feature whose velocity is known. One technique for determining the radial velocity of a given spectrum is to cross correlate it against a template spectrum. Cross correlation is a technique used to measure lag between two signals. As the signals are correlated a correlation plot is produced. If two signals are identical, the correlation plot will have a maximum at zero. However, if there is a small shift in one of the signals the plot's maximum will be offset. Figure 4.16 shows the basic idea behind cross correlation of two signals.

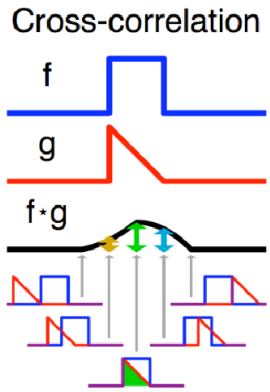

Figure 4.16: Cross correlation of two signals. Where the signals overlap there is a maximum in the correlation function. If these were two spectra, the radial velocity would be the offset of the peak of the correlation function. This is analogous to a sliding dot product of two signals.

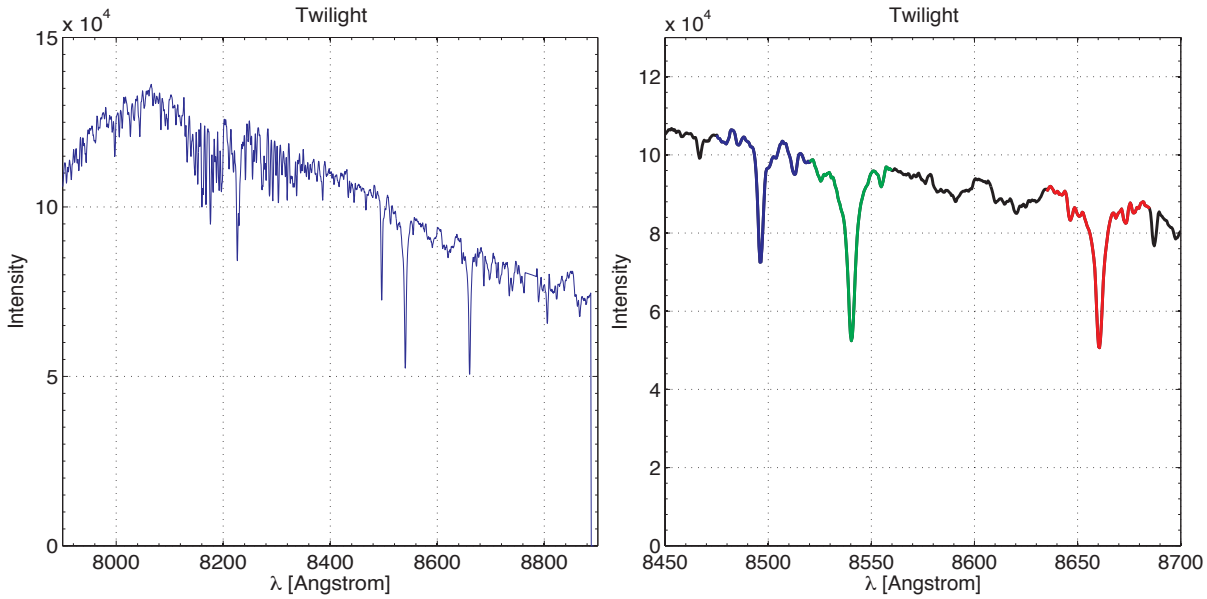

Figure 4.17: Twilight Spectra. The figure on the right shows a close up of the three regions of cross correlation when the lines are used individually.

As we have strong Calcium Triplet lines in the twilight signals (see figure

4.17). We will use them as one of the correlation signals. The other will be the stellar spectra. From figure 4.14 we can see small hexagonal lenslets. Each of these contains a stellar spectrum. Therefore, the brighter stars will have not only stronger absorption lines in the spectrum but more spectra for measuring radial velocities. For cross correlation, we use the three triplet lines individually for stars that are brighter than ∼18.5. This provides three radial velocity measurements for these stars. Stars fainter than ∼18.5 have weak triplet lines in their spectra and therefore are correlated using all three lines at once. Figure 4.17 shows the three triplet line regions for correlation. They were from λ = 8475:8525, 8525:8560, and 8635:8685.

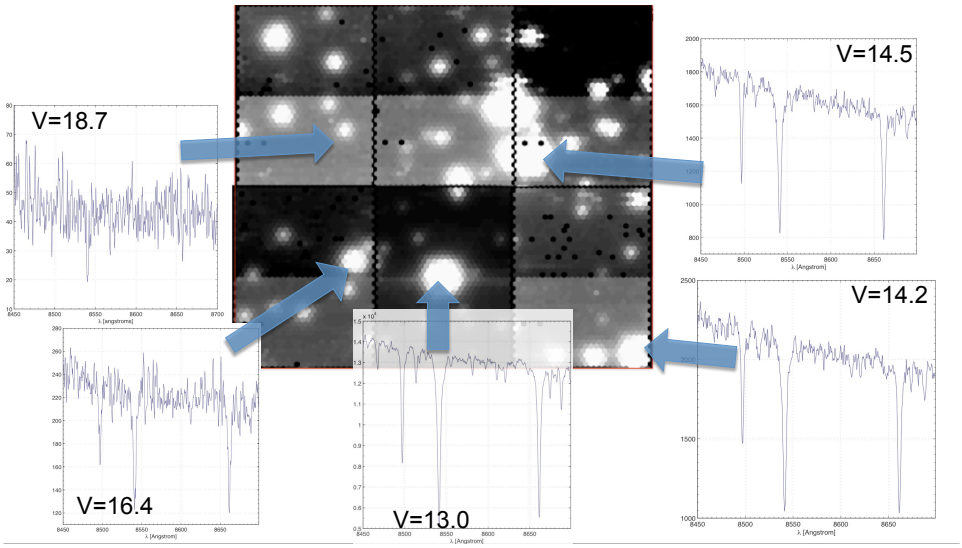

Figure 4.18: The spectra of one IFU fiber and the corresponding star from which the fiber was from. Brighter stars have many more illuminated fibers.

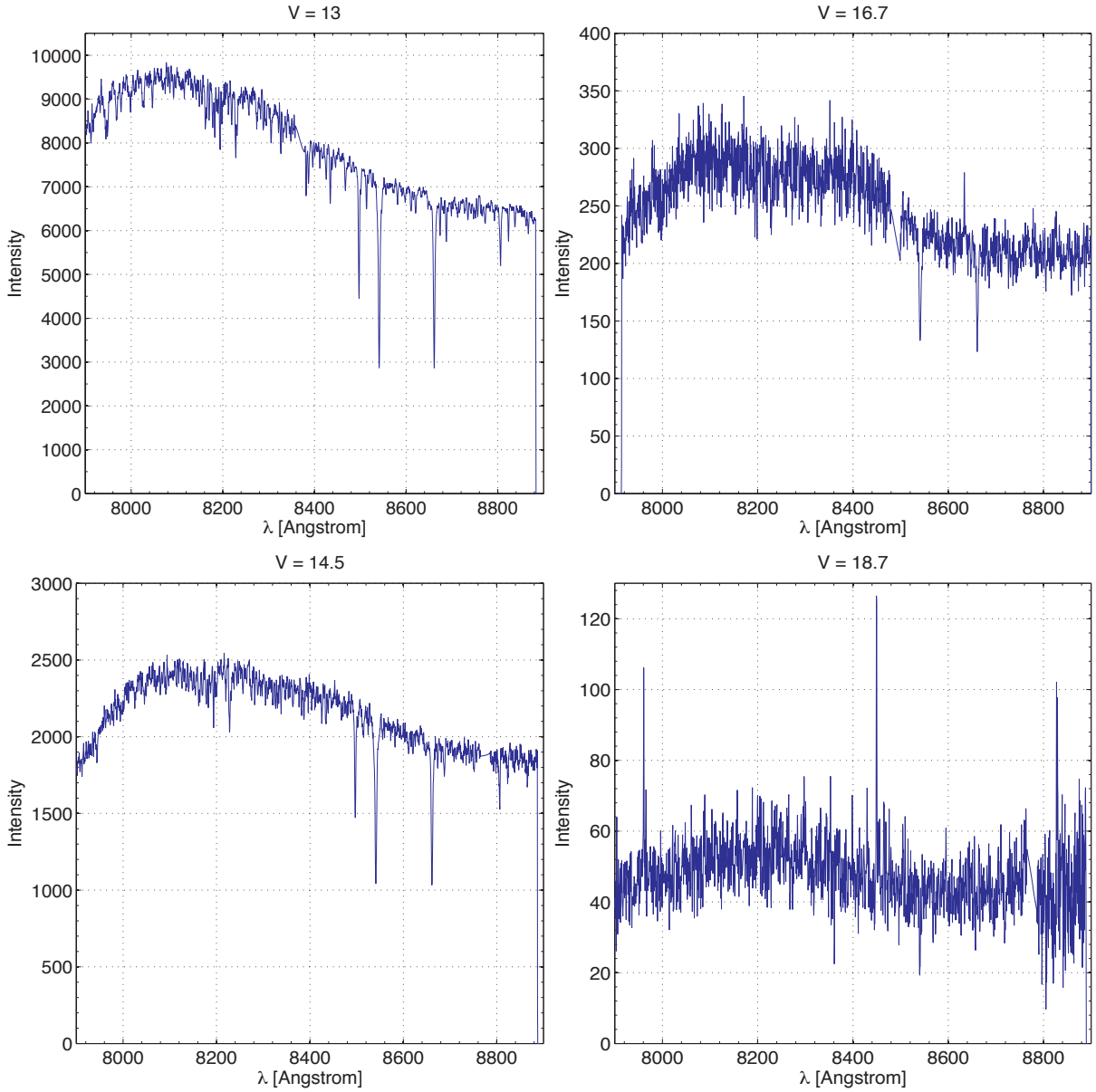

Figure 4.19: Spectra of a single IFU fiber for four different stars. Stars fainter than V = 20 did not have strong enough Calcium Triplet lines for velocity measurements.

The number of radial velocity measurements of a particular star depends

on the star's brightness. The brighter the star is, the more IFU lenslets are illuminated by that star's light, therefore we have more measurements of velocity. Some of the brighter stars can have starlight enter up to 50 lenslets, each of which offers three measurements of radial velocity. Whereas, stars fainter than V = 18 have starlight enter only one lenslet and have weak triplet lines.

The general steps for measurement of velocity is as follows: cross correlate with twilight spectrum, perform heliocentric velocity correction, add in the wavelength shifts due to telescope flexure and finally combine all radial velocities from all measurements for each individual star.

To measure radial velocity, we use the IRAF task FXCOR. This task takes in two spectra and performs a cross correlation over a specified region. In our case, this is the Calcium Triplet region. Following this, FXCOR produces a correlation plot which is used to determine the shift between the two signals. To get the pixel shift between the spectra, we fit a gaussian function to the correlation plot. The location of its peak gives the pixel shift and the error in the shift. We then simply convert from pixels to a wavelength shift using the scale calculated during the wavelength calibration. In our case, this was about 16.6 km/s/pixel but varied from each fiber. FXCOR is applied to all stars and every fiber for which there is stellar spectra present.

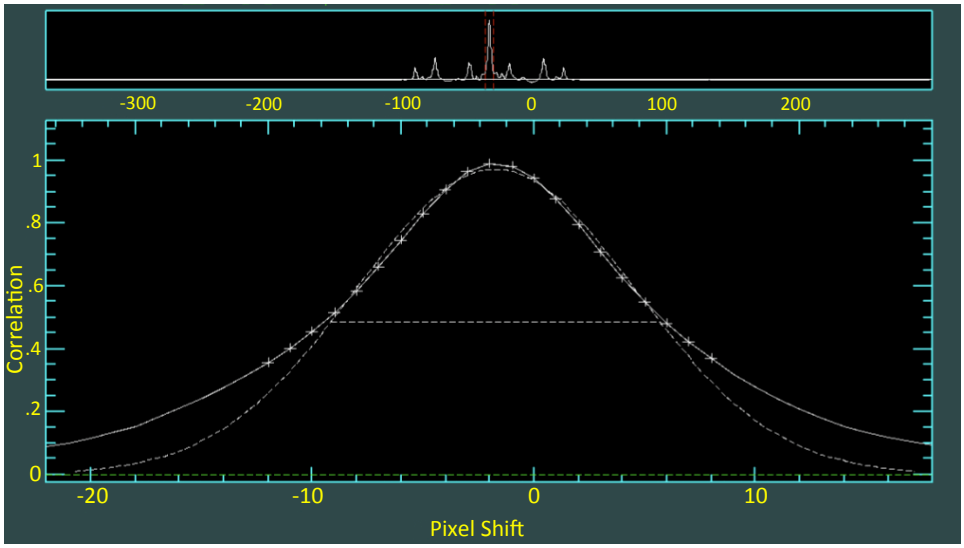

Figure 4.20: The correlation function of two spectra. The fitting function here is a gaussian represented by the dashed curve.

As the Earth orbits the sun, its velocity with respect to M71 is constantly

changing . In addition to this, our data was obtained from different nights. We therefore have to make corrections for this motion. This is done by using the IRAF task RVCORRECT. In this task, we feed in the observed velocity from FXCOR, in addition to the date, time and location of the observations, to obtain the heliocentric radial velocity of the stars.

Flexure Correction

The next task for our velocity calculations is to add in the shift due to CCD flexure to the velocities. When observations are carried out depending on the angle at which the telescope is situated, the CCD can experience small distortions. We correct for these using the Copper-Argon arc spectra. We first create a median combined arc spectrum. We create two different median combined arcs one for each of the IFU slits. We then use FXCOR and cross correlate a small section of the arc spectrum using the median arc as a template and each of the IFU fibers as the object. The result of the flexure response can be seen in figure 4.21. Here, all seven (including doublets) are correlated against the same region of the template.

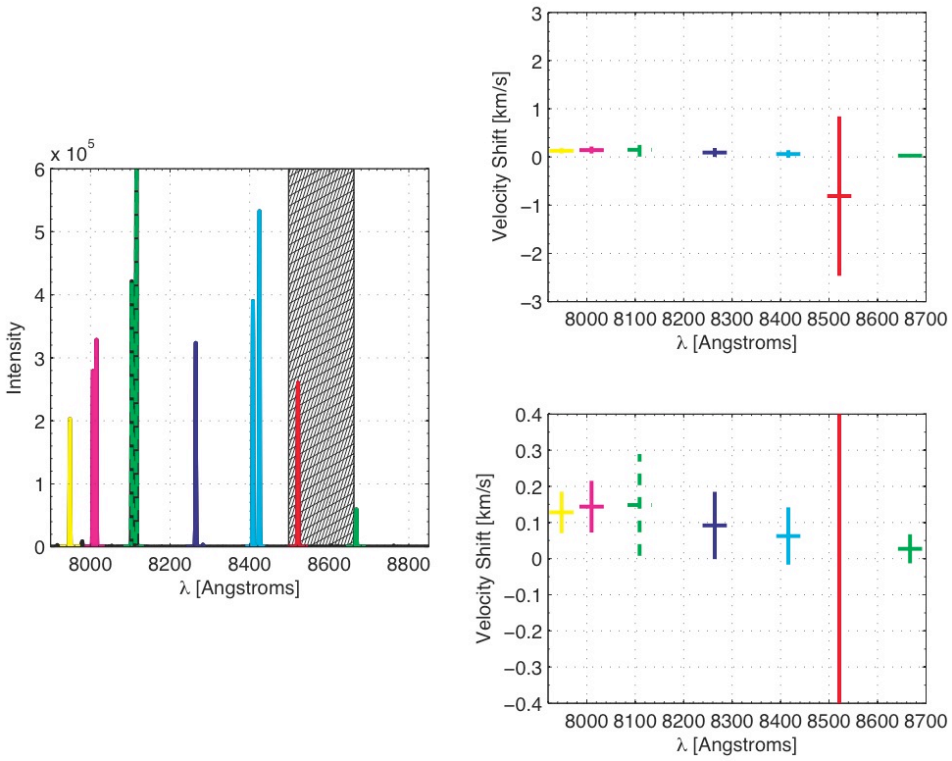

Figure 4.21: The response from CCD flexure. The left panel shows the arc spectrum with individual emission lines coloured. In the two figures on the right hand side, we see the result of cross correlating the coloured region against a median combined arc of that same region. The bottom panel is a zoom of the top panel to show how CCD flexure varies across the chip.

We can see that the red line at $\lambda = 8500$ gives a very large shift. However, this line was ignored in our wavelength calibration due to Gemini IRAF tasks warnings. We then take the next closest line which is the green line at $\lambda \sim$ 8700 Angstroms and use this to correct for CCD flexure. The value from cross correlating the emission line at $\lambda \sim 8700$ against a median combined arc gives the flexure correction, typically this is on the order of $\sim$50 m/s.

Combining Radial Velocities

To combine multiple radial velocity measurements of stars, we used equation 4.3. The underlying principle here is that the more accurate a measurement

is the greater its weight should be on the combined radial velocity.Less accurate measurements have less contribution. We can derive this by using the χ^2 formula:

$$\chi^2 = \sum (\frac{v_i - \bar{v}}{\sigma_i^2})^2 \tag{4.2}$$

Here, v_i and σ_i are the measurements of velocity and the associated error. We then take the derivative of this function with respect to χ^2 and solve for when $\bar{v}$ is set to zero to obtain:

$$\bar{v} = \sum \frac{v_i}{\sigma_i^2} / \sum \frac{1}{\sigma_i^2} \tag{4.3}$$

The error of the measurment is obtained by taking the second derivative of χ^2 and solving for σ:

$$\bar{\sigma} = (\sum \frac{1}{\sigma_i^2})^{-0.5} \tag{4.4}$$

Once we have calculated the combined radial velocities for each of our stars using the above equations, we are now able to proceed to determine the radial velocity dispersion.

4.6 Radial Velocity Dispersion

We have now at this point determined radial velocities for 43 stars in our IFU field. They range from V = 13 to ∼20. We have proper motions for 37 of these stars. We then perform the same colour and proper motion cuts from section 3.1 to arrive at a final cluster member only radial velocity sample.

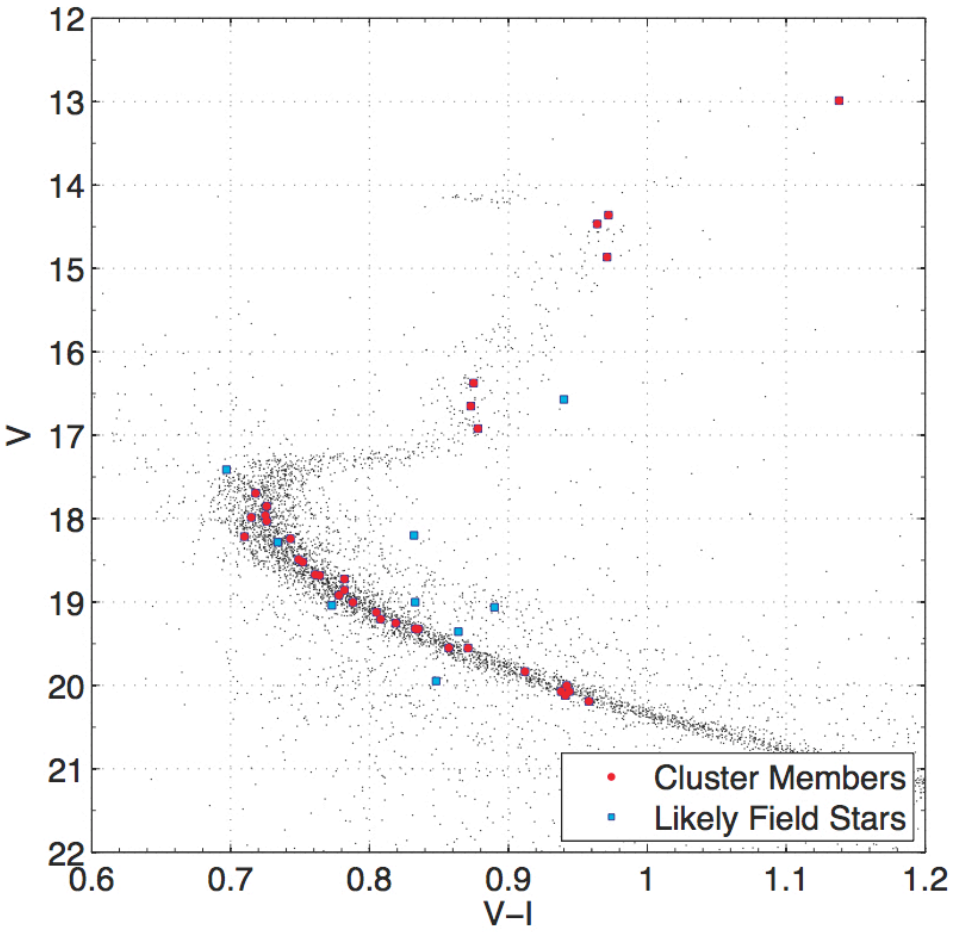

Figure 4.22: The CMD of the IFU stars for which we have radial velocities is overlaid on the CMD of the ACS field. The cluster members are the stars which satisfy the colour criteria from figure 3.4 and the proper motion cut from figure 3.5.

The final radial velocity sample is shown in figure 4.23. We have 36 stars which we can say are likely cluster members and we can now compute the radial velocity dispersion using equation 3.2. We find the radial velocity dispersion to be $\sigma_{vr} = 3.54 \pm 0.64$ km s^{-1}. The error is determined by bootstrapping the sample. In comparison, this value is greater than the previous two measurements of the radial velocity dispersion. Rastorguev & Samus [17] calculate a dispersion of 2.0 $\pm$0.6 km/s, whereas Peterson & Latham

[16] obtained 2.8 ± 0.6 km/s. However, both of these measurements are for stars situated far away from the cluster centre where the dispersion is expected to be lower. Our measurement of the dispersion is slightly higher than Peterson & Latham's, however it is still within the errors.

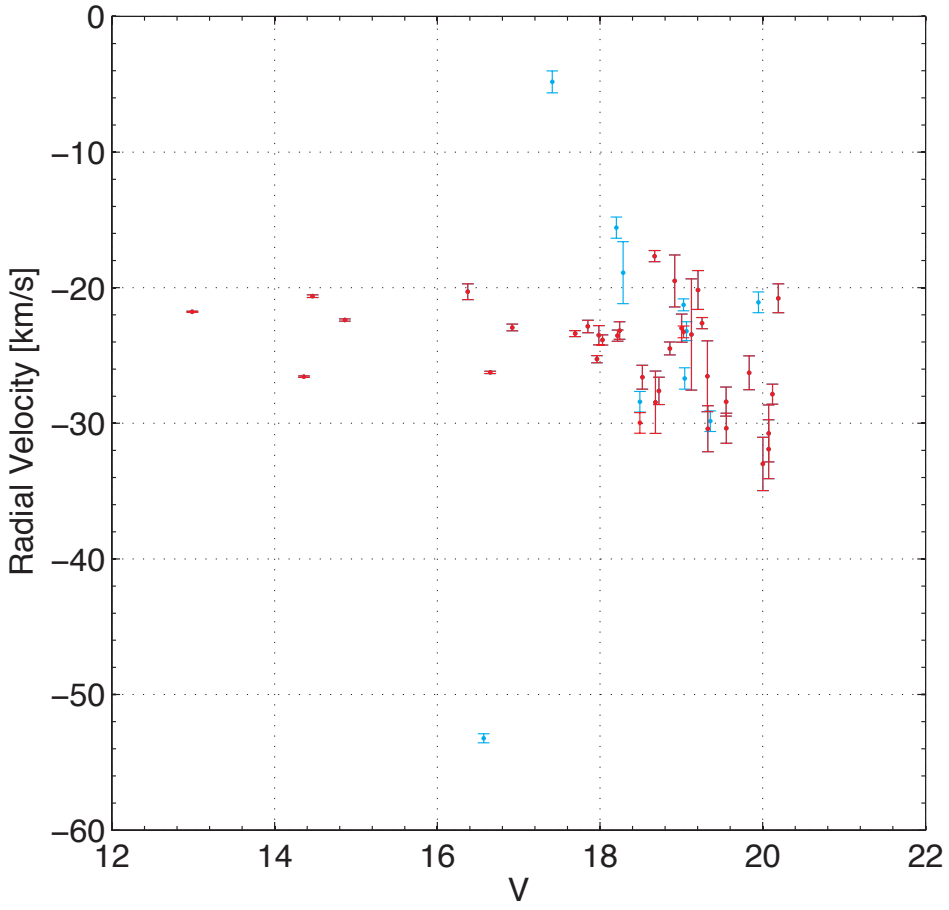

Figure 4.23: Radial velocities of the same stars from figure 4.22.

Chapter 5

The Distance to Messier 71

5.1 Geometric Distance

Distances to globular cluster can be measured using two main methods, fitting stellar evolution models and geometry. Clusters are generally too far away for the use of geometric parallax for modern day instruments. Instead, we can get the distance using the proper motion and radial velocity dispersions. To get the distance, we assume that stars are on isotropically distributed orbits and the absolute tangential and radial velocity dispersions are equal. Binney & Tremaine (1987, p. 280) [5] give the geometric distance as:

$$D(kpc) = \frac{\sigma_{vr}[\text{km s}^{-1}]}{4.74 \times \sigma_{\mu}[\mu\text{as year}^{-1}]} \tag{5.1}$$

We then select the same stars from figure 4.22, which are cluster members and have radial velocities to determine that sample's proper motion dispersion. This is the denominator in equation 5.1. The same group of stars has a proper motion dispersion of 183 $\pm$ 33 μas year^{-1}. By substituting in the radial velocity dispersion, we arrive at a geometric distance to M71 be 4.1 $\pm$ 1.2 kpc. This distance is consistent with all other values of the distance published to date.

5.2 Stellar Model Distance

We now calculate the distance to M71 using stellar evolution models from Dotter et al (2007) [8]. Using published values of metallicity and age, we generated isochrones of M71. However, fitting isochrones on a CMD can be challenging as it is difficult to fit at the main sequence turnoff. Additionally, the turn off is the most important location of the CMD to be fitted as it is most dependent upon the model parameters. Here, we devise a method to fit the turnoff by taking the derivative of the CMD with respect to colour.

Our first step is to make a fiducial CMD from our data. We do this by first removing stars which are clearly off the main sequence in figure 3.2. We then run a bin down the main sequence for every 50 stars and calculate the median V magnitude and colour. This produces a fiducial main sequence down the centre of the CMD as shown in figure 5.1.

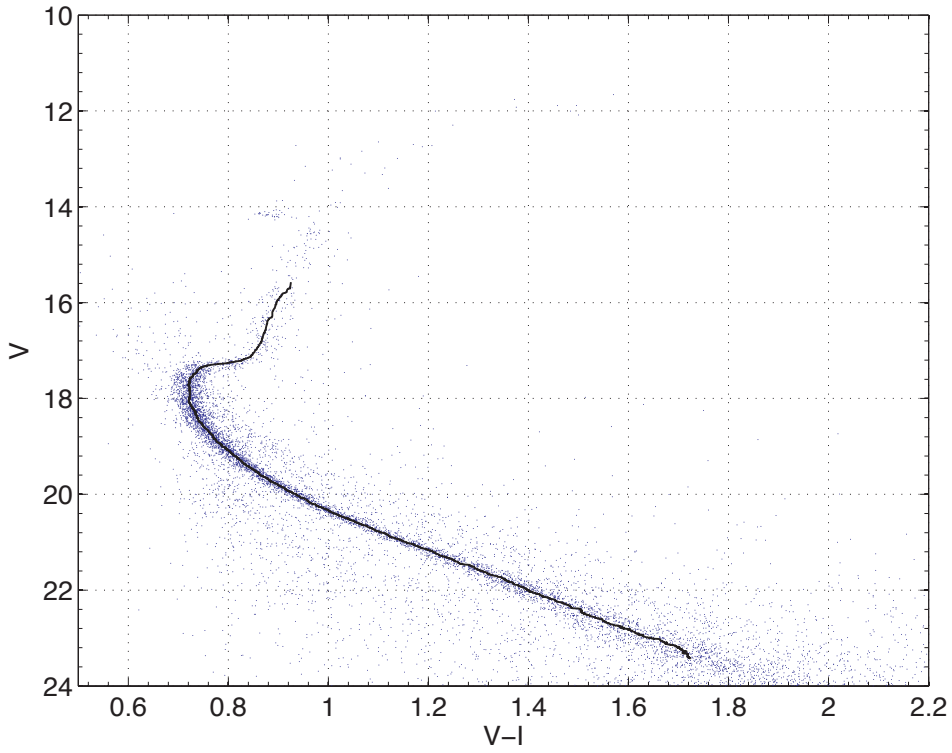

Figure 5.1: The CMD from figure 3.2 with a median line running down the centre. Here V is now in Vega magnitudes.

We now plot the CMD horizontally and the derivative of the CMD as well.

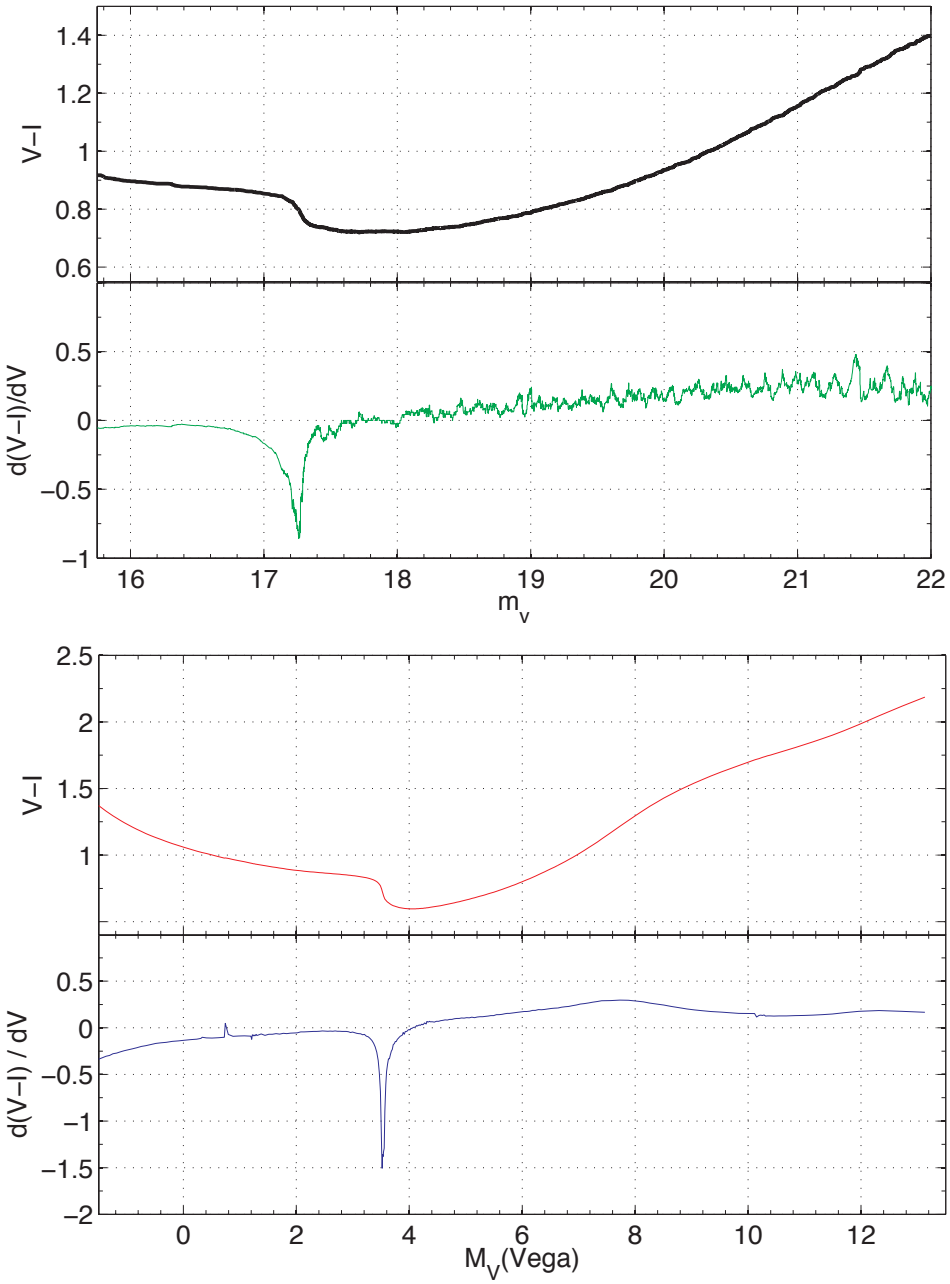

Figure 5.2: Top: The fiducial cmd and the derivative of the cmd. Bottom: An 11 Gyr isochrone of stars with similar abundances as M71 and the corresponding derivative.

The only difference we have here is that the model is calibrated in absolute magnitude and the data is in apparent magnitude. By simply shifting the models so that the spike in the derivative is aligned with the observed data we get the distance modulus. We find the distance modulus to be 13.72 ± 0.10, corresponding to a distance of 3.9 ± 0.2 kpc. The error in the distance modulus comes from the FWHM of the spike in the derivative plot.

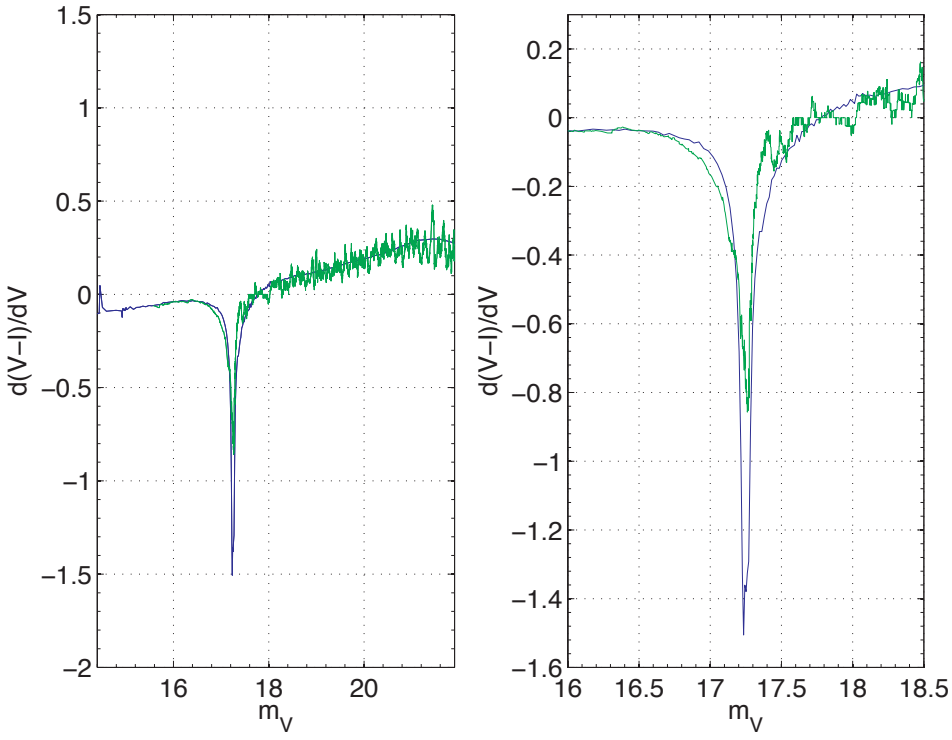

Figure 5.3: By shifting the isochrone so that the spike of the derivative matches that of the observed data, we get the distance modulus. The left panel is over the entire CMD. The right panel is a close up of the turn off.

We have now calculated the distance to M71 using two independent methods. Previous measurements of the distance have been by Arp & Hartwick (1971) [3] of 4100 ± 400 pc and Geffert & Maintz (2000) [10] at 3600 ± 250 pc. Both of our measurements place M71 at distances which are consistent with previous results.

Chapter 6

Conclusions

Using the Gemini North Observatory and two of its instruments, Near Infrared Adaptive Optics Imager (NIRI) and the Gemini Mulit Object Spectrograph's Integrated Field Unit (GMOS-IFU), we determined the proper motions and radial velocities of stars in the core of Messier 71. The NIRI data was obtained over a 3.8 year span and allowed us to explore the internal dynamics in the core of the cluster. In this short time span we were able to resolve the internal proper motion dispersion, a feat normally reserved for space based observatories. Previous work on M71's proper motions from ground based telescopes required images obtained decades apart. Adaptive optics imaging in conjunction with ALLFRAME software was required to accomplish this task, therefore this thesis is a testament for the capabilities of instrumentation and computer software.

From the proper motion data, we found no evidence for a central intermediate mass black hole and were able to put a strict upper limit of just $150M_{\odot}$. Additionally, we found no evidence of anisotropy in the motions of stars and inconclusive evidence for any escaping stars.

With the use of the GMOS-IFU, we were able to determine the radial velocities of 43 stars from our NIRI field. This is the first time that stars have had their radial velocities and proper motions measured in the core of a globular cluster. We were thus able to determine the radial velocity dispersion in the core of the cluster. By combining the radial velocity and proper motion dispersions, we are able to calculate the geometric distance to the cluster. By using the same stars for both proper motion and radial velocity measurments, we are able to simply the distance calculation and not have to incorporate uncertainties in the orbital parameters of stars. Using this method, we find the distance to be 4.1 ± 1.2 kpc.

Finally we determined the distance to M71 using stellar evolution models. Normally, this task is somewhat ambiguous to perform as fitting an isochrone to a CMD is difficult to perform. We devised a new method to fit isochrones to data by taking the derivative of the CMD with respect to colour. In our observed filters, the CMD is simplified as it turns into a spike at the main sequence turn off. This spike can be used to easily fit our

observed data. Using this method, our distance to the cluster was found to be 3.9±0.2 kpc, consistent with the geometric distance.

Some of the techniques discussed in this thesis are performed for the first time and have yet to be found in published literature. In particular, resolving proper motion dispersions using ground based telescopes in a very short timescale. Also we were the first to use the same stars for the proper motion and radial velocity dispersions for the geometric distance. Finally, using derivatives of the CMD to calculate a distance using stellar models.

Bibliography

[1] J. Anderson, A. Sarajedini, L. R. Bedin, I. R. King, G. Piotto, I. N. Reid, M. Siegel, S. R. Majewski, N. E. Q. Paust, A. Aparicio, A. P. Milone, B. Chaboyer, and A. Rosenberg. The Acs Survey of Globular Clusters. V. Generating a Comprehensive Star Catalog for each Cluster. *AJ*, 135:2055–2073, June 2008.

[2] J. Anderson and R. P. van der Marel. New Limits on an Intermediate-Mass Black Hole in Omega Centauri. I. Hubble Space Telescope Photometry and Proper Motions. *ApJ*, 710:1032–1062, February 2010.

[3] H. C. Arp and F. D. A. Hartwick. A Photometric Study of the Metal-Rich Globular Cluster M71. *Ap.J.*, 167:499–+, August 1971.

[4] H. Baumgardt, J. Makino, and T. Ebisuzaki. Massive Black Holes in Star Clusters. II. Realistic Cluster Models. *ApJ*, 613:1143–1156, October 2004.

[5] J. Binney and S. Tremaine. *Galactic dynamics*. 1987.

[6] K. M. Cudworth. Photometry, proper motions, and membership in the globular cluster M71. *A.J.*, 90:65–73, 1985.

[7] J. Cuffey. Noc 6838. *A.J.*, 64:327–+, 1959.

[8] A. Dotter, B. Chaboyer, J. W. Ferguson, H.-c. Lee, G. Worthey, D. Jevremović, and E. Baron. Stellar Population Models and Individual Element Abundances. I. Sensitivity of Stellar Evolution Models. *Ap.J.*, 666:403–412, September 2007.

[9] K. Gebhardt, R. M. Rich, and L. C. Ho. An Intermediate-Mass Black Hole in the Globular Cluster G1: Improved Significance from New Keck and Hubble Space Telescope Observations. *ApJ*, 634:1093–1102, December 2005.

[10] M. Geffert and G. Maintz. First results of a photometric and astrometric study of the globular cluster M 71 (NGC 6838). *Astron. Astrophys. Suppl. Ser.*, 144:227–233, June 2000.

[11] A. M. Ghez, M. Morris, and E. E. Becklin. Dynamical Evidence for a Supermassive Black Hole at the Center of the Milky Way. In D. R. Merritt, M. Valluri, and J. A. Sellwood, editors, *Galaxy Dynamics - A Rutgers Symposium*, volume 182 of *Astronomical Society of the Pacific Conference Series*, page 24, August 1999.

[12] R. Goldsbury, H. B. Richer, J. Anderson, A. Dotter, A. Sarajedini, and K. Woodley. The ACS Survey of Galactic Globular Clusters. X. New Determinations of Centers for 65 Clusters. *AJ*, 140:1830–1837, December 2010.

[13] W. E. Harris. A Catalog of Parameters for Globular Clusters in the Milky Way. *A.J.*, 112:1487–+, October 1996.

[14] N. Lützgendorf, M. Kissler-Patig, E. Noyola, B. Jalali, P. T. de Zeeuw, K. Gebhardt, and H. Baumgardt. Kinematic signature of an intermediate-mass black hole in the globular cluster NGC 6388. *AAAP*, 533:A36, September 2011.

[15] E. Noyola, K. Gebhardt, and M. Bergmann. Gemini and Hubble Space Telescope Evidence for an Intermediate-Mass Black Hole in ω Centauri. *ApJ*, 676:1008–1015, April 2008.

[16] C. J. Peterson and I. R. King. The structure of star clusters. VI. Observed radii and structural parameters in globular clusters. *A.J.*, 80:427–436, June 1975.

[17] A. S. Rastorguev and N. N. Samus. Velocity Dispersion of Stars and the Mass of Globular Clusters m4 m5 M10 M12 and M71. *Soviet Astronomy Letters*, 17:388, May 1991.

[18] H. B. Richer and G. G. Fahlman. Star counts in the globular cluster M71. *Ap.J.*, 339:178–194, April 1989.

[19] A. C. Robin, C. Reylé, S. Derrière, and S. Picaud. A synthetic view on structure and evolution of the Milky Way. *AAAP*, 409:523–540, October 2003.

[20] P. J. Rousseeuw and N. N. Croux. Alternatives to the Median Absolute Deviation. *Journal of the American Statistical Association*, 88:20, 1991.

[21] M. Safonova and P. Shastri. Extrapolating SMBH correlations down the mass scale: the case for IMBHs in globular clusters. *APPS*, 325:47–58, January 2010.

[22] R. S. Samra, H. B. Richer, J. S. Heyl, R. Goldsbury, K. Thanjavur, G. Walker, and K. A. Woodley. Proper Motions and Internal Dynamics in the Core of the Globular Cluster M71. *ApJl*, 751:L12, May 2012.

[23] A. Sarajedini, L. R. Bedin, B. Chaboyer, A. Dotter, M. Siegel, J. Anderson, A. Aparicio, I. King, S. Majewski, A. Marín-Franch, G. Piotto, I. N. Reid, and A. Rosenberg. The ACS Survey of Galactic Globular Clusters. I. Overview and Clusters without Previous Hubble Space Telescope Photometry. *aj*, 133:1658–1672, April 2007.

[24] G. V. Schultz and W. Wiemer. Interstellar reddening and IR-excess of O and B stars. *AAP*, 43:133–139, September 1975.

[25] L. Spitzer. *Dynamical evolution of globular clusters*. 1987.

[26] P. B. Stetson. DAOPHOT - A computer program for crowded-field stellar photometry. *Pub.Astron.Soc.Pac.*, 99:191–222, March 1987.

[27] P. B. Stetson. More Experiments with DAOPHOT II and WF/PC Images. In D. M. Worrall, C. Biemesderfer, and J. Barnes, editors, *Astronomical Data Analysis Software and Systems I*, volume 25 of *Astronomical Society of the Pacific Conference Series*, page 297, 1992.

[28] S. E. Strom, K. M. Strom, D. C. Wells, J. C. Forte, M. G. Smith, and W. E. Harris. The halo globular clusters of the giant elliptical galaxy Messier 87. *ApJ*, 245:416–453, April 1981.

[29] J. S. Ulvestad, J. E. Greene, and L. C. Ho. Radio Emission from the Intermediate-Mass Black Hole in the Globular Cluster G1. *ApJL*, 661:L151–L154, June 2007.

[30] A. A. Wyller. Observational Aspects of Black Holes in Globular Clusters. *ApJ*, 160:443, May 1970.

[31] R. Zinn. The globular cluster system of the galaxy. IV - The halo and disk subsystems. *Ap.J.*, 293:424–444, June 1985.

Appendix A

NIRI Proper Motion Data

The cluster centre is located at coordinates (x,y) = (754,806). The each pixel is 0.022″projected onto the plane of the sky. Proper motions and proper motion errors are in milli-arcseconds year^{-1}.

Star ID	x	y	PM$_x$	δx	PM$_y$	δy	V	I
3	122.81	-41.08	-0.4919	0.4527	-0.1050	0.3173	17.215	16.410
4	561.78	-38.06	0.0606	0.1552	0.5228	0.2791	18.931	18.150
6	458.76	-35.75	-0.2638	0.2264	0.5746	0.2717	19.658	18.791
7	81.10	-35.01	-0.1944	0.3582	-0.3903	0.3132	20.086	19.129
8	415.44	-33.10	-0.0847	0.2421	0.1910	0.2182	20.956	19.736
9	138.32	-25.12	-0.3584	0.3569	-0.0114	0.2446	17.165	16.345
11	107.26	-17.85	-0.1851	0.2430	0.1682	0.2115	18.735	17.986
12	197.89	-17.84	-0.3468	0.3062	0.3442	0.2445	17.853	17.103
13	385.18	-16.52	-0.2374	0.2156	0.1425	0.1446	19.639	18.588
14	920.14	-17.31	0.1485	0.3967	-2.8143	1.0246	22.640	21.177
15	26.55	-15.89	-0.4826	0.3689	0.0962	0.2441	21.352	20.155
16	78.20	-7.89	-0.0270	0.2792	0.1635	0.2142	19.796	18.871
17	499.25	-6.46	0.0581	0.1063	0.2480	0.1847	18.359	17.619
18	693.83	-4.89	-0.2255	0.1806	0.8493	0.3728	22.544	21.021
20	215.69	2.31	-0.0479	0.1776	-3.6546	1.1523	17.630	16.831
22	385.76	6.56	-0.2633	0.2168	0.3945	0.2078	19.938	18.999
24	902.75	12.97	-0.0228	0.1502	0.4657	0.2231	17.858	17.147
25	752.69	15.88	-0.2009	0.1476	0.3188	0.2331	20.419	19.398
27	475.29	21.42	0.0303	0.1115	0.4136	0.1807	19.508	18.669
28	878.10	22.11	0.0389	0.1134	0.1672	0.1778	18.317	17.585
29	409.58	24.08	-1.4610	0.5933	-1.6851	0.5741	22.782	21.474
34	689.84	30.50	-2.0788	0.6503	-1.6266	0.4909	22.137	20.949
35	236.29	40.78	-0.3603	0.1989	0.1420	0.1501	20.439	19.393
36	437.86	62.58	0.1431	0.1197	0.2817	0.1337	20.485	19.453
37	422.89	73.40	0.2566	0.1812	0.4196	0.3044	23.026	21.612
38	420.62	77.61	0.0547	0.0975	0.2338	0.1220	20.078	19.135
39	929.06	80.66	0.0635	0.1183	0.1244	0.1300	19.045	18.245

Star ID	x	y	PM_x	δx	PM_y	δy	V	I
40	732.86	88.89	-0.3190	0.1101	-3.5128	1.0146	17.088	16.404
41	945.92	89.93	0.0508	0.1567	0.2830	0.1368	21.365	20.125
42	295.54	95.60	-0.0793	0.1848	-0.0254	0.0864	23.025	21.263
43	806.44	96.32	0.0910	0.1070	0.3885	0.1791	18.747	17.901
44	4.07	109.97	0.4564	0.2400	0.2688	0.1672	16.541	15.939
45	850.02	122.29	0.0982	0.0917	0.2561	0.1344	19.158	18.323
46	514.09	127.58	0.2265	0.0893	0.2180	0.1056	19.074	18.278
47	910.24	136.31	0.0285	0.0804	0.3258	0.1170	21.118	19.930
48	169.70	157.53	-0.4098	0.1841	0.0150	0.0703	19.456	18.589
49	451.06	160.42	0.0163	0.0800	0.5072	0.1932	17.491	16.766
50	494.21	159.51	0.3491	0.1081	0.4634	0.1674	20.429	19.424
51	728.42	163.99	-0.1672	0.0973	0.2587	0.1977	23.054	21.535
52	532.74	165.04	0.5272	0.2347	-0.0998	0.1439	23.906	21.977
53	948.40	166.46	0.3084	0.1252	0.1446	0.0922	20.271	19.295
54	39.30	168.24	-0.0098	0.1682	-0.0340	0.0938	20.703	19.630
55	168.89	173.39	-0.2864	0.1549	-0.0933	0.0863	20.709	19.627
56	213.21	190.34	-0.1565	0.1127	0.1267	0.0724	21.216	20.006
57	862.52	193.65	-0.1970	0.0770	0.1897	0.1018	18.937	18.151
58	809.47	202.88	-0.0371	0.0780	0.0080	0.0895	16.886	16.012
59	652.08	205.16	-0.1978	0.0876	0.3009	0.1592	20.500	19.422
60	840.21	207.43	-0.0124	0.1585	0.0228	0.0746	22.243	20.776
61	430.19	-0.17	-0.4683	0.3659	0.3434	0.2775	23.840	21.977
62	594.79	211.22	0.1361	0.0783	0.3120	0.1668	18.266	17.473
63	379.49	219.08	0.1817	0.0942	0.2719	0.1120	19.530	18.651
64	476.18	221.91	-0.1280	0.1141	0.3167	0.1447	23.058	21.394
65	293.16	227.44	-1.3619	0.4619	-2.1200	0.6294	16.024	15.251
67	705.62	235.08	-0.2641	0.1008	0.5772	0.2192	22.332	20.841
68	995.18	244.74	0.2600	0.1274	-0.2514	0.1454	18.255	17.526
69	577.57	248.00	0.1501	0.0746	0.4670	0.1921	19.583	18.602
70	758.55	250.57	-0.5295	0.1325	0.4764	0.1829	21.393	20.134
71	971.16	249.54	-0.1213	0.1445	-2.9432	0.9393	21.278	20.252
72	246.69	259.50	-0.2123	0.0838	0.1140	0.1350	23.163	21.493
73	591.54	259.52	-1.1606	0.3327	-3.6548	1.0847	22.067	20.639
74	664.60	261.33	-0.0765	0.1223	0.3854	0.2041	23.458	21.559
75	216.89	272.54	-0.1143	0.0725	0.1190	0.0897	18.681	17.888
76	726.20	272.73	-0.2942	0.0937	-1.6538	0.4721	19.374	18.603
77	120.46	275.15	0.1379	0.0905	-0.0757	0.0640	18.744	17.981

Star ID	x	y	PM_x	δx	PM_y	δy	V	I
78	916.21	275.11	-0.0959	0.0616	0.0855	0.0745	18.832	18.060
81	130.97	295.60	0.0067	0.0599	0.0277	0.0784	18.237	17.485
82	293.14	300.14	-0.0080	0.0874	0.0868	0.0699	21.504	20.223
83	823.52	300.14	-0.0277	0.1085	0.3958	0.2641	22.927	21.379
84	525.84	317.79	0.3590	0.1375	0.1156	0.0702	17.883	17.161
85	750.39	318.58	-0.1825	0.0848	0.1892	0.1671	21.157	19.929
86	480.20	319.56	0.1192	0.0712	-0.2301	0.0943	18.983	18.148
87	209.07	321.65	-0.3504	0.1059	-0.0912	0.0992	17.940	17.230
88	733.99	321.56	-0.0438	0.2013	0.3281	0.4832	23.800	22.075
89	395.72	333.61	0.6091	0.2194	0.1089	0.1445	23.568	21.659
93	531.69	346.05	1.8816	0.5876	-3.8401	1.2557	23.873	21.910
98	466.33	350.15	-0.0775	0.0550	0.2711	0.0896	20.072	19.128
99	922.93	350.45	-2.6708	0.8347	0.3838	0.1460	17.392	16.646
104	721.28	358.73	-0.3045	0.0827	0.2820	0.1306	16.921	16.043
106	534.13	359.77	-0.0581	0.0611	0.3494	0.1158	20.095	19.138
108	656.78	361.40	0.1104	0.0678	0.2475	0.1029	17.694	16.976
110	538.36	362.55	-2.7379	0.8079	-0.5075	0.1808	22.975	20.567
111	913.34	364.10	0.0599	0.1227	-0.0135	0.0946	20.459	19.410
114	588.66	90.66	0.3019	0.2040	0.5881	0.3059	23.970	22.167
120	835.99	374.85	2.2162	0.6952	-9.0674	2.9333	18.682	17.711
122	166.66	377.77	-0.1083	0.0617	0.0560	0.0662	18.659	17.895
127	643.58	382.07	0.1863	0.1312	-2.7166	0.8730	21.963	20.486
128	397.75	383.20	-3.1051	0.9293	-0.2260	0.1131	21.335	19.871
131	914.78	386.71	-0.1366	0.0897	-0.1495	0.1004	20.646	19.589
133	485.93	401.28	-0.0140	0.0671	-0.1527	0.1044	20.192	19.234
134	-23.90	403.62	-0.0262	0.3397	0.6111	0.2330	22.866	21.230
135	500.56	407.08	0.1182	0.1220	-0.0150	0.0650	20.119	19.178
136	586.97	411.88	0.1568	0.0742	-0.0578	0.0544	18.725	17.943
137	465.10	415.38	0.3180	0.1542	-0.3660	0.1255	18.030	17.304
138	531.58	414.74	0.0213	0.0695	0.2066	0.0875	19.255	18.436
139	188.86	423.86	-0.2073	0.0813	0.0319	0.0671	18.682	17.918
140	735.25	425.11	-0.0993	0.0682	-0.1558	0.0612	21.030	19.820
141	824.13	427.18	-0.0708	0.0759	0.3349	0.1075	19.216	18.284
142	282.46	432.33	-0.2273	0.0752	0.2195	0.0737	17.986	17.271
143	158.48	432.66	0.2872	0.2022	0.0223	0.1609	23.398	21.714
144	238.60	437.18	-0.0482	0.0644	0.0886	0.0593	18.918	18.140
145	521.47	437.42	-0.1794	0.1042	-0.0233	0.1310	19.063	18.173

Star ID	x	y	PM_x	δx	PM_y	δy	V	I
147	23.08	462.78	-0.0132	0.2362	1.0600	0.4137	24.062	21.979
154	354.75	471.07	-0.0915	0.0818	0.0422	0.0665	18.364	17.556
160	605.42	476.08	-0.0946	0.2507	0.5336	0.2641	24.295	22.201
161	990.76	475.57	0.2522	0.1533	-0.1978	0.1412	20.926	19.795
174	123.23	487.13	3.1927	1.0234	-7.1140	2.1704	22.404	20.788
178	6.41	490.70	-0.1102	0.1929	0.5150	0.2488	17.069	16.453
187	202.32	495.92	-0.2027	0.0798	0.0575	0.0572	19.326	18.491
205	735.54	507.01	0.0609	0.0848	-0.0524	0.0579	20.991	19.839
219	606.00	520.16	-0.1208	0.0993	-0.1172	0.1435	22.895	21.227
220	366.93	520.56	0.1418	0.1229	0.0847	0.0580	16.375	15.500
226	835.25	531.96	-0.1796	0.0804	0.0936	0.0782	19.213	18.409
227	782.91	543.10	-0.2550	0.0845	0.2745	0.1109	19.320	18.487
228	389.76	545.18	0.0337	0.0734	0.2250	0.0760	19.026	18.193
229	899.12	547.18	-0.1011	0.0781	-0.1571	0.1165	20.820	19.697
230	228.10	548.50	-0.2654	0.1022	0.1835	0.1028	22.897	21.268
232	585.53	562.27	0.2509	0.1190	0.0832	0.0590	19.850	18.937
233	447.66	563.86	0.1827	0.1014	0.0041	0.0733	18.858	18.076
234	251.99	565.33	-0.3222	0.0912	-0.0350	0.0817	19.123	18.318
235	837.78	564.76	-0.0044	0.1691	0.5769	0.2361	24.013	21.990
236	944.25	564.89	-0.1273	0.0838	-0.0741	0.0907	19.396	18.578
237	369.45	569.74	-0.3571	0.1119	-0.3636	0.2490	23.236	21.492
238	129.95	577.83	-0.2646	0.1318	0.3097	0.1570	17.974	17.258
239	701.96	616.54	0.0897	0.0664	0.0047	0.0790	19.205	18.397
240	422.05	618.16	0.4818	0.1579	-0.0306	0.0690	20.294	19.308
241	731.79	620.22	0.1045	0.1068	0.0990	0.0746	22.469	20.757
242	145.43	636.28	-0.2488	0.1341	-0.1946	0.1287	19.026	18.235
243	804.16	642.01	-0.0899	0.1166	0.1234	0.1068	22.544	21.070
244	515.13	643.98	0.1786	0.0790	0.1423	0.0861	17.292	16.531
245	701.82	645.31	-0.5318	0.1729	-4.6913	1.5484	20.322	19.228
246	43.44	650.29	-0.4769	0.2318	0.3618	0.2368	19.200	18.326
247	499.96	649.69	0.3548	0.1692	0.4499	0.1511	21.018	19.862
248	511.41	654.84	0.0259	0.1033	0.1140	0.0904	17.962	17.237
249	557.39	658.40	-0.0363	0.0479	0.1571	0.1065	19.553	18.682
250	949.40	659.32	0.1477	0.0796	0.3665	0.1518	21.592	20.244
251	23.18	661.65	-0.2040	0.2462	0.4883	0.2744	17.767	17.053
253	538.66	672.05	0.0088	0.1071	0.2952	0.1114	22.559	21.043
257	427.61	675.70	-0.1459	0.0704	-5.2044	1.6731	20.880	19.944

Star ID	x	y	PM_x	δx	PM_y	δy	V	I
259	138.49	677.83	-0.4922	0.1842	-0.1140	0.1234	17.228	16.425
264	792.84	688.40	2.3551	0.7938	-5.3182	1.7785	22.335	20.865
274	426.98	702.38	0.3123	0.1161	0.0925	0.0766	20.072	19.134
279	675.50	713.30	-0.0993	0.0818	-0.0127	0.0684	18.240	17.497
281	61.31	717.78	-0.7583	0.2820	0.0798	0.1781	17.411	16.671
283	883.21	718.51	-0.0096	0.0757	0.0404	0.0808	18.945	18.155
284	485.12	720.52	0.0765	0.0689	-0.0682	0.0622	18.644	17.830
285	700.74	720.43	0.3488	0.1908	0.1819	0.0936	22.317	20.834
286	462.75	724.38	0.3245	0.1212	0.0485	0.0756	20.089	19.141
287	570.33	724.37	-0.2162	0.2478	-0.0873	0.2356	22.100	20.992
288	179.93	733.26	0.2071	0.1644	-4.5018	1.3806	18.216	17.506
289	353.68	735.05	0.2291	0.1136	-0.1643	0.0812	18.671	17.910
290	745.62	739.26	0.1260	0.0721	0.3035	0.1382	18.726	17.966
291	618.67	741.09	0.2558	0.1598	0.1832	0.0949	19.947	19.099
292	944.18	740.81	0.0272	0.1140	0.2242	0.0841	19.202	18.396
293	148.46	742.46	-0.6697	0.2393	-0.0098	0.1352	18.490	17.743
294	731.44	743.54	0.0503	0.0592	0.2343	0.1101	19.004	18.216
295	133.39	744.37	-0.5917	0.2429	0.1651	0.1456	19.717	18.825
296	141.18	754.87	-0.5326	0.2363	0.0835	0.1723	21.044	19.887
301	661.22	758.99	-1.8647	0.6344	-2.6943	0.8720	21.693	20.715
304	249.22	762.22	-0.1990	0.1228	0.0474	0.1269	17.413	16.716
312	327.08	779.37	-0.0205	0.0972	0.1493	0.1075	19.041	18.268
316	524.35	786.65	0.1392	0.0754	0.3343	0.1175	19.833	18.921
317	448.74	791.48	0.4577	0.1442	0.0749	0.0801	21.849	20.486
318	786.60	795.94	-0.2162	0.1062	0.0376	0.1012	21.395	20.160
319	628.74	806.69	0.3696	0.1581	0.3442	0.1282	21.378	20.140
320	723.64	807.44	-0.1568	0.1069	0.4683	0.1941	17.851	17.125
325	429.96	825.94	0.1397	0.1116	0.2022	0.1425	21.115	19.932
326	755.21	827.00	-0.0912	0.1310	0.2343	0.1113	20.603	19.578
327	-2.82	832.37	-0.8890	0.6557	0.1625	0.5844	19.246	18.397
328	1022.80	837.46	0.2760	0.2918	-0.3812	0.1665	18.680	17.932
329	481.67	843.19	0.0643	0.0975	0.2986	0.1782	18.520	17.768
330	568.08	851.17	0.2540	0.1105	0.0140	0.1080	20.002	19.060
331	337.11	853.03	-0.0200	0.1316	-0.0314	0.1188	18.201	17.369
333	956.25	852.81	0.4950	0.1968	0.2784	0.1293	18.132	17.415
335	818.79	858.33	-0.4691	0.2061	-1.0644	0.3558	20.822	19.660
336	919.87	857.68	0.3338	0.1446	0.3906	0.1569	18.119	17.391

Star ID	x	y	PM_x	δx	PM_y	δy	V	I
340	176.02	886.84	-0.5069	0.3739	-0.3971	0.4823	23.102	21.397
344	241.16	895.88	-0.0498	0.1740	-0.1472	0.2204	16.650	15.777
345	550.72	898.24	0.1770	0.1336	-0.0832	0.1835	18.490	17.741
347	884.18	899.93	-0.8589	0.3243	-0.3281	0.1587	21.889	20.093
399	650.69	957.33	-1.4900	0.5754	-1.6996	0.4930	23.501	21.530
402	429.19	959.80	0.4445	0.2512	-0.0314	0.2820	18.943	18.157
423	885.21	995.14	0.4538	0.2261	-0.2206	0.3353	17.149	16.314
430	566.38	1007.70	-0.0754	0.3155	-0.2410	0.5348	18.275	17.517
439	754.59	1025.50	0.3556	0.3658	0.4103	0.6816	20.321	19.281
503	764.84	522.73	0.5655	0.5497	-2.3211	0.7915	25.707	23.304
550	-40.85	575.36	-0.3063	0.5066	1.0955	0.7132	23.643	21.791
553	853.57	598.24	-2.8392	1.2462	-0.4051	0.5861	24.318	23.076
624	452.69	700.60	0.3043	0.5696	-3.0225	0.9431	25.838	23.673
650	119.15	718.91	-0.0860	1.2861	-0.3110	1.3140	25.694	23.398
722	391.13	781.89	0.3781	0.9295	-2.4170	1.1792	25.382	24.392
746	906.81	803.41	-1.6742	1.0401	0.4764	0.8558	25.129	23.808
758	316.79	809.09	0.0829	0.4301	-0.5005	0.4105	24.644	22.748
911	523.83	89.01	-2.3338	0.8104	-2.6938	0.9521	24.671	22.587
951	18.78	899.28	-0.3942	0.5877	0.0879	0.5661	17.804	17.048
966	383.72	905.30	-1.5265	0.8690	-1.1738	0.5789	27.043	23.554
967	429.12	905.44	0.7612	0.4723	-0.3359	0.5117	25.691	23.184
1015	312.20	921.35	-0.3175	0.5613	-0.1506	0.4786	24.373	22.555
1043	787.12	931.87	0.0397	0.3153	-5.9853	1.9341	25.768	23.126
1047	280.67	932.58	-0.6977	0.6668	0.8187	0.6848	24.173	22.522
1056	323.65	936.96	0.0949	0.2867	-0.2146	0.2360	19.549	18.692
1120	639.07	317.26	0.2755	0.3255	0.4769	0.3874	24.612	22.577
1126	987.92	968.20	0.3587	0.5282	-0.1298	0.4256	22.662	21.112
1207	210.49	996.54	-0.6363	0.4633	0.5155	0.5103	18.980	18.179
1258	831.19	-3.87	0.1125	0.5996	0.4963	0.4356	24.230	22.337
2101	864.92	57.89	-0.0104	0.3799	0.4559	0.2028	24.213	22.193
2122	901.86	99.63	-2.0659	0.7441	-3.3361	1.2544	26.182	23.791
2130	275.54	115.60	-1.5356	0.5295	-0.8519	0.3021	22.124	21.220
2131	317.81	116.33	-0.4945	0.2644	-0.1418	0.1721	23.923	21.981
2135	825.51	124.11	-0.1705	0.2308	0.6407	0.2741	24.059	22.106
2152	145.96	176.43	-0.1783	0.3112	0.0625	0.2956	24.556	22.655
2168	149.35	211.62	-10.0620	3.1974	1.2438	0.5194	25.610	22.655
2193	439.49	256.67	-3.3410	1.0817	3.0727	0.9902	25.249	23.414

Star ID	x	y	PM_x	δx	PM_y	δy	V	I
2408	158.97	477.49	-2.3141	0.9164	2.7475	0.9996	25.435	23.746

Table A.1: NIRI Proper Motion Data, the photometry is from the Advanced Camera for Surveys

Appendix B

IFU Radial Velocity Data

The cluster centre is located at the ACS coordinates (x,y) = (2882,2986). The each pixel is 0.049″ projected onto the plane of the sky.

ACS Star ID	V	V-I	V_{rad} [km/s]	δV_{rad} [km/s]	ACS X Pixels	ACS Y Pixels	Cluster Member?
5846	18.682	0.764	-28.45	2.3	2654.4	2838.2	yes
5847	19.326	0.835	-30.4	1.7	2660.5	2869.5	yes
5878	18.918	0.778	-19.5	1.92	2676.3	2843.8	yes
5879	17.986	0.715	-23.51	0.71	2695.5	2841.6	yes
5939	18.283	0.734	-18.89	2.28	2742	2818.7	no
6001	20.072	0.944	-31.91	2.17	2775.6	2805.3	yes
6002	20.192	0.958	-20.78	1.06	2784.2	2827.5	yes
6003	18.03	0.726	-23.85	0.38	2775.1	2833.7	yes
6004	20.119	0.941	-27.845	0.739	2790.6	2829.9	yes
6005	12.989	1.138	-21.774	0.043	2785.7	2868.1	yes
6037	19.063	0.89	-23.206	0.689	2799.7	2843.1	no
6038	19.255	0.819	-22.609	0.413	2804.1	2833.2	yes
6039	19.355	0.864	-29.841	0.76	2809.1	2871.7	no
6074	18.725	0.782	-27.61	1.01	2828.2	2831.8	yes
6100	17.694	0.718	-23.382	0.217	2858.6	2809.6	yes

ACS Star ID	V	V-I	V_{rad} [km/s]	δV_{rad} [km/s]	ACS X Pixels	ACS Y Pixels	Cluster Member?
6133	16.921	0.878	-22.932	0.248	2886.7	2808.2	yes
6167	14.361	0.972	-26.561	0.055	2919.6	2809.9	yes
10025	18.216	0.71	-23.533	0.41	2650.8	2972.9	yes
10049	19.123	0.805	-23.45	4.1	2682.3	2899.5	yes
10050	17.413	0.697	-4.814	0.81	2681.2	2985.3	no
10051	16.65	0.873	-26.243	0.089	2677.7	3043.8	yes
10077	19.041	0.773	-26.688	0.79	2715.3	2992.5	no
10079	18.201	0.832	-15.57	0.78	2719.7	3024.6	no
10081	19.549	0.857	-28.4	1.07	2713.8	3061.4	yes
10116	16.375	0.875	-20.3	0.58	2732.5	2879.7	yes
10118	19.026	0.833	-21.26	0.436	2742.5	2890.3	no
10119	18.671	0.761	-17.667	0.41637	2726.9	2973	yes
10143	18.858	0.782	-24.48	0.4776	2767.7	2898.2	yes
10146	20.072	0.938	-30.74	2.1	2758.9	2958.5	yes
10175	17.962	0.725	-25.272	0.269	2795.6	2937.6	yes
10179	18.52	0.752	-26.595	0.879	2782.8	3019.7	yes
10202	19.553	0.871	-30.359	1.109	2815.6	2938.9	yes
10204	19.833	0.912	-26.273	1.2502	2801.4	2994.9	yes
10205	20.002	0.942	-32.995	1.97	2820.5	3022.9	yes
10206	18.49	0.749	-28.406	0.759	2813	3043.6	yes
10247	19.947	0.848	-21.078	0.772	2842.4	2974.7	no
10279	18.24	0.743	-23.159	0.65	2867.2	2962.5	yes
10306	19.205	0.808	-20.166	1.435	2878.6	2920.3	yes
10310	19.004	0.788	-22.98	1.04	2891.6	2975.5	yes

ACS Star ID	V	V-I	V_{rad} [km/s]	δV_{rad} [km/s]	ACS X Pixels	ACS Y Pixels	Cluster Member?
10312	17.851	0.726	-22.857	0.459	2888.3	3003.4	yes
10333	19.32	0.833	-26.528	2.61	2913.8	2888.1	yes
10372	16.57	0.94	-53.23	0.3345	2929.1	3010	no
10245	14.468	0.964	-20.628	0.098	2838.3	2953.7	yes
10248	14.864	0.971	-22.386	0.0872	2828.6	2988.5	yes

Table B.1: Radial velocity data from the GMOS IFU, the photometry is from the Advanced Camera for Surveys.

To convert from NIRI coordinates to ACS coordinates use:

$$x_{\mathrm{ACS}} = (A \times x_{\mathrm{NIRI}}) + B \tag{B.1}$$

$$y_{\mathrm{ACS}} = (C \times y_{\mathrm{NIRI}}) + D \tag{B.2}$$

Here A & C = 0.438 (the NIRI plate scale divided by the ACS plate scale), B = 2636 and C = 2761.5.

Appendix C

Bulk Motion of Messier 71

Here we attempted to derive the bulk motion of Messier 71. For this we need to calculate the bulk proper motion of the cluster. Stars with known proper motions or distant galaxies can serve as extragalactic anchors to determine the bulk motion of a globular cluster. We attempted to look for point like galaxies in our NIRI field to find an extra galactic anchor. The first task was to use our PSFs that we had created from chapter 2 and subtract stars from our images. We then look for any left over flux in the subtracted image. A point like star would have zero residual flux whereas a galaxy which is elongated would have some left over.

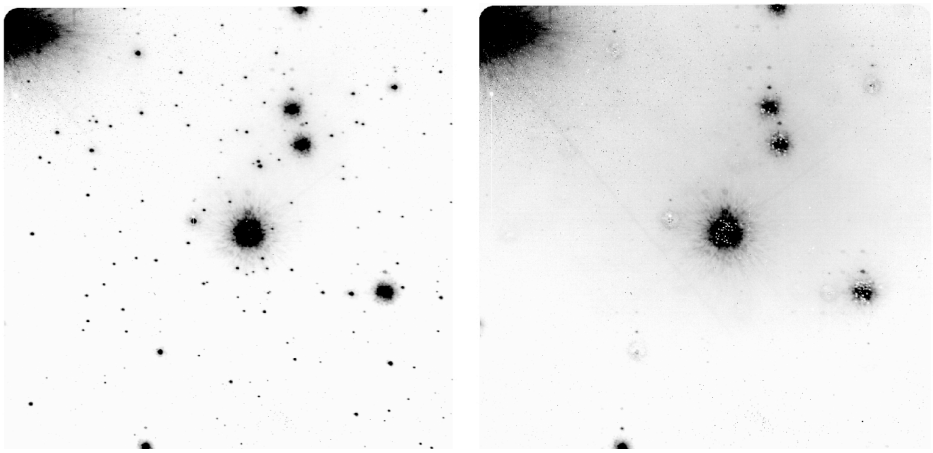

Figure C.1: An example of a NIRI image prior to star subtraction.

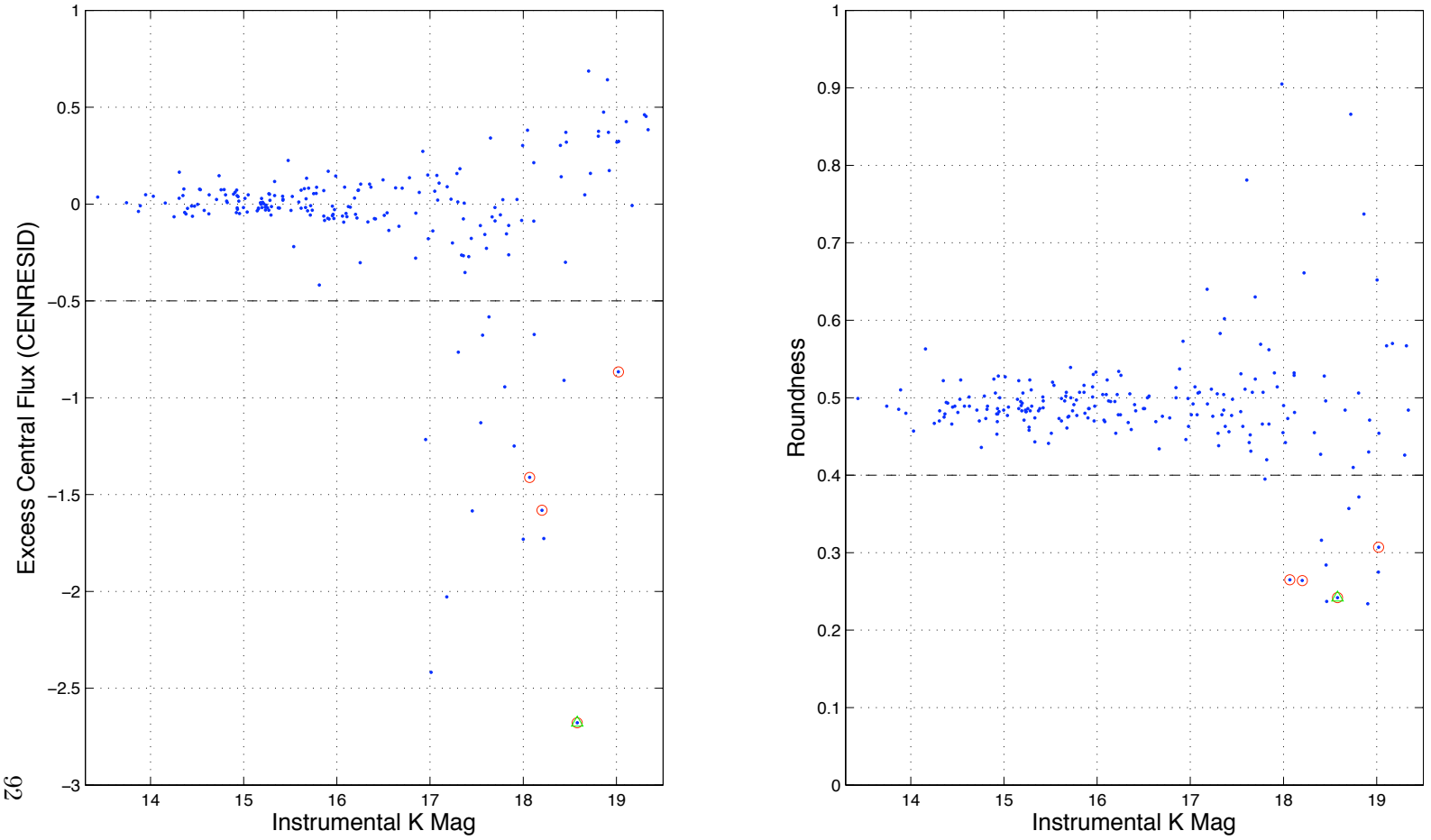

Figure C.2: Four objects were found to survive both cuts in residual flux and sharpness. Three of them were found to be on the cluster CMD, the fourth was not.

From the four objects that survived the cuts in excess flux and roundness three of them were found to be on the CMD, the fourth was not. However, upon closer inspection the object is likely a visual binary star. The bulk motion of M71 can still be calculated using background galaxies, from figure 2.2 there are numerous background galaxies visible. The bulk motion of M71 has already been calculated by Cudworth (1985) [6] and it resembles the motion of a typical galactic disk cluster.

Appendix D

Installation of DAOPHOT

The installation of DAOPHOT may not be trivial to a novice user, especially if the user has little experience with command line scripts and Fortran makefiles. The following explains how to install DAOPHOT on a computer running Mac OS. This is different from the DAOPHOT software that comes pre-installed on IRAF, this is a standalone version which offers more versatility and options for reduction of photometric and astrometric data. Prior to installation of DAOPHOT and its family of software the user will need to acquire the following software:

1. Download and install a gcc compiler

2. Install Mac Xcode developer's tools. This is a free download from Apple Inc and also comes on the Mac OS installation DVD.

3. Download and install the cfitsio package. This is avaialbe from the High Energy Astrophysics Science Archive Research Center's (HEASARC) software page.

4. Acquire DAOPHOT from Peter Stetson.

Installing of DAOPHOT

```
F77 = g77
FFLAGS = -c -O2
LFLAGS = -O2 -Wall -Wsurprising,--defsym,mem_=0 -fbounds-check
HOSTLIBS = -L/usr/local/lib -L/usr/lib -lm -lgcc
FITLIB = /usr/local/cfitsio/lib/libcfitsio.a

# RULES:
.SUFFIXES: .o .f
.f.o:
        $(F77) $(FFLAGS) $

daophot: daophot.o pckpsf.o find.o fotometry.o \
        psf.o peak.o nstar.o fudge.o addstar.o substar.o \
        group.o sort.o lnxsubs.o fitsubs.o iosubs.o mathsubs.o
        $(F77) $(LFLAGS) -o daophot daophot.o pckpsf.o find.o fotometry.o \
        psf.o peak.o nstar.o fudge.o addstar.o substar.o \
        group.o sort.o lnxsubs.o fitsubs.o \
        iosubs.o mathsubs.o \
        $(HOSTLIBS) $(FITLIB)

allstar: allstar.o allstsubs.o lnxsubs.o \
        iosubs.o mathsubs.o fitsubs.o
        $(F77) $(LFLAGS) -o allstar allstar.o allstsubs.o \
        lnxsubs.o iosubs.o mathsubs.o fitsubs.o \
        $(HOSTLIBS) $(FITLIB)

daomaster: daomaster.o iosubs.o mathsubs.o lnxsubs.o dummysm.o
        $(F77) $(LFLAGS) -o daomaster daomaster.o iosubs.o mathsubs.o lnxsubs.o dummysm.o

daomatch: daomatch.o iosubs.o mathsubs.o lnxsubs.o
        $(F77) $(LFLAGS) -o daomatch daomatch.o iosubs.o mathsubs.o lnxsubs.o

montage2: montage2.o mathsubs.o iosubs.o lnxsubs.o fitsubs.o
        $(F77) $(LFLAGS) -o montage2 montage2.o mathsubs.o iosubs.o \
        lnxsubs.o fitsubs.o \
        $(HOSTLIBS) $(FITLIB)

allframe: allframe.o fitsubs.o lnxsubs.o iosubs.o mathsubs.o
        $(F77) $(LFLAGS) -o allframe allframe.o fitsubs.o \
        lnxsubs.o iosubs.o mathsubs.o \
        $(HOSTLIBS) $(FITLIB)

daogrow: daogrow.o iosubs.o mathsubs.o lnxsubs.o
        $(F77) $(LFLAGS) -o daogrow daogrow.o iosubs.o mathsubs.o lnxsubs.o
```

Figure D.1: Daophot Makefile.

Modify the fifth line in the included Makefile to have the FITSLIB directed to the folder where libcfitsio.a is found (see figure D.1)

Switch to the tsch shell in terminal, this shell is required to install DAOPHOT. Once in tsch run Makefile. This will only compile the programs and not package them all into their suites. It packages only the the suite found at the top of the Makefile script.

Now edit Makefile and delete the DAOPHOT code and replace it with the next package as the suite at the top of the script.

Repeat the step in figure D.2 until the rest of the suites are installed. When this is finished executables for daophot, daomaster, daomatch, daogrow, allstar, montage2 and allframe should all be ready for use.

```
F7 = g77
FFLAGS = -c -O2
LFLAGS = -O2 -Wall -Wsurprising,--defsym,mem_=0 -fbounds-check
HOSTLIBS = -L/usr/local/lib -L/usr/lib -lm -lgcc
FITLIB = /usr/local/cfitsio/lib/libcfitsio.a

# RULES:
.SUFFIXES: .o .f
.f.o:
	$(F77) $(FFLAGS) $

allstar: allstar.o allstsubs.o lnxsubs.o \
	iosubs.o mathsubs.o fitsubs.o
	$(F77) $(LFLAGS) -o allstar allstar.o allstsubs.o \
	lnxsubs.o iosubs.o mathsubs.o fitsubs.o \
	$(HOSTLIBS) $(FITLIB)

daomaster: daomaster.o iosubs.o mathsubs.o lnxsubs.o dummysm.o
	$(F77) $(LFLAGS) -o daomaster daomaster.o iosubs.o mathsubs.o lnxsubs.o dummysm.o

daomatch: daomatch.o iosubs.o mathsubs.o lnxsubs.o
	$(F77) $(LFLAGS) -o daomatch daomatch.o iosubs.o mathsubs.o lnxsubs.o

montage2: montage2.o mathsubs.o iosubs.o lnxsubs.o fitsubs.o
	$(F77) $(LFLAGS) -o montage2 montage2.o mathsubs.o iosubs.o \
	lnxsubs.o fitsubs.o \
	$(HOSTLIBS) $(FITLIB)

allframe: allframe.o fitsubs.o lnxsubs.o iosubs.o mathsubs.o
	$(F77) $(LFLAGS) -o allframe allframe.o fitsubs.o \
	lnxsubs.o iosubs.o mathsubs.o \
	$(HOSTLIBS) $(FITLIB)

daogrow: daogrow.o iosubs.o mathsubs.o lnxsubs.o
	$(F77) $(LFLAGS) -o daogrow daogrow.o iosubs.o mathsubs.o lnxsubs.o
```

Figure D.2: The Makefile is now edited so Allstar is the next suite to be packaged. Run Makefile again and Allstar will be installed.

Appendix E

Extra Photometric Work

Here we present additional colour-magnitude diagrams from two other data sets of Messier 71. Both data sets were not involved in our analysis of the data but are here to show that they are available for the interested researcher. This data is available for download from the Canadian Astrophysical Data Centre.

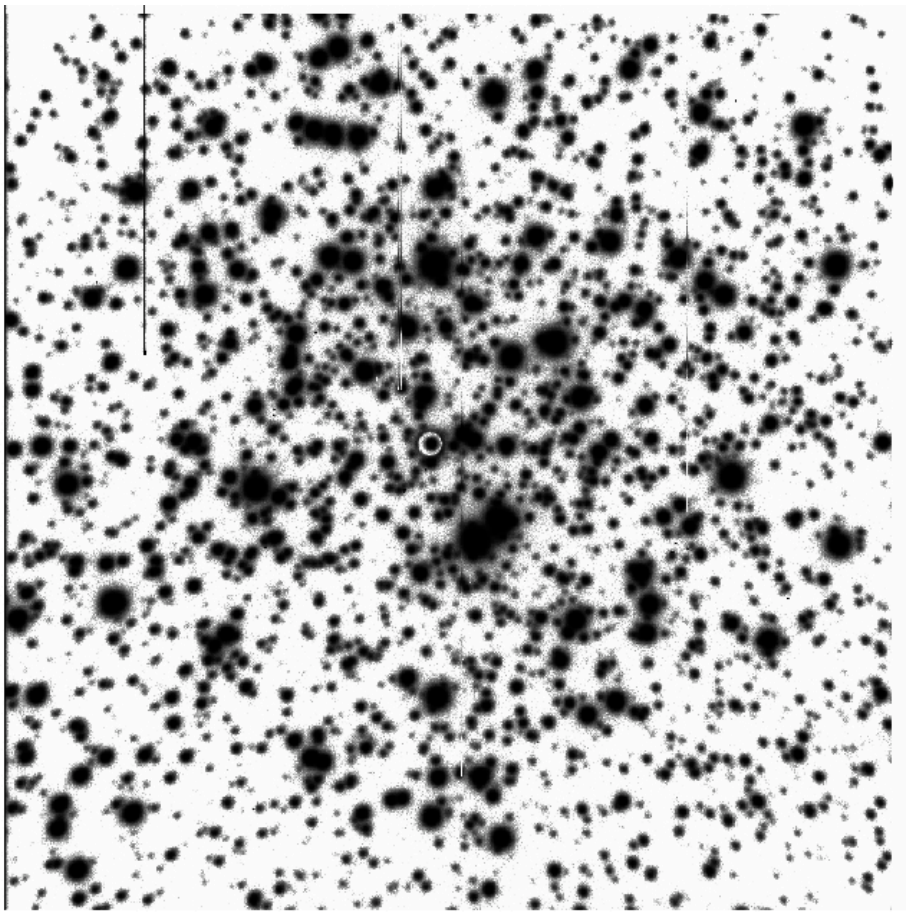

Figure E.1: Canada-France-Hawaii Telescope image of M71 from The CFHT Adaptive Optics Bonnette from 1991. With a field of view is $90'$ on each side of the image, two images one in B and the other in R with a integration time of 120s for each filter.

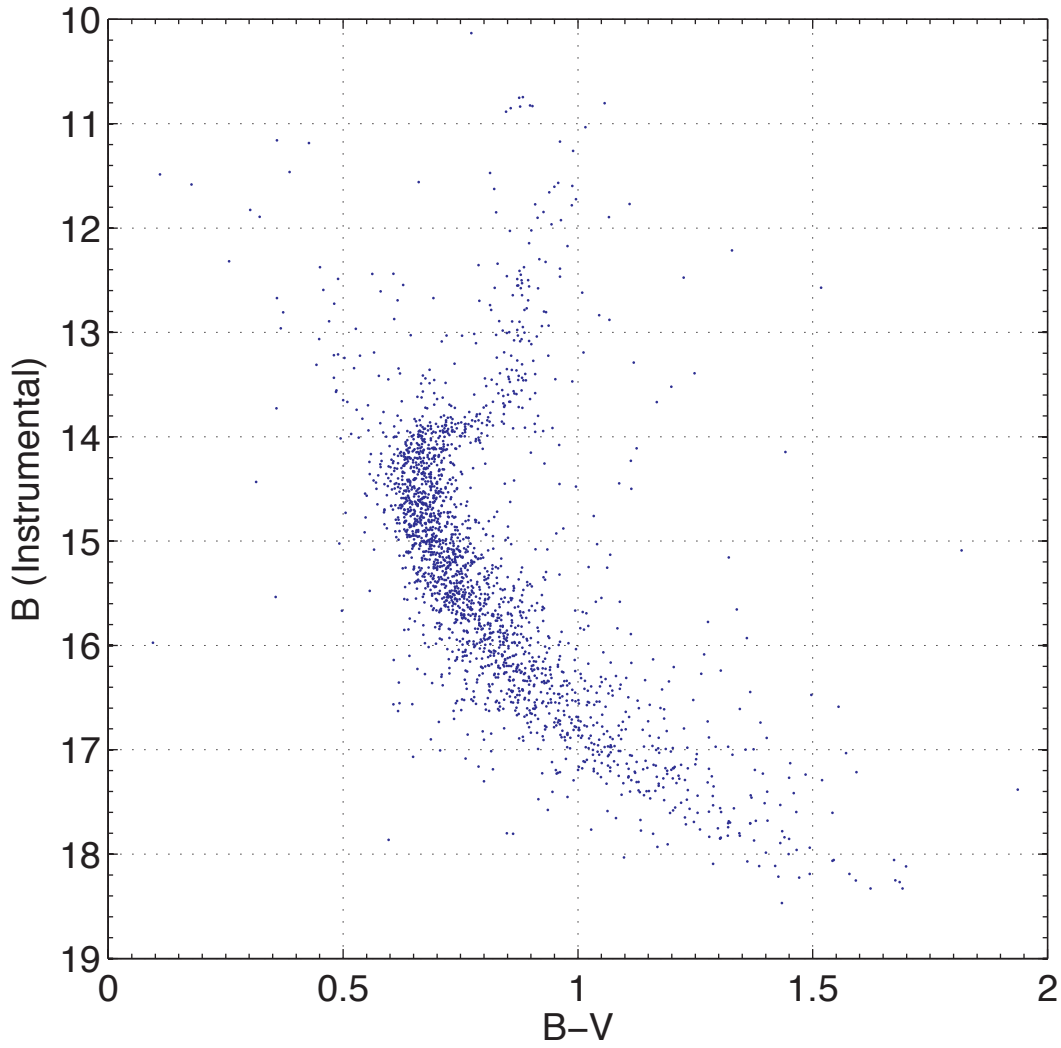

Figure E.2: A CMD from the data in Figure E.1. The CMD is in uncalibrated magnitudes.

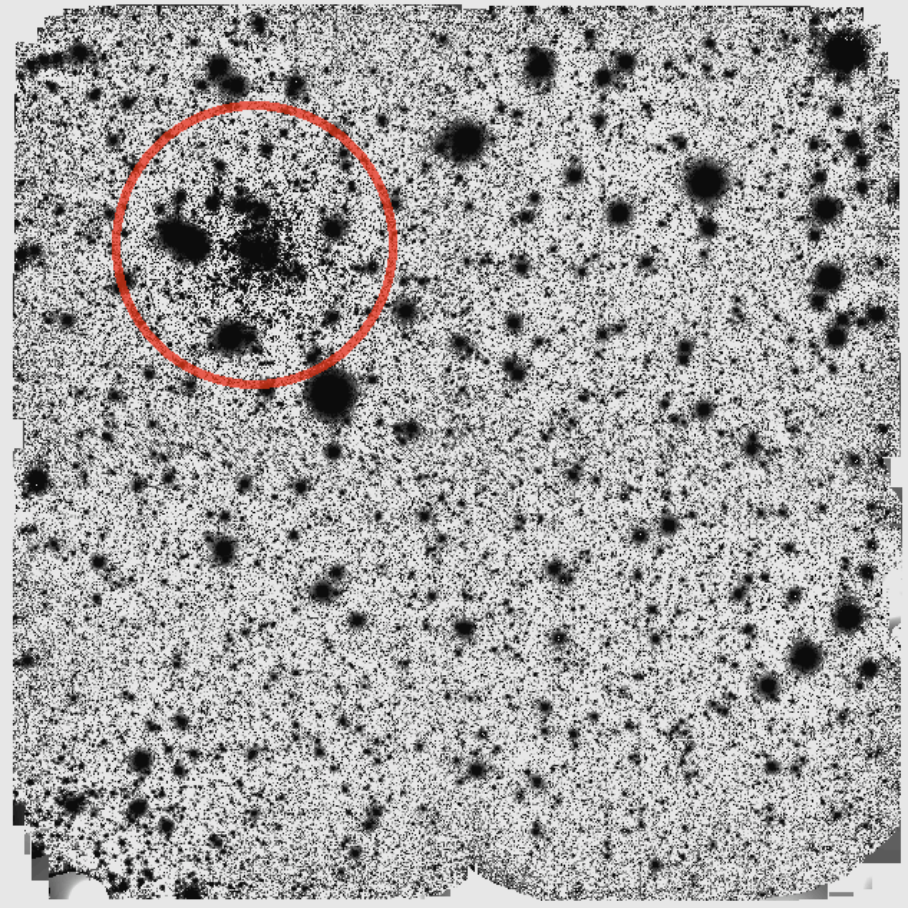

Figure E.3: Image of Messier 71 obtained using the Wide Field Infrared camera from CFHT. The image is $20'$ x $20'$. This is a H band image of the cluster which is found in the top left hand of the image. The red circle depicts a $\sim 7'$ circle centred on the cluster centre

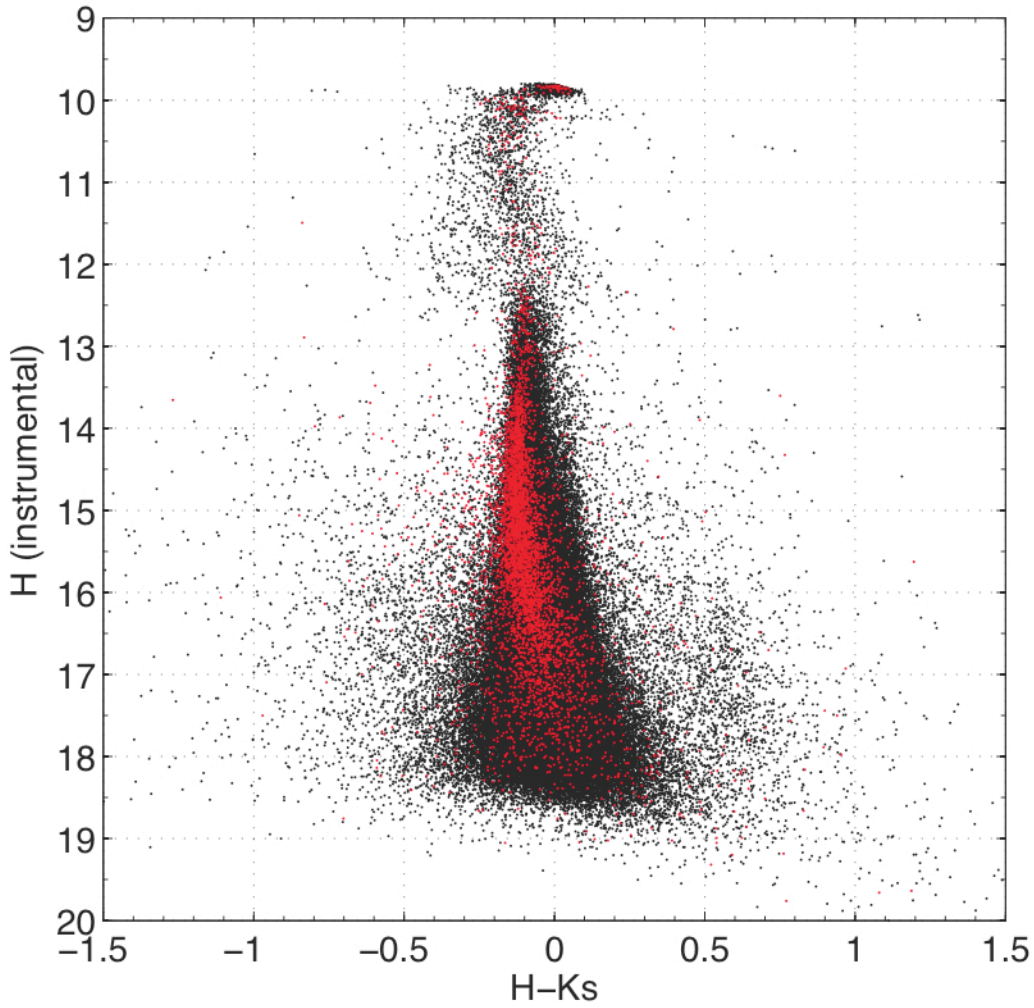

Figure E.4: A CMD from the data in Figure E.3. The stars within the circle are represented with red points, they are likely cluster members, likely galatic field stars are represented by black markers, those are also the stars which were not in the circle from Figure E.3.